*Author:*
**Buchanan, Emma**

*Title:*
**Spatial Resolution Studies for the LHCb VELO Upgrade**

# Spatial Resolution Studies for the LHCb VELO Upgrade

by

Emma Buchanan

A thesis submitted to the University of Bristol for the degree of Doctor of Philosophy

in the
Faculty of Science
School of Physics

October 2018

# Abstract

The Vertex Locator (VELO) detector is a silicon strip detector that surrounds the proton-proton interaction region of the LHCb detector, reconstructing primary and secondary vertices. The detector will be upgraded during Long Shut Down 2 of the LHC as part of a full LHCb detector upgrade program that aims to allow the experiment to operate at higher luminosities. The VELO will replace the current silicon strip sensors with silicon hybrid pixel sensors which consist of a planar silicon sensor bump-bonded to a readout ASIC. Multiple silicon sensor prototypes have been characterised and tested in a laboratory and at the SPS testbeam facility using the TimePix3 Telescope. The TimePix3 telescope was found to have a telescope resolution of $1.69 \pm 0.16$ µm in $x$ and $1.55 \pm 0.16$ µm in $y$. The focus of this thesis is the study of the spatial resolution performance of the sensors before and after exposure to a maximum radiation fluence of $8 \times 10^{15}$ $1\text{MeV}\text{n}_{\text{eq}}\text{cm}^{-2}$. The TimePix3 ASIC, which has analogue readout, was used for the majority of the prototype testing. However, the VeloPix ASIC designed for the upgrade has a binary readout. Therefore analogue (Centre of Gravity) and binary position reconstruction algorithms were performed on TimePix3 data and the spatial resolutions compared. Binary resolution was found to be better than analogue resolution independent of the applied bias voltage, both before and after irradiation. This was because of a non-linear charge sharing feature in the silicon sensor that degraded the precision of the analogue position reconstruction and hence the analogue spatial resolution. The Centre of Gravity algorithm assumes linear charge sharing between pixels and therefore requires a non-linear correction to correct for the sensor effects. Without a correction, the binary resolution was generally better over a range of different track angles, where the analogue resolution only became better than binary after 10° for non-irradiated sensors and 18° for irradiated. One method of correcting for the non-linear feature is introduced but was determined not to be practical. Further work, beyond that presented in this thesis, is required to correct for the non-linear effects. The sensor prototype that best met the requirements of the upgrade was a 200 µm thick n-on-p sensor with an implant size of 39 µm and a guard ring size of 450 µm, produced by Hamanatsu.

# Declaration of authorship

I, Emma Buchanan, declare that the work in this dissertation was carried out in accordance with the requirements of the University's Regulations and Code of Practice for Research Degree Programmes and that it has not been submitted for any other academic award. Except where indicated by specific reference in the text, the work is the candidate's own work. Work done in collaboration with, or with the assistance of, others, is indicated as such. Any views expressed in the dissertation are those of the author.

Signed: _____

Date: _____

# Acknowledgements

From fairly early on in my undergraduate physics degree, I knew that particle and nuclear detection was an interest of mine. When searching for a PhD, it was difficult to find a position that would allow me to solely study detector physics, therefore I would like to thank the Bristol Particle Physics Group for giving me the opportunity to so. I had an excellent time being part of the Bristol group and I am very sad to be leaving.

Thanks to Leonor Frazao and Chiara Giroletti for joining me on many tea breaks and adventures around Bristol and at Summer schools. Thanks to Tai Sakuma for providing endless chocolate. Thanks to Martisse Foster for solving all problems. And thanks to both Sophie Richards and Lana Beck for being great office mates. Sophie you helped me a lot when I first joined the VELO and Lana you kept me sane and entertained during the final months of writing.

Special thanks to Jaap Velthuis for being a great supervisor and allowing me to make impromptu plots daily when there really wasn't time left to make them. In the end I think some of my best plots are the ones made during this time. I learned a lot from you and I really hope that one day we work together again.

I would like to thank the LHCb VELO group, especially Paula Collins, Kazu Akiba, Heinrich Schindler and Martin Van Beuzekom. Also Elena Dall'occo, Vinícius (Vinny) Franco and Tim Evans, we had an unforgettable time at testbeams. I look forward to the release of our Testbeam Greatest Hits album, including "Dancing Beam" and "Mr Schindler give us beam bum bum bum bum."

Thanks to all my friends that I met on LTA at CERN, especially David, it was a wonderful experience and I sometimes miss the "beautiful" R1 wine and Wednesday night kebabs in Champs Frechets.

And as promised all those years ago, thank you Anna Duncan for collecting my finished masters thesis and submitting it for me. We both lack organisational skills, but at least we get it done in the end, even if we need each others help to do it.

And finally thanks to my family for all of their love, support and encouragement over the years. I could not have completed this PhD without them.

# Author's contribution

I was actively involved in the prototype testing campaign from October 2014 until September 2017, collecting data at both the SPS testbeams and in the laboratory at CERN. The pointing resolution study in Chapter 4 is based on a basic simulation that was initially written by another collaborator but I further optimised it for the TimePix3 telescope. The measurements of the multiple scattering angles using testbeam data and the comparisons of the biased residuals and mean cluster sizes was analysis performed by myself. All analysis presented in Chapters 6 and Chapters 7 are all of my own work, with the exception of any comparisons to binary resolutions measured using LHCb Simulation.

# Contents

# List of Figures

# List of Tables

# Introduction

A good understanding of the basic concepts of how radiation interacts with matter allows invisible particles to become "visible". For example, charged particles traversing through a material interact via the electromagnetic force, causing excitation and ionisation of the atomic electrons [1]. This ionisation creates a measurable signal, that is used to detect the particle. This concept has been exploited in the field of particle physics to build different detector types that can reconstruct particles that are produced at proton-proton collisions at the Large Hadron Collider (LHC). The proton-proton collisions result in a shower of sub-atomic particles that need to be measured for subsequent physics analyses. It is crucial that the trajectory of particles is reconstructed so that their momentum (in parallel with a magnet) can be measured and their point of origin is extrapolated. This requires the separation of tracks originating from decay vertices from those produced at the primary interaction vertex. The detectors designed to track the trajectory of charged particles are called tracking detectors, which usually consist of a series of silicon planes. Traversing charged particles generate charge in all planes, allowing for their trajectory to be reconstructed.

The Large Hadron Collider beauty (LHCb) experiment at the LHC [2], is an experiment focused on the study of $b$-quarks. Its primary goal is to look for indirect evidence of new physics in CP violation and rare decays of beauty and charm hadrons. From an experimental view point, $\boldsymbol{B}$ mesons distinguish themselves from other mesons by their long lifetimes, meaning that they travel a measurable distance before decaying. This results in a displaced secondary vertex. The VErtex LOcator (VELO) detector is a silicon strip detector that surrounds the interaction region of LHCb [3]. Its main role is to reconstruct primary and secondary vertices.

The LHCb detector will be upgraded during Long Shutdown 2 of the LHC, starting from 2019 [4]. The upgrade is to allow the experiment to run at a higher luminosity. The VELO detector will undergo a substantial upgrade such that the detector will be able to cope with higher data rates and tolerate a maximum fluence of $8{\times}10^{15}$ $1\text{MeV}\text{n}_{\text{eq}}\text{cm}^{-2}$. One of the major changes is the move from silicon strip sensors to hybrid pixel sensors. Over several years a major R&D effort has been carried out to determine which silicon sensor type is best suited to the performance requirements of the VELO upgrade. The requirements were outlined in the Technical Design Report (TDR) [5].

Prototype sensors were provided by different manufacturers and varied in bulk type, thickness, implant size and guard ring designs. The prototypes were tested in a laboratory and using the TimePix3 Telescope at the SPS testbeam facility. For testing purposes the sensors were readout using a general purpose analogue readout Application Specific Integrated Circuit (ASIC) called the TimePix3 [6], which is a predecessor of the binary readout ASIC designed for the upgrade, called the VeloPix [7].

This thesis focuses on the study of the spatial resolution and the charge sharing properties of the prototypes, both before and after exposure to radiation. The spatial resolution is studied as a function of the bias voltage and track angle. Since the TimePix3 has an analogue readout ASIC and the VeloPix has a binary readout, the TimePix3 data was turned binary by ignoring the charge information. This allowed direct comparisons between binary and analogue resolutions, and also to determine if the binary resolution measured using the different prototypes matched simulations presented in the upgrade TDR.

# Chapter 1

# The LHCb Experiment

In this chapter, the LHC accelerator facility will be introduced. This will be followed by a detailed description of the LHCb experiment and its sub-detector systems. As previously mentioned, the LHCb detector will be upgraded. The motivations for the upgrade and the changes to the trigger system are briefly discussed. This will be followed by a more detailed outline of the VELO upgrade components and expectations.

## 1.1 The Large Hadron Collider

The European Organization for Nuclear Research, commonly known as CERN, is home to the worlds largest particle collider, the Large Hadron Collider (LHC) [8]. The LHC is a 27 km long circular collider, ~ 100 m underground, which accelerates bunches of protons up to energies of $\sqrt{s} \sim 14$ TeV. The protons are produced by stripping electrons from hydrogen molecules. The protons are then accelerated through a series of different particle accelerators, each ramping up the energy before being injected into the LHC. An illustration of the accelerator complex is shown in Figure 1.1. The protons are first accelerated to 50 MeV using the LINAC 2, a linear accelerator. The protons are then injected into a sequence of circular accelerators, the Proton Synchrotron Booster (PSB), the Proton Synchrotron (PS), and the Super Proton Synchrotron (SPS) which increase the energy to 1.4 GeV, 25 GeV, and 450 GeV respectively. After the SPS, the proton bunches are separated into two beams which are transferred into two counter-rotating

beams in the LHC. Once in the LHC, the protons are accelerated to the maximum design energy of 6.5 TeV. Each beam has a maximum of 2808 bunches with a maximum collision rate of 25 ns.

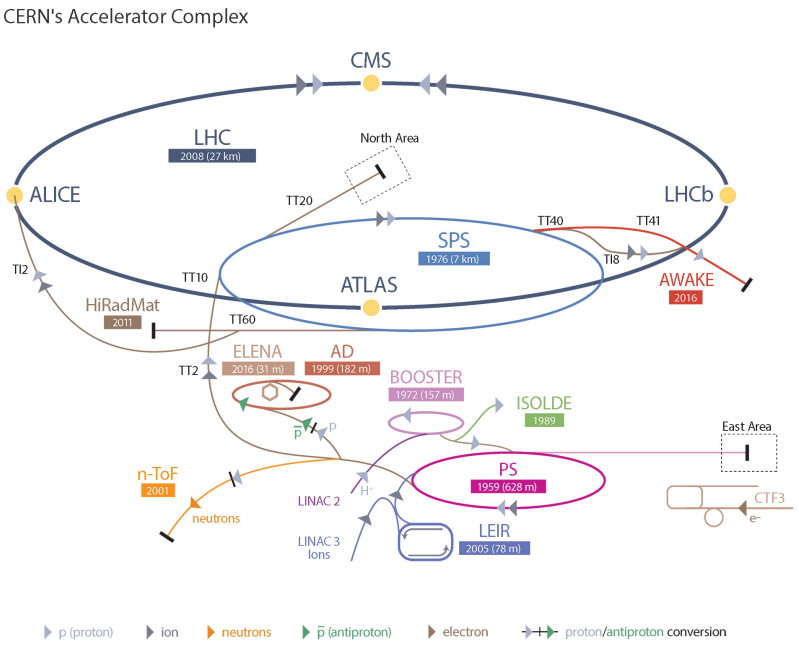


Figure 1.1: Illustration of the LHC accelerator facility and experiments.

The LHC uses a series of super conducting magnets to steer and focus the beams. The dipole magnets keep the protons in a circular path, while quadrupole magnets focus the beams. The protons are collided at four collision points situated around the LHC, at these points are the four main experiments. There are two general purpose detectors: A Toroidal LHC ApparatuS (ATLAS) [9] and Compact Muon Solenoid (CMS) [10], which have a varied physics program. The other two experiments, A Large Ion Collider Experiment (ALICE) and the Large Hadron Collider Beauty Experiment (LHCb) are more specialised in their physics goals. The ALICE [11] experiment mainly studies the properties of the quark gluon plasma in the collision of heavy ions, which the LHC provides for ~1 month of a running year. The LHCb experiment is searching for indirect evidence of new physics in CP violation and rare decays of heavy flavour hadrons.

## 1.2 The Large Hardron Beauty Detector

In proton-proton (p-p) collisions, $b\bar{b}$ pairs are mostly produced by parton-parton interactions, where one parton has a significantly higher energy than the other [12]. This results in the $b\bar{b}$ pair being boosted in the direction of the higher energy parton, relative to the laboratory rest frame, meaning that they are both moving in either the forwards or backwards direction. The production angle of $b$ and $\bar{b}$ mesons in the lab reference frame is shown in Figure 1.2. $b$-mesons are long lived, and therefore the events have well separated primary and secondary vertices. $b$-mesons also have a large mass meaning that the decay products can have a large transverse momentum ($p_T$) [12], where $p_T$ is the momentum perpendicular to the beamline. Interesting decays of $b$ and $c$ hadrons typically contain a number of kaons, pion and protons. To reduce background, particle identification is key.

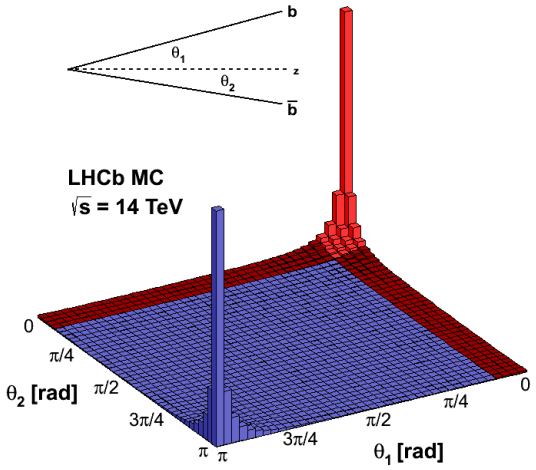


Figure 1.2: Angular distribution of $b$ and $\bar{b}$ quarks produced in simulated p-p collisions at a centre of mass energy of = 14 TeV. The red shaded area represents the acceptance of LHCb and $\theta_1$ and $\theta_2$ corresponds to the angle between $b$ and $\bar{b}$ with respect to the beam axis [13].

The angular distribution led to the design of the LHCb detector as a forward angle spectrometer, with a horizontal coverage of 10 to 300 mrad and a vertical coverage of 250 mrad; both with respect to the incoming proton beams [2]. An illustration of the

detector is shown in Figure 1.3. A vertexing detector called the VELO detector surrounds the interaction region and its key role is to reconstruct the primary and secondary vertices. Tracking stations are positioned before and after a room temperature dipole magnet of strength 4 Tm which bends charged particles for momentum determination. The particle identification system includes Electromagnetic and Hadronic calorimeters which measure the energy of particles, and a muon system to reconstruct and identify muons. In addition, there are two Ring Imaging Cherenkov (RICH) detectors, which are used to distinguish kaons, protons and pions. A trigger is used to select $b$ and $c$ events in the harsh hadronic environment. In the following section, each of the different sub-detectors will be discussed in more detail.

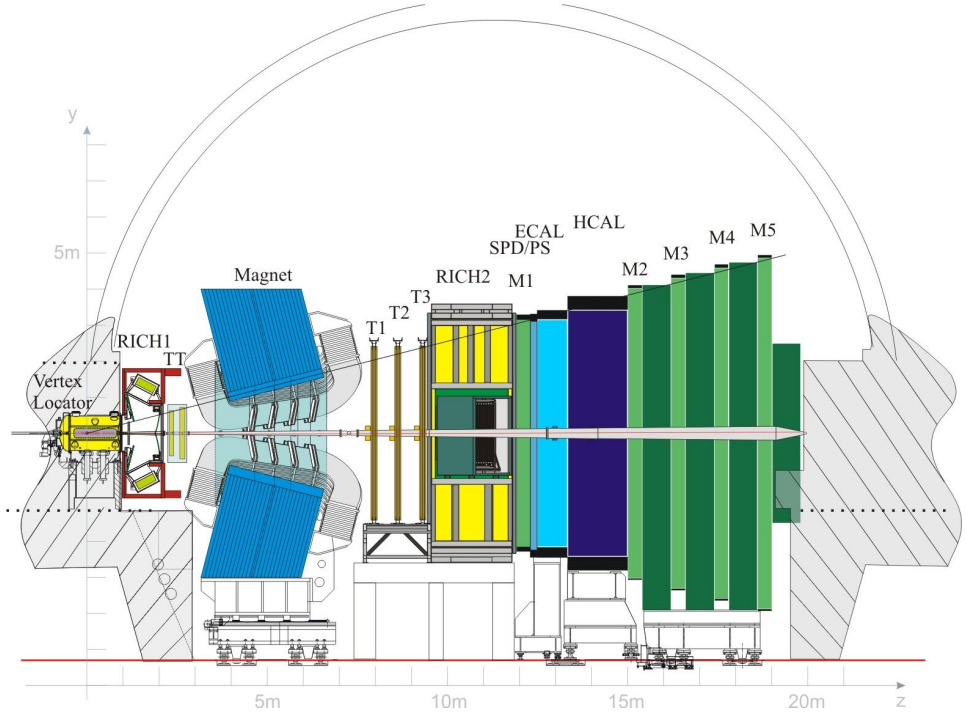


Figure 1.3: Illustration of the LHCb experiment.

### 1.2.1 The VErtex LOcator (VELO)

The VErtex LOcator (VELO) is the detector that surrounds the interaction region of the LHC [14]. The role of the VELO is to provide track coordinates and timing information which are used in the reconstruction of primary and secondary vertices produced by p-p interactions, and to provide tracking information upstream of the magnet. Tracks originating from secondary vertices with large impact parameters are a distinctive feature

of decaying beauty and charm mesons. The impact parameter is the distance of closest approach of the tracks to the primary vertex, as shown in Figure 1.4. If the particle is long lived the impact parameter can be large. Therefore the LHCb trigger relies on an impact parameter cut to identify interesting events, further described in Section 1.2.7. The trigger needs the VELO to measure the impact parameter to a high precision. The impact parameter resolution is described by the following expression [5]:

$$\sigma_{IP}^2 = \frac{r_1^2}{p_T^2}\left(0.0136\ GeV/c\ \sqrt{\frac{x}{X_0}\left(1+0.038\ln\left(\frac{x}{X_0}\right)\right)}\right)^2 + \frac{\Delta_{02}^2\sigma_1^2 + \Delta_{01}^2\sigma_2^2}{\Delta_{12}^2} \tag{1.1}$$

where $r_1$ is the radius to the first measured point on a charged particle track, $p_T$ is the traverse momentum, $x/X_0$ is the fractional radiation length before the second measured point. $\sigma_1$ and $\sigma_2$ are the measurement errors on the first and second point. $\Delta_{ij}$ represents the distance between $i$ and $j$, where $i$ and $j$ can be 0 (the vertex), 1 (the first measured point), or 2 (the second measured point). This expression applies to a 1D impact parameter measurement [14].

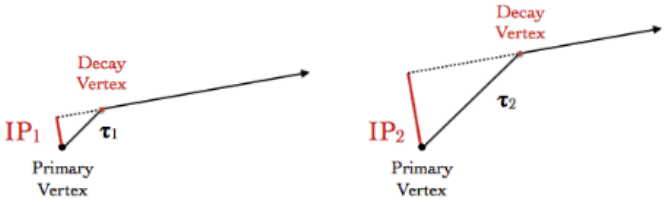


Figure 1.4: A sketch showing the definition of the Impact Parameter (IP) and its dependence on particle decay time [15].

This expression gives motivation for the design choices for the VELO. The $r_1^2$ term suggests that the first measured point should be as close to the interaction region as possible. The $x/X_0$ term shows the importance of reducing the material budget of the detector, especially limiting the material before the first and second measured point. The measurement errors $\sigma_1$ and $\sigma_2$, are the spatial resolution of the detectors that measure the track intercepts, therefore these also need to be minimised.

The VELO contains a series of silicon strip detector modules situated inside the LHC vacuum. The sensors are positioned only ~8 mm from the LHC beams. This is smaller than the aperture of the LHC beams during injection, therefore the detector is arranged

in two retractable halves. Figure 1.5 (a) shows an illustration of one half of the VELO and the RF foil, further described below. During unstable beams the two halves are retracted away from the beamline and during stable beams, the two halves close creating a full geometrical coverage around the interaction region. Each half is equipped with 21 modules with a $R$ sensor and $\phi$ sensor oriented perpendicular to the beam. Each module contains one of each type of sensor mounted on either side of a thermally conductive plate. The sensors are n-on-n type with a thickness of 300 μm, with the exception of one of the most upstream modules having two n-on-p sensors[1]. The strips of the $R$ sensor are separated into four 45° quadrants with the pitch ranging from 40 – 101.6 μm. The strips of the $\phi$ sensor are divided into an inner and outer region with the pitch varying from 35.5 – 96.6 μm, as shown in Figure 1.5 (b). The finer pitches are closest to the beamline as this is the region where the highest occupancies and data rates are expected. The readout ASICs, are placed at the periphery of the sensors and the signal from inner strips are transported to the readout via routing lines on the sensor. The ASICs, called Beatle chips, were custom made for LHCb and have analogue readout providing Time Over Threshold (ToT) information. A photograph of two VELO modules is shown in Figure 1.5 (c). The modules are cooled using evaporated $CO_2$, circulating in capillaries clamped to the bottom of the module, as shown in Figure 1.5 (d). During operations, the average temperature of a module is about -10°C. Each VELO half is separated from the LHC vacuum by 300 μm thick RF foil, creating a secondary VELO vacuum. The function of the foil is to provide shielding against RF pickup from the beams and the protect the LHC vacuum from outgassing of the detector modules.

The impact parameter resolution in the $x$-direction as a function of the inverse of the transverse momentum $p_T$ is shown in Figure 1.6 (a). Both simulation and data collected in 2012 are compared. There is a roughly linear dependence on $1/p_T$ and impact parameter resolutions of less than 35 μm are achieved for particles with $p_T > 1$ GeV/c. Thus, the VELO provides excellent impact parameter measurements for the LHCb trigger. The LHCb trigger will reject events that do not contain displaced vertices. The spatial

[1]The n-on-p sensors were installed to test their performance. At the time, the technology was a leading candidate for use in the LHC upgrades.

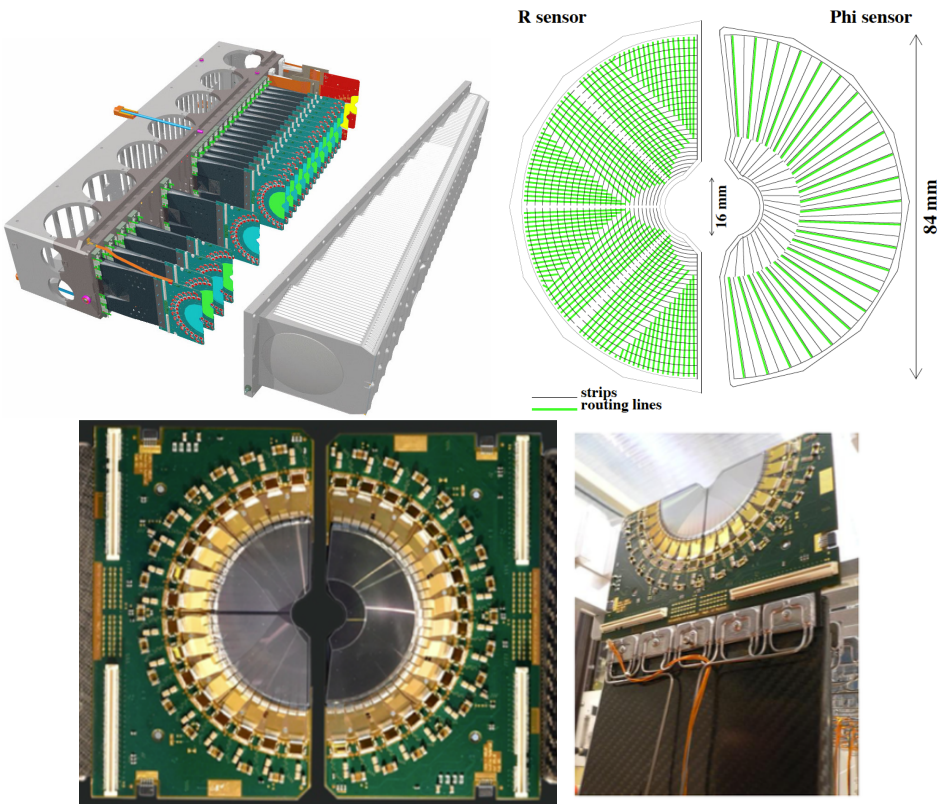


Figure 1.5: (a) Illustration of one half of the VELO and the RF foil. (b) Sketch of the silicon strip geometries for a $R$ and $\phi$ sensor. (c) Photograph of two VELO modules, one of each sensor type where the readout Beatle ASICs are in the periphery. (d) Photograph of one VELO module where the cooling system is visible at the bottom of the module.

resolution as a function of the track projected angle[2] for four different strip pitches is shown in Figure 1.6 (b) for an $R$ sensor. The resolutions have been normalised to the strip pitch [14]. The resolution varies between $\sim$ 4.3 µm and $\sim$ 18 µm, depending on the strip pitch and the track angle. The breakdown of the total material budget of the VELO is shown in Figure 1.7. The VELO design means that the majority of the electronics and mechanics are outside of the VELO acceptance. The largest contribution comes from the RF foil. Unfortunately, particles have to traverse the RF foil before reaching the first sensors, which degrades the impact parameter resolution. Studies are currently being performed to determine if future upgrades of the VELO could operate without an RF foil. This has been proposed for the Phase II upgrade [17], and not the current upgrade that will be discussed in Section 1.4.

[2]Defined by $tan(\alpha_p) = l_p/d$, where $l_p$ is the distance perpendicular to the strips between the entry and exit points of the particle when traversing a detector of thickness $d$ [16].

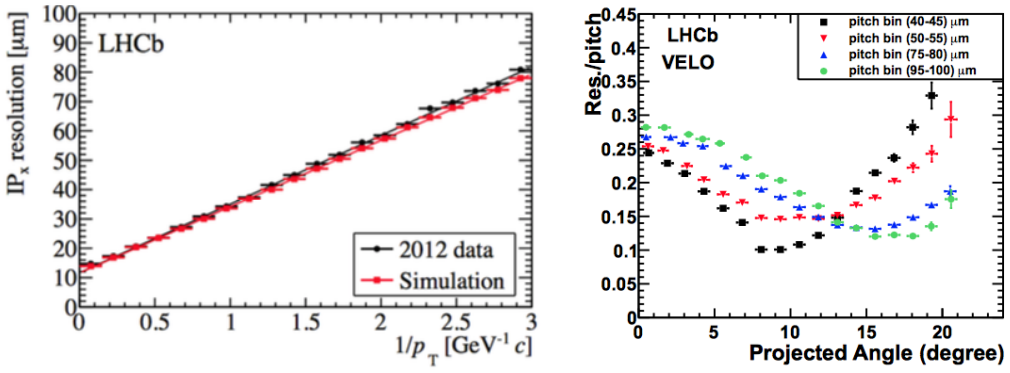


Figure 1.6: The impact parameter resolution as a function $1/p_T$ comparing data from 2012 and LHCb simulation (a). The spatial resolution as a function of the projected angle for a $R$ sensor for each of the different strip pitches (b) [14].

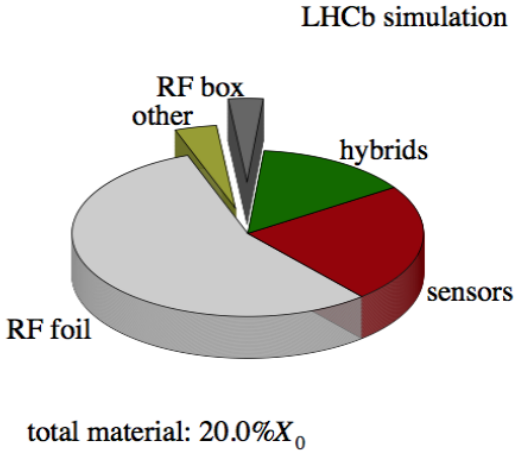


Figure 1.7: A breakdown of the material budget of the VELO within the pseudorapidity range $2 < \eta < 5$. The overall $x/X_0$ is 20%.

### 1.2.2 The Tracker Turicensis (TT)

There is an additional tracking station before the LHCb magnet called the Tracker Turicensis (TT) which is used to match tracks produced in the VELO to tracks seen in the downstream trackers [2]. It consists of four detector planes along the beam direction ($z$), as illustrated in Figure 1.8. Each plane has a series of single sided silicon strip sensors mounted on a common cooling plate. The sensors are 500 μm thick $p^+$-on-n with vertical strips of pitch 183 μm. The layers are tilted at stereo angles of 0°, +5°, -5° and 0° respectively. The TT has a spatial resolution of ~50 μm.

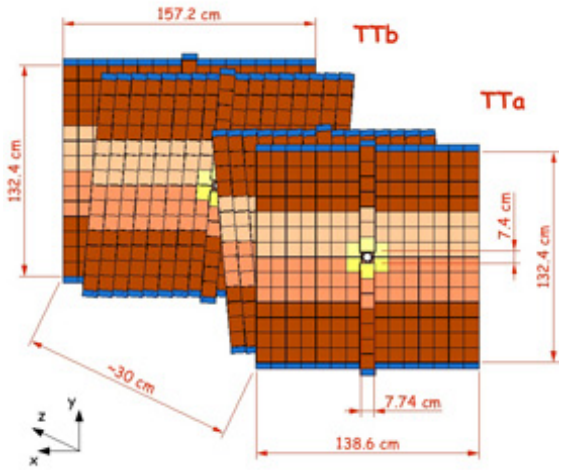


Figure 1.8: Illustration of the Tracker Turicensis (TT).

### 1.2.3 Tracking Stations T1-T3

The tracking system downstream of the magnet consist of tracking stations T1-T3. These stations are separated into two different tracker types: the Inner Tracker (IT) and the Outer Tracker (OT) [18]. The IT sits closest to the beamline and each station contains four layers of silicon strip detectors, tilted at stereo angles of 0°, +5°, -5° and 0° with respect to the vertical. An illustration of one IT layer is shown in Figure 1.9 (a). The sensors are p-on-n with a pitch of 198 µm with the thickness dependent on the location. The horizontal nature of the magnetic field requires a wider coverage of silicon sensors on the left and right of the beam pipe. Two sensors are bound together with a readout length of 22 cm, requiring a silicon sensor thickness of 410 µm to achieve a sufficient Signal to Noise ratio (S/N). Above and below the beam pipe, only a series of single sensors is required, resulting in a readout length of 11 cm therefore allowing a thinner sensor of 230 µm.

The particle flux falls off considerably with increasing radius from the beam, therefore less granularity is required in the outer regions. To avoid the high costs of installing a silicon detector over the full area of T1-T3, the OT is a gaseous straw tube detector. An illustration of the OT detector is shown in Figure 1.9 (b). The straw tube planes are tilted to match the orientation of the IT planes. The planes consist of hollow straw tubes of diameter 4.9 mm, with 24.9 µm thick gold-plated tungsten wire running through the

centre. The tubes are filled with a gas mixture of 70% Ar and 30% $CO_2$. The IT has a spatial resolution of $\sim 50$ µm and the OT $\sim 200$ µm.

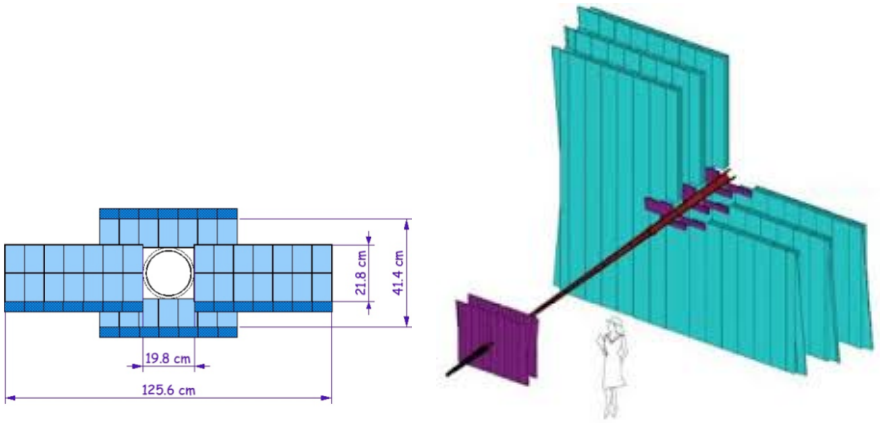


Figure 1.9: Illustration of one layer of the IT (a) and an illustration of the TT and of the tracking stations T1-T3 (b). The silicon strip devices for both the TT and IT are shown in purple and the OT is shown in blue.

### 1.2.4 RICH Detectors

As previously discussed, the LHCb detector uses RICH detectors to distinguish protons, kaons and pions [19]. There are two RICH detectors covering different momentum ranges. RICH1, situated before the LHCb magnet, covers the low momentum range of 2 - 60 GeV/c, and RICH2, situated downstream of the tracking stations T1-T3, covers the higher momentum range of 15 - 100 GeV/c. Both RICH1 and RICH2 are similar in design. An illustration of RICH1 is shown in Figure 1.10 (a). If a charged particle passes through the radiators at the entrance of the detector (aerogel for RICH1), at a velocity exceeding that of light traversing the same medium, Cherenkov photons are emitted. The photons are emitted in a cone, where the angle of emission, the Cherenkov angle, is dependent on the velocity and the refractive index of the material. The photons are then reflected in a series of mirrors: spherical focusing primary mirrors, and secondary flat mirrors to deflect the photons to photo-detectors outside the acceptance of LHCb. Here the Cerenkov angle is reconstructed. Combined with the particle momentum, which is measured downstream of the magnet, the mass of the particle can be determined and the particle identified. The reconstructed Cherenkov angles as a function of track momentum is shown in Figure 1.10 (b). There are clear separations between the protons, pion and

kaons. Also, although the RICH detectors are primarily used for hadron identification, a distinct muon band can be observed.

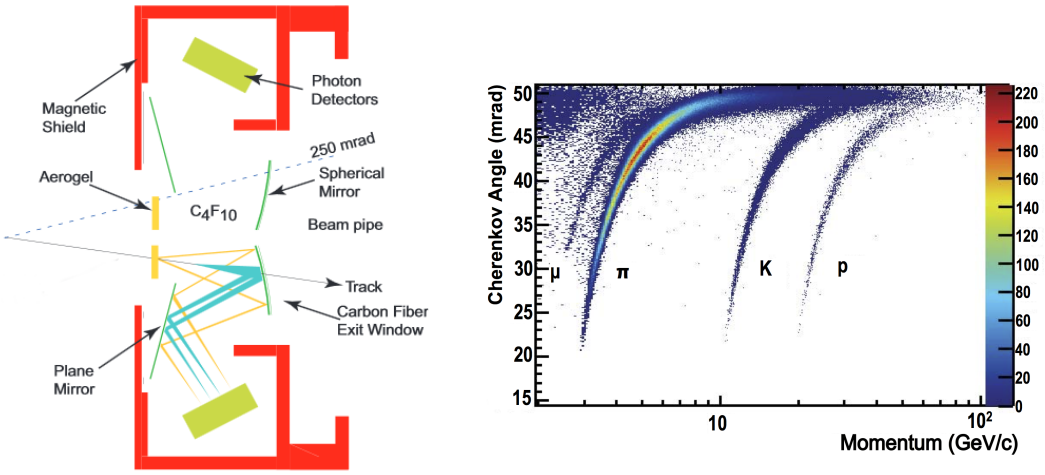


Figure 1.10: Illustration of the RICH1 detector (a). Reconstructed Cherenkov angle as a function of track momentum in the $C_4F_{10}$ radiator.

### 1.2.5 Calorimeters

The primary role of the LHCb calorimeters is the measure the positions and energies of photons, electrons and hadrons [20]. This is achieved using a series of four sub-detectors: a Scintillating Pad Detector (SPD), a pre shower detector (PS), a electromagnetic (ECAL) and a hadronic (HCAL) calorimeter. The ECAL and HCAL are used to measure the energy and positions of particles whereas the SPD and PS are used for particle identification. The SPD and PS are both made out of vertical scintillating pads, sandwiching between a lead plane. Traversing charged particles produce scintillation light in the pads, which is then transmitted to Multi Anode Photo Multipliers (MAPMTs) in the periphery using wavelength shifting (WLS) fibres. Photons do not produce scintillation light, therefore if no signal is measured in the SPD but there is a signal in the SP, the particle is likely to be a photon. Electrons and pions will both produce signals in the SPD, electrons will liberate more energy in the lead conversion layer than pions, thus the energy deposits in the SPD are used to distinguish between the two. A sketch of a simplified layout of the calorimeter system is shown in Figure 1.11.

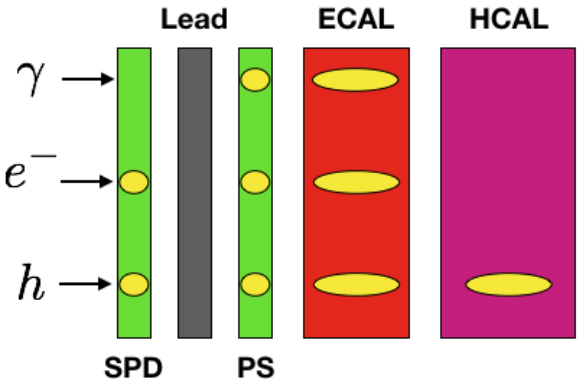


Figure 1.11: A sketch of the different sub-detectors of the calorimeter system and the interactions depending on particle type.

### 1.2.6 Muon Chambers

Muons are present in the final states of many $B$ meson decays, making muon detection very important at LHCb. The muon system has five stations, M1 to M5, and their role is to identify and measure the momentum of muons. The first muon station (M1) is positioned in front of the calorimeters and the rest are downstream of the calorimeters. M1 uses Gas Electron Multiplier (GEM) detectors and M2 to M5 use Multi Wire Proportional Chambers (MWPCs). MWPCs consist of gas volumes containing thin wires operated at high voltage. When muons interact with the gas, they create free electrons that drift towards the wires inducing a current in the readout detectors. The downstream muon stations have iron absorbers between each of the layers, in order to absorb all charged particles that are not muons. Gaseous detectors were chosen as the detector type because large areas needed to be covered and the occupancy is low. The muon system provides fast information for the high $p_T$ muon trigger and muon identification for the high-level trigger and offline analysis.

### 1.2.7 Luminosity and Trigger

The LHC collides bunches of protons every 25 ns and has a design luminosity of $\sim 10^{34}$ cm$^{-1}$s$^{-1}$, which leads to multiple p-p collisions within the same bunch crossing. This creates a significantly complicated vertex reconstruction and increases the detector occupancy. Therefore to simplify the event reconstruction, the LHCb experiment runs

at a lower luminosity of $4 \times 10^{32}$ cm$^{-2}$s$^{-1}$. Running at this level of luminosity results in a single p-p interaction per bunch crossing, on average, and limits the radiation damage effects in the detectors. The reduced luminosity is achieved using the lumo-levelling technique [21]. The proton beams are offset and gradually overlapped, giving an almost constant luminosity over a fill. An example of the development of the instantaneous luminosity over the duration of a run is shown in Figure 1.12 (a) for ATLAS, CMS and LHCb. An illustration of the lumo-levelling technique is overlain in the plot. The proton beams provided to ATLAS and CMS are collided face on to give a peak luminosity, that then degrades over the period of a fill, resulting in a maximum of 50 p-p interactions per bunch crossing.

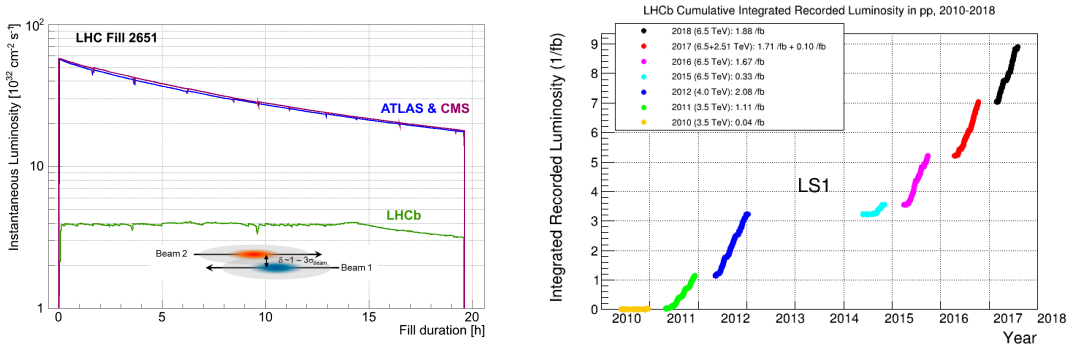


Figure 1.12: The instantaneous luminosity over the duration of a run for ATLAS, CMS and LHCb (a) and the integrated luminosity collected at LHCb over the years of running (b).

The magnitude of the data collected by each sub-detector makes it impossible to store all the data for all events, even though there is only ~ 1 p-p interaction per bunch crossing. Therefore a trigger is used to filter and save the interesting events [22]. There are two levels to the trigger: Level 0 (L0) and the High Level Trigger (HLT). The L0 trigger is implemented in hardware and reduces the data rate from 40 MHz to 1 MHz. The rate is reduced by triggering on large energy deposits or the presence of a moderately energetic muon [15]. The HLT is a software based trigger which looks for distinct features of $B$ decays, for example the displaced vertices and significant $p_T$.

Since the beginning of Run 1 the LHCb experiment has collected ~ 9 fb$^{-1}$ of integrated luminosity, as shown in Figure 1.12 (b). The LHCb experiment expects to collect approximately 10 fb$^{-1}$ of data by the end of Run 2.

## 1.3 LHCb Upgrade

Results from LHCb analyses so far have mostly been consistent with the SM. To increase sensitivities to very rare decays, that may provide insight to the physics Beyond the Standard Model (BSM), the LHCb experiment needs to collect more data. During Run 3, the LHCb experiment plans to operate at a luminosity of $2\times10^{33}$ cm$^{-2}$s$^{-1}$, which is 5 times greater than the current luminosity [4]. Maintaining this luminosity over 10 years, the experiment expects to collect 50 fb$^{-1}$. As discussed in Section 1.2.7, the LHCb experiment is not limited by the luminosity that the LHC can deliver, but by the luminosity that the current detector can operate at. The detector is limited by the L0 trigger and the radiation damage experienced by the sub-detector systems. Therefore the LHCb detector will be upgraded during Long Shut Down 2 of the LHC, beginning 2019.

To be able to operate at a higher luminosity, the L0 trigger will be removed and the trigger will become fully software based, the first of its kind at the LHC. The new trigger scheme requires a readout rate of 40 MHz for all sub-detectors, which will require an upgrade of the majority of the detector electronics. In addition, the increased luminosity will lead to larger track densities and higher radiation doses on the sub-detectors. Therefore a large fraction of the detector hardware needs to be upgraded to improve the tracking performance and radiation tolerance. The LHCb VELO will undergo a substantial upgrade and will be discussed in detail below.

## 1.4 VELO Upgrade

The upgraded VELO must be able to maintain or improve its physics performance while delivering the 40 MHz readout rate required for the upgrade trigger system [3]. With the increased luminosity, the VELO will face increased occupancies, data rates and radiation damage. To be able to operate under these conditions, all of the VELO's silicon sensors and electronics will be replaced. To reduce occupancies, silicon hybrid pixel sensors were chosen due to their high granularity in comparison to the traditional silicon strip sensors. A new readout chip was developed to cope with the increased data rates, and it will

have a binary readout. By using a binary readout, the readout circuitry is simpler and smaller. However, the charge information is lost, which predictably has consequences on the performance, especially the position reconstruction and hence spatial resolution. This is a key discussion in this thesis (Chapter 6). Severe radiation damage in silicon requires low temperature cooling. The silicon areas that are closest to the interaction region are exposed to the largest radiation damage, therefore a new cooling system has been designed to protect the very tip of the silicon from thermal runway after significant irradiation. Radiation damage effects in silicon are introduced in Section 2.3. The majority of the mechanical structure of the VELO will remain the same, with only slight modifications to allow the sensors to be closer to the LHC beam. The first active pixel will be $\sim$ 5.1 mm from the beam, in comparison to the first active strip being $\sim$ 8 mm from the beam in the current VELO. Therefore the $z$ positions of the planes have been changed to achieve a similar acceptance. These modifications require a new RF foil design to accommodate the new module layout.

### 1.4.1 Hybrid Pixel Sensors

In a hybrid pixel detector, a planar silicon sensor is connected to a readout ASIC via small soldering bumps called "bump bonds", as illustrated in Figure 1.13 [23]. Charged particles interact with the silicon semiconductor material and produce electron-hole pairs which in turn induce an electrical signal that is measured by the readout ASIC. This phenomenon is further described in Section 2.2. The pixel size in the sensor must match the pixel size in the readout ASIC, where the pixel size is limited by the area required for the readout circuitry and the size of the bump bonds. The VeloPix ASIC consists of a matrix of $256 \times 256$ pixels of $55 \times 55$ µm each, resulting in an active area of $14 \times 14$ mm$^2$ [7]. As previously mentioned, the VeloPix has a binary and data driven readout which means that every hit is time-stamped, labelled and immediately sent off chip. The data is readout in super pixels which are groups of $2 \times 4$ pixels for which the data is sent off together. The output includes the bunch crossing ID, the location of the super pixel and the pixels within the group that exceeded the threshold. The super pixel readout method reduces the data by 30%. A table summarising some of the VeloPix

| Specification | |
|---|---|
| Readout Type | Triggerless Binary |
| Pixel Dimensions | $55 \times 55$ µm$^2$ |
| Matrix Size | $256 \times 256$ |
| Timing Resolution | 25 ns |
| Power Consumption per ASIC | $< 3$ Wcm$^{-2}$ |
| Peak Pixel Hit Rate | 900 MHits/s |

Table 1.1: Summary of VeloPix specifications.

specifications are shown in Table 1.1. Three VeloPix devices will share the same planar sensor, and is refereed to as a "Tile" or "Triple" sensor, as shown in Figure 1.14. The pixel size is the same but the overall dimensions differ and are approximately 14×43 mm$^2$. The silicon sensor design is a topic of this thesis and is therefore further discussed in Chapter 3.

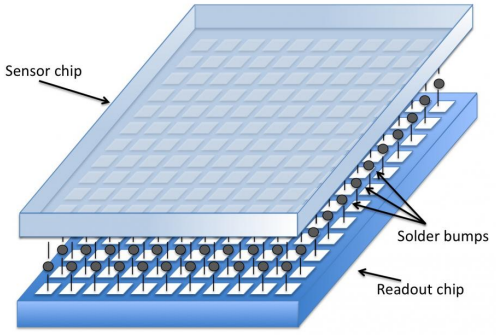


Figure 1.13: Illustration of a hybrid pixel detector.


Figure 1.14: Illustration of the layout of one sensor tile (or triple) for the upgrade. Three VeloPix ASICs share one planar silicon sensor.

### 1.4.2 VELO Modules and Cooling

Four hybrid pixel sensor tiles will be mounted on a module, two on either side and arranged in an "L" shape formation. Two L shaped modules, one on either side of the VELO will close around the LHC beam ensuring full coverage, as shown in Figure 1.15 (a). The backbone of the module is the cooling system. The upgraded cooling system uses micro-channel cooling technology, where micro-channels are etched into the 400 µm thick silicon substrate, as depicted in Figure 1.15 (b). Trenches 120 µm deep are etched into the silicon substrate, allowing evaporative $CO_2$ to flow through the channels. There will be 19 channels under each ASIC, maintaining the temperature at about -30°C. A thermal map from simulation shows a variation of less than 1°C between the micro-channels and the surface of the ASIC.

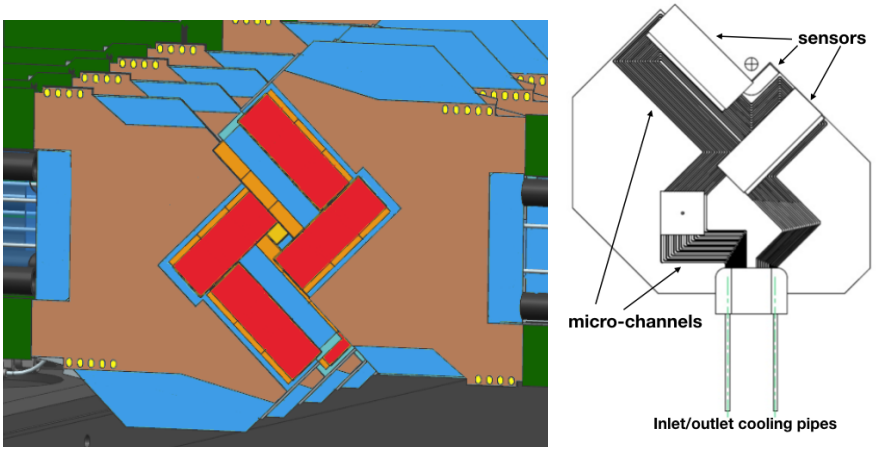


Figure 1.15: Illustration of VELO modules (a) and an illustration of the micro-channel cooling design (b).

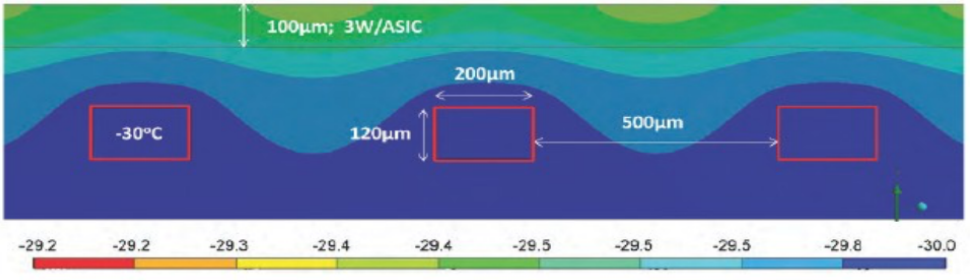


Figure 1.16: A thermal map from simulation, shows a variation of less than 1°C between the micro-channels and the surface of the ASIC.

### 1.4.3 RF foil

A new RF box has been designed to accommodate the new module geometry and allow a closer proximity to the beam line. The aluminium foil will have a reduced thickness of 250 µm to reduce the material and hence suppress multiple scattering effects. The thickness has been reduced in comparison to the current VELO (300 µm), however the RF foil is still the largest contribution to the material budget of the VELO, as shown in Figure 1.17 (b).

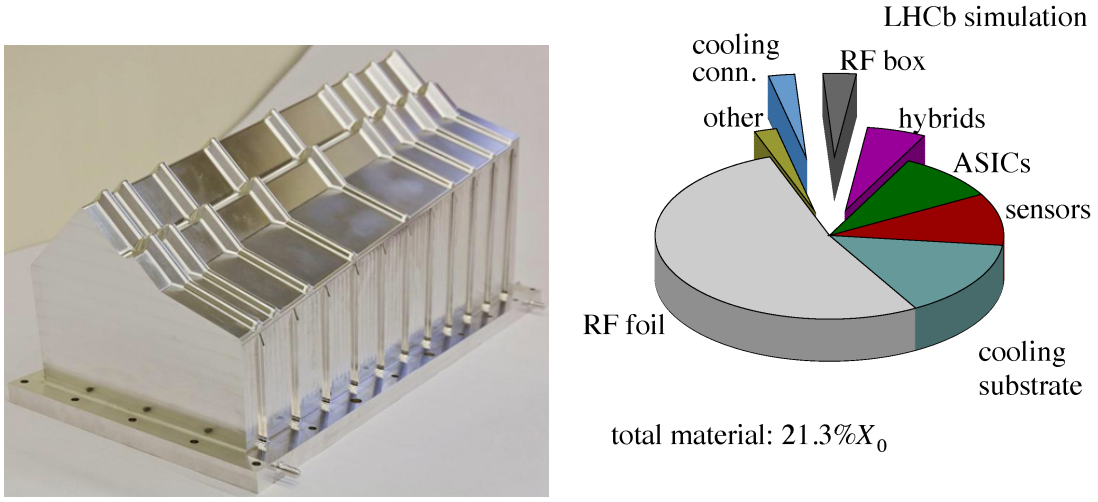


Figure 1.17: Photograph of a RF foil prototype (a) and the different contributions to the material budget of the VELO upgrade within the pseudorapidity range $2 < \eta < 5$ (b).

### 1.4.4 Occupancy and Radiation Doses

The occupancy as a function of radius is shown in Figure 1.18 (a), for the module stationed closest to the interaction point. This is where the occupancy will be the highest. The highest pixel (black) occupancy is ~ 0.125%. The cluster occupancy, where the predicted average cluster size will be size 2 is also shown (red). In Figure 1.18 (b), the charged particle density across one VELO module is shown and the average number of particles crossing each VeloPix ASIC from one event is overlain. Closest to the interaction region, the number of particles crossing an ASIC is ~ 8 and drops to less than 1 for the outer most ASICs.

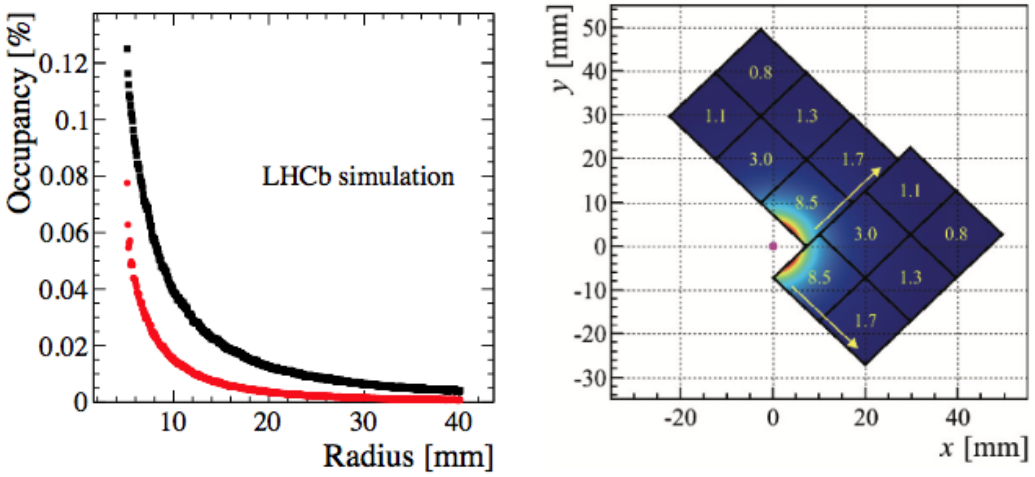


Figure 1.18: The occupancy as a function of radius for pixels (black) and for cluster, average size 2 (red) (a). The particle density across a VELO module and the average particles crossing each VeloPix ASIC (b).

The expected radiation damage per 1 $\text{fb}^{-1}$ under the upgrade conditions is shown in Figure 1.19. The vertical lines show the positions of the modules along the $z$ plane, where the p-p interaction region is at $z = 0$. The highest dose is concentrated at very low radii and is overall higher for modules closest to the interaction region. The inner most tip is required to withstand a maximum fluence of $8 \times 10^{15}$ $1\text{MeVn}_{\text{eq}}\text{cm}^{-2}$ after the full life time of the VELO (10 $\text{fb}^{-1}$).

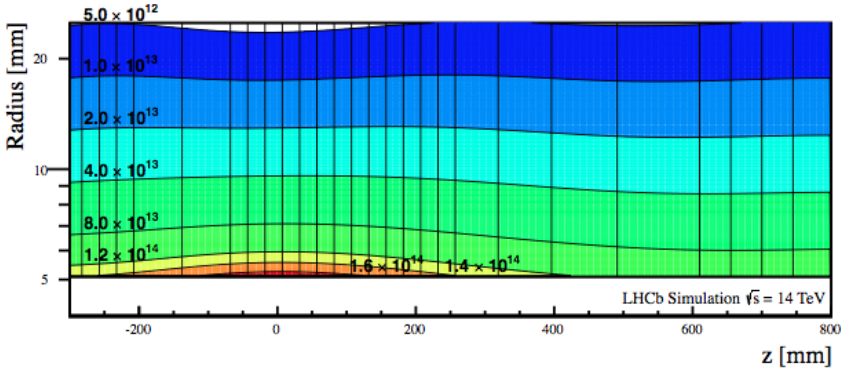


Figure 1.19: The integrated radiation dose per $\text{fb}^{-1}$ at upgrade upgrade conditions in units of $1\text{MeVn}_{\text{eq}}\text{cm}^{-2}$.

### 1.4.5 Impact Parameter Resolution

As previously described in Section 1.2.1, the impact parameter resolution is a key parameter of the VELO performance. Overall the upgraded VELO is expected to have a

better impact resolution. This is because of the improvements made: reducing the distance to the first measured point and reduced RF foil thickness. The simulated impact parameter resolution as a function of $1/p_T$ is shown in Figure 1.20, comparing the current VELO (black) to the upgraded VELO (red) [24]. The VELO upgrade modifications result in an improved impact parameter. For low $p_T$ multiple scattering is dominant, so reducing the material budget has helped improved the impact parameter resolution. For high $p_T$ the spatial resolution dominates (Equation 1.1) and the performance is similar for the current and upgraded VELO. The spatial resolution is a focus of this thesis and will be further discussed from Chapter 6 onwards.

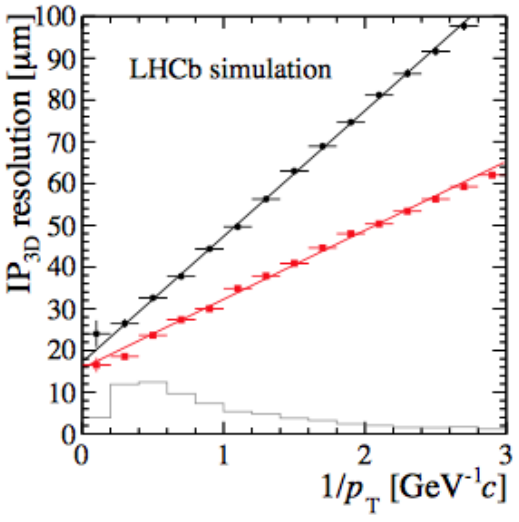


Figure 1.20: The impact parameter resolution as a function of the inverse of the transverse momentum for the current VELO (black) and the VELO upgrade (red). The relative population of $b$-hadron tracks in each bin is shown in light gray [24].

# Chapter 2

# Position Sensitive Semiconductor Detectors

The method of detecting a charged particle is to measure the electron-hole pairs left behind as it travels through a detection material. The energy deposited generates electron hole pairs that can be detected as electrical signals. The interaction of a charged particle with an array of detectors, separated spatially along the path of a particle, allows for its trajectory to be reconstructed. Currently silicon semiconductor devices are the most used detector type in tracking detectors. Silicon has the benefits of being a widely available material and has a relatively small band gap [25]. The first position sensitive semiconductor device was the silicon strip detector, with pixel detectors soon following. With the possibility of high granularity devices coupled to fast readout electronics they are suited for the high multiplicity and harsh radiation environments of particle physics experiments. This chapter will introduce the concepts of how charged particles interact with matter and how silicon semiconductor devices exploit these interactions to detect traversing particles. The very particles that the silicon devices are designed to measure are also damaging to their performance, therefore the different radiation damage mechanisms are also discussed.

## 2.1 Charged Particle Interactions with Matter

Charged particles mostly interact with matter via the electromagnetic interaction [1]. The two main consequences of the interaction are the loss of energy by the particle due to inelastic collisions with atomic electrons and the deflection of the particle from its incident direction due to elastic scattering from the nuclei [26]. The majority of the energy loss is from the inelastic collisions with the atomic electrons, causing excitation and ionisation. The energy transferred is only a small fraction of the total kinetic energy, where the average energy loss per unit path length $\langle \frac{dE}{dx} \rangle$ is described by the Bethe-Bloch formula:

$$-\left\langle \frac{dE}{dx} \right\rangle = \frac{4\pi N_A r_e^2 m_e c^2}{\beta^2} \frac{Z}{A} \left[ \frac{1}{2} \ln \frac{2m_e c^2 \beta^2 \gamma^2 T_{max}}{I^2} - \beta^2 - \frac{\delta(\beta\gamma)}{2} \right] \tag{2.1}$$

where $N_A$ is Avogadro's number, $r_e^2$ is the electron radius, $m_e c^2$ is the rest mass of the electron, $Z$ and $A$ are the atomic number and weight of the medium, $z$ is the charge of a traversing charged particle, $\beta$ is the ratio of the velocity to the speed of light, $\gamma$ is the Lorentz factor, $T_{max}$ is the maximum energy transfer in a single collision, $I$ is the mean excitation energy and $(\beta\gamma)$ is the density effect correction for high energy particles.

The formula describes the mean rate of energy loss in the region $0.1 \leq \beta\gamma \leq 1000$ and is often referred to as the stopping power. Figure 2.1 shows the stopping power for positive muons in copper as a function of $\beta\gamma$, where the region described by the Bethe-Bloch formula is highlighted in red. For low energies the $1/\beta^2$ term dominates, therefore the stopping power decreases rapidly as $\beta\gamma$ increases until a minimum is reached at $\beta\gamma \approx 3 - 3.5$. Particles with an energy loss at this minimum are called Minimum Ionizing Particles (MIPs) and most relativistic particles have a mean energy loss close to this minimum. Above the minimum, there is a gradual rise due to the logarithmic term $(\ln \beta\gamma)$.

For a charged particle traversing a material, the number of collisions occurring and the amount of energy transferred in each collision is subject to statistical fluctuations. The Bethe-Bloch formula is a good estimate of the average charge loss, however the actual

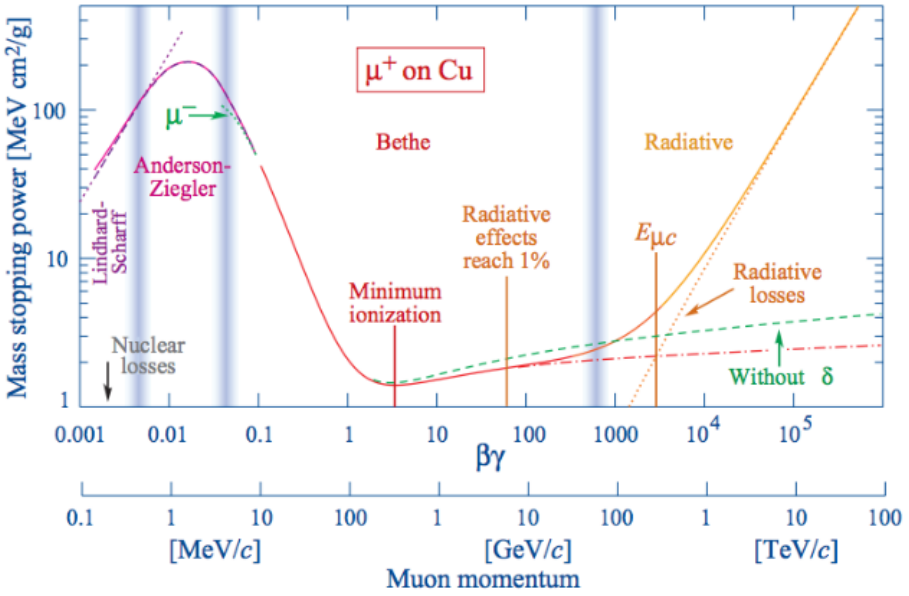


Figure 2.1: The stopping power ($-\langle\frac{dE}{dx}\rangle$) as a function of $\beta\gamma$. The region that the Bethe-Bloch formula describes is $0.1 \leq \beta\gamma \leq 1000$ and is highlighted in red [1].

energy loss is expected to differ due to these statistical fluctuations. For a relatively thick material, the number of collisions will be large and the distribution of energy losses will be roughly Gaussian [27]. For thinner materials, similar in thickness to detectors used in tracking detectors, the average energy loss is small but there are large fluctuations in the deposited energy. Dominating fluctuations come from high energy transfers to the atomic electrons, when the energy is large enough the ionised electrons can cause further ionisation, known as $\delta - rays$. This results in a largely asymmetric charge distribution, which is parametrised by the Landau distribution. Figure 2.2 shows the Landau distribution for different detector thicknesses. For thin detectors the distribution has a low broad peak with a large tail due to the $\delta - rays$. As the detector thickness increases, the peak value increases and the curve becomes more Gaussian in shape. This distribution is traditionally fit with a Landau convoluted with a Gaussian to extract the peak charge collection, the Most Probable Value (MPV) [28].

As previously discussed, in addition to the inelastic collisions with atomic electrons, the traversing charged particle can also repeatedly elastically scatter off nuclei. The path of a charged particle is altered by many small angle scatters due to multiple Coulomb scattering causing a deflection of the particle from its incident path, illustrated in Figure 2.3. Since the mass of the nuclei is much larger than the incident charged particle,

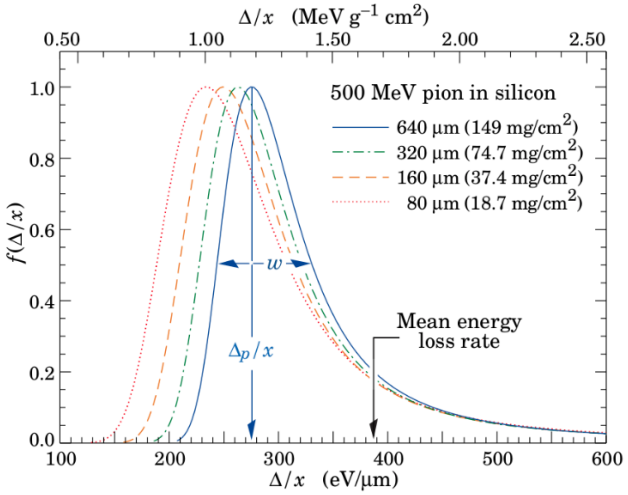


Figure 2.2: Example Landau distributions for in silicon for 500 MeV pions for different detector thicknesses.

the energy loss is negligible. The scattering distribution for small deflection angles is expected to be roughly Gaussian with a width given by:

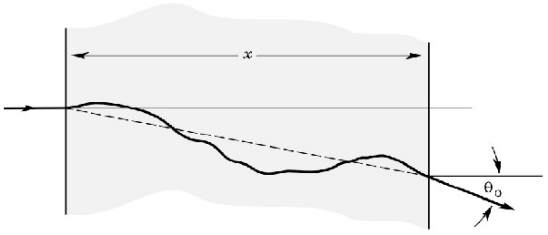


Figure 2.3: Sketch of a charged particle traversing a material where the trajectory is altered by many small scatters from multiple scattering with the atomic nuclei.

$$\theta_i = \frac{13.6\ MeV}{\beta cp} z \sqrt{x/X_0}\left[1 + 0.38 \ln\left(x/X_0\right)\right] \tag{2.2}$$

Where $p$, $\beta c$ and $z$ are the momentum, velocity and charge number of the incident particle and $x/X_0$ is the thickness of the material in radiation lengths. Therefore the largest multiple scattering occurs for low momentum particles traversing thick material layers.

To summarize, a particle can be detected by exploiting its interaction with matter. In silicon tracking detectors, several detection planes are placed spatially along the path of a charged particle. The energy deposited in each of the planes is used to reconstructed the trajectory of the particle. Energy loss and multiple scattering in each plane should be

kept to a minimum. This implies the use of a thin detection material that can generate a large enough charge signal with minimal energy loss.

## 2.2 Semiconductors

Silicon like all semiconductors has a valence band and conduction band separated by a forbidden region called the band gap [25]. For intrinsic silicon, free from impurities and at low temperatures, the valence band is full and the conduction band is empty as illustrated in Figure 2.4 (left). Under these conditions the number of electrons is equal to the number of holes resulting in a net equilibrium of charge. At higher temperatures thermal vibrations may allow electrons to be excited to the conduction band, Figure 2.4 (right).

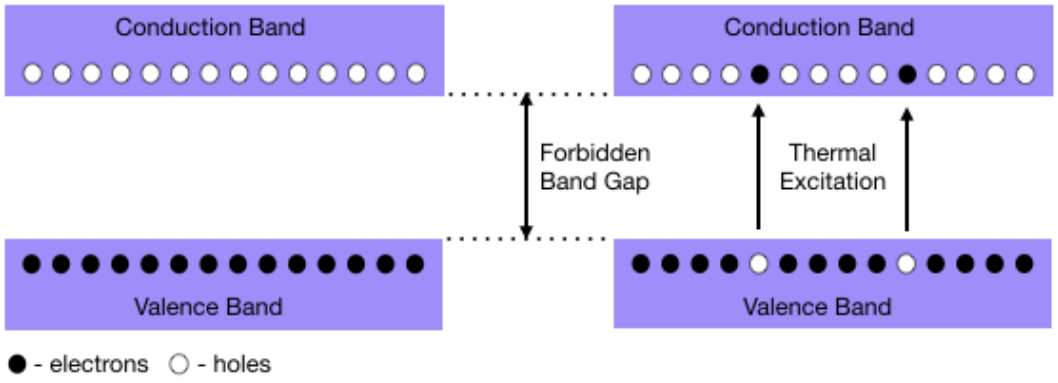


Figure 2.4: Illustration of the valence and conduction band in a semiconductor. The conduction bad is empty at low temperatures (left) and thermal vibrations at higher temperatures can lead to electrons being excited into the conduction band (right).

Additional states in the forbidden region can be introduced to increase the probability to excite electrons or holes, this process is called "doping". This is achieved by replacing atoms in intrinsic silicon with foreign atoms with more or less valence electrons. By adding a material like arsenic that contains 5 valence electrons, a donor, an excess in electrons occurs and an n-type material is produced. By introducing impurities like boron that contains 3 valences electrons, an acceptor, an excess of holes occurs and a p-type material is produced. This process is illustrated in Figure 2.5.

Homogeneous semiconductors are not suitable for particle detection as there are too many free electrons. Typically in silicon sensors used in high energy physics there

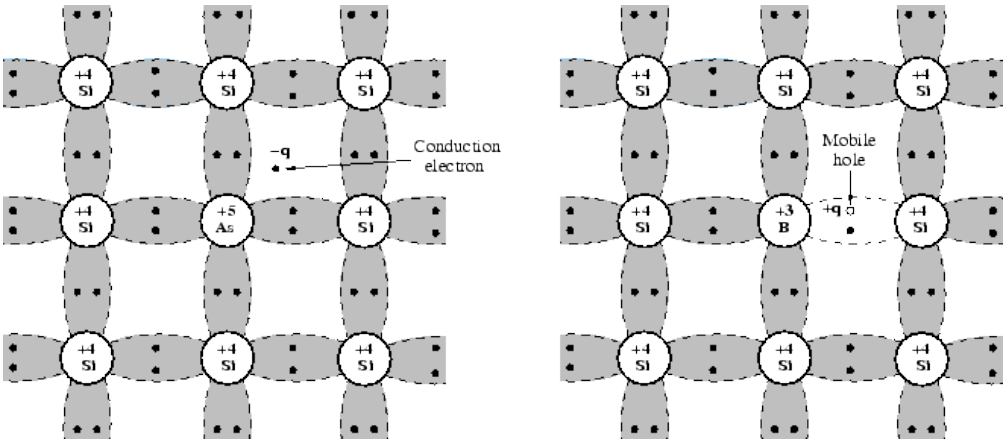


Figure 2.5: Sketches showing the doping process. Doping silicon with arsenic turns the material to n-type and doping with boron turns the material to p-type.

are $\sim 10^9$ free carriers but only $\sim 2 \times 10^4$ generated electrons induced by an ionizing particle [29]. This means that a generated signal would be lost in a sea of free carriers. One way to reduce the number of free charge carriers in silicon would be to cool it down to extremely low temperatures, or the alternative is to deplete the silicon volume of free of any charge carriers with the use of a p-n junction [23].

### 2.2.1 p-n Junctions

The joining of n-type and p-type materials creates a p-n junction. This naturally causes the free charge carriers to move into the opposite regions, with electrons diffusing to the p region and holes to the n region. This results in an excess of negative charge in the p region and positive charge in the n region, creating an electric field counteracting the diffusion. The electric field sweeps away any free charge carriers in the region around the boundary producing a space charge region (SCR). This is often referred to as the depletion zone, the width of which can be further increased with the application of an external voltage, see Section 2.2.3. Ionizing particles travelling through the material generate charge in the form of electron-hole pairs which are then separated by the electric field of the depleted region, and collected at the junction.

### 2.2.2 Carrier Motion

There are two types of motion of the charge carriers in semiconductors: drift and diffusion. Drift describes the motion of charged particles in the response to an electric field and diffusion describes the natural movement of charges from areas of high concentration to areas of low concentration. The flow of current in a semiconductor is described by the current density [15]

$$\boldsymbol{J} = \boldsymbol{J}_{drift} + \boldsymbol{J}_{diffusion} \tag{2.3}$$

where $\boldsymbol{J}_{drift}$ is the drift current and $\boldsymbol{J}_{diffusion}$ is the diffusion current. The drift current $\boldsymbol{J}_{drift}$ for electrons is given by

$$\boldsymbol{J}_{drift} = -en\boldsymbol{v}_e \tag{2.4}$$

where $e$ is the electron charge, $n$ is the free electron density and $\boldsymbol{v}_e$ is the drift velocity of electrons. The drift velocity is dependant on the electric field $\boldsymbol{E}$

$$\boldsymbol{v}_e = -\mu_e \boldsymbol{E} \tag{2.5}$$

where $\mu_e$ is the electron mobility. A similar expression can be given for the motion of holes, giving the overall drift current

$$\boldsymbol{J}_{drift} = (en\mu_e + ep\mu_h)\boldsymbol{E} = \sigma \boldsymbol{E} \tag{2.6}$$

where $p$ is the is hole density and $\mu_h$ is the mobility of holes. This constant of proportionality is the conductivity $\sigma$ of the silicon, which is related to the resistivity $\rho$

$$\rho = \frac{1}{\sigma} = \frac{1}{en\mu_e + ep\mu_h} \tag{2.7}$$

The diffusion current $\boldsymbol{J}_{diffusion}$ is given by

$$\boldsymbol{J}_{diffusion} = eD\nabla_n \tag{2.8}$$

where $D$ is the diffusion coefficient and $\nabla_n$ is the concentration gradient. The diffusion coefficient is related to the $\mu$ by Einstein's relation

$$D = \frac{\mu kT}{e} \tag{2.9}$$

where $k$ is the Boltzmann constant and $T$ is the temperature in Kelvin.

The $\boldsymbol{J}_{diffusion}$ is simplified to

$$\boldsymbol{J}_{diffusion} = \mu kT \nabla_n \tag{2.10}$$

Therefore the current density for electrons can now be written as

$$\boldsymbol{J} = en\mu_e \boldsymbol{E} + \mu kT \nabla_n \tag{2.11}$$

As previously mentioned the diffusion current depends on the slope of the carrier concentration $\nabla_n$ and is influenced by random thermal motions in the crystal lattice. The spread of charge can be described as a Gaussian distribution with a standard deviation $\sigma$

$$\sigma = \sqrt{2Dt_d} \tag{2.12}$$

where $t_d$ is the drift time. This means that the charge spread is larger for longer drift times. The width of the charge cloud for the VELO upgrade prototype sensors is expected to be around 5 - 10 µm.

### 2.2.3 Position Sensitive Devices

A pixel detector is a series of segmented p-n junctions, such that the charge generated can be split between more than one readout electrode with the ratio of charges depending on the position [23]. An illustration is shown in Figure 2.6, where highly doped n-type ($n^+$) implants are separated along the surface of a lightly doped p-bulk sensor. Because the implant is heavily doped in comparison to the bulk the depletion region extends into the less heavily doped side. Along the back of the sensor is a highly doped p-type ($p^+$)

backplane to cut off the electric field. The turquoise shaded area represents regions which are depleted. The size of the depleted region is dependent on the bias voltage. With increasing bias voltage the depleted area increases horizontally and vertically. Since the spacing between the implants is much smaller than the thickness of the sensor, the depleted areas first merge well before the entire sensor is depleted. A charged particle can be seen travelling through the sensor creating electron-hole pairs. Those created in the depleted region are separated, with the electrons travelling towards the implant. If the full thickness is not depleted, charge is still generated in the neutral regions. This charge has a very small chance of reaching the depleted region by diffusion but almost all charge carriers will combine with free carriers and be lost. Therefore in the operation of silicon sensors, it is advantageous to operate the device such that the full volume is depleted to ensure full collection of the signal. Given the negligible depth of the implant, the depletion width $x_d$ is governed by the bulk type and can be calculated using the relation [30]:

$$x_d = \sqrt{\frac{2\epsilon(V_{bi} + V)}{e}\left(\frac{1}{N_a} + \frac{1}{N_d}\right)} \tag{2.13}$$

where $\epsilon$ is the permittivity of the material, $N_a$ and $N_d$ are the doping concentrations for p-type (acceptor) and n-type (donor) materials, respectively. $V_{bi}$ is the built in voltage, created at the joining of the p-n junction and the $V$ is the external bias voltage applied to extend the depletion width. Taking the bulk doping to be $N$, and ignoring the built in voltage (typically $< 1$ V), the relation simplifies to

$$x_d = \sqrt{\frac{2\epsilon V}{eN}} \tag{2.14}$$

Therefore the voltage required to deplete the full thickness of the sensor $d$ is:

$$V_{dep} = \frac{eNd^2}{2\epsilon} \tag{2.15}$$

Given the resistivity $\rho$ (in Equation 2.7) the $V_{dep}$ becomes:

$$V_{dep} = \frac{d^2}{2\epsilon\mu\rho} \tag{2.16}$$

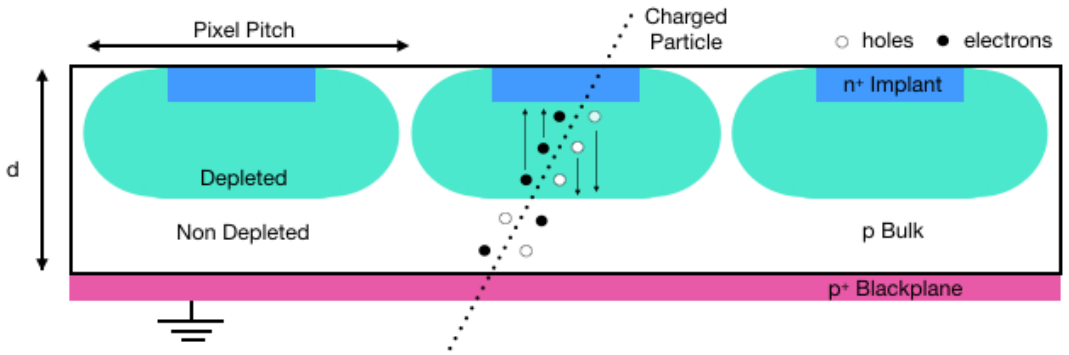


Figure 2.6: Illustration of a n-on-p type pixel detector. Traversing charged particles create electron hole pairs and electrons generated within the depletion region are collected at the implant.

As discussed above, if the sensor bulk is not fully depleted, then not all of the generated charge is collected. This can be shown using data collected at testbeam, further discussed in Section 4.2. Figure 2.7 shows an example of the collected charge distributions for a 200 µm thick sensor operated at four different bias voltages. The charge is measured in units of Time over Threshold (ToT), introduced in Section 3.2. The peak of the charge distributions increase with increasing bias until 40 V. The charge distribution measured at 80 V lies almost directly on top of the 40 V distribution, suggesting that the full sensor thickness is depleted and no additional charge signal can be collected. This also suggests that the depletion voltage is between 20 and 40 V. This can be confirmed by fitting the charge distributions with a Landau convoluted with a Gaussian to extract the MPV, previously described in Section 2.1. The measured MPV is plotted for a range of bias voltages shown in Figure 2.8. The ToT values were converted to electrons using the calibration method described in Section 4.1.4. The MPV increases with increasing bias until a point where the collected charge begins to plateau, the point at which is when the sensor is fully depleted. For this example the sensor has a depletion voltage $\sim$ 40 V.

The high voltage capability of a sensor is limited by the high electric field generated at the edge. Therefore multiple guard rings are implemented around the periphery of the pixel matrix. The purpose of the multi guard rings is to establish a smooth voltage drop, where the number of rings depends on the maximum target bias voltage. The guard rings are a necessary feature however they introduce an inactive area around the pixel matrix. In the case of the VELO, this increases the distance from the first measured

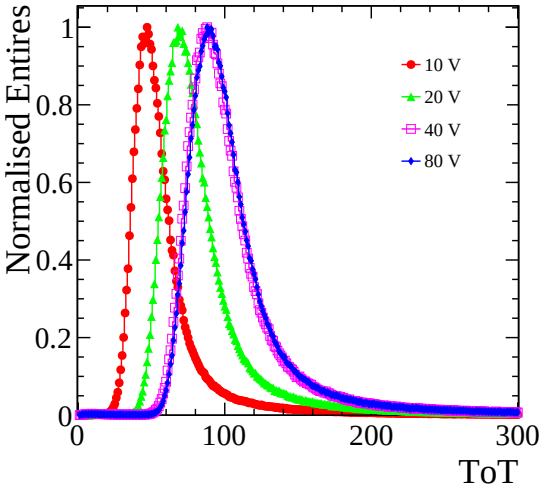


Figure 2.7: The collected charge distributions for different bias voltages depending on their Time over Threshold (ToT).

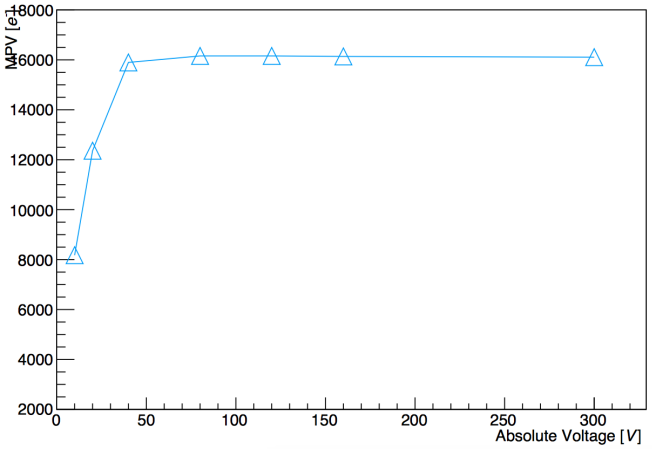


Figure 2.8: The charge MPVs as a function of bias, where the depletion is seen at ~40 V, taken from [28].

point and contributes to the overall material budget of the detector. Illustrations of different guard ring designs are shown in Section 3.1.

### 2.2.4 Leakage Current

The idea of the bias voltage is to create a depleted region free of charge carriers, so that no current can flow unless generated by traversing charged particles. However, thermal excitation can allow electrons to cross the bandgap (see Figure 2.4 (right)), even in the absence of a charged particle. The probability of thermal excitation of electrons is increased strongly by the presence of impurities in the lattice, because they introduce

additional energy states in the bandgap. This flow of current is called the leakage current and is given by

$$I(T) \propto T^2 e^{-(\frac{E_g}{2kT})} \tag{2.17}$$

where $T$ is the temperature in Kelvin, $E_g$ is the band gap energy and $k$ is Boltzmann constant. The leakage current increases the noise, therefore sensors are often operated at low temperatures to decrease the probability of thermal excitations.

## 2.3 Radiation Damage

The charged particles that silicon detectors are designed to detect are also damaging to the device itself. As previously discussed, traversing particles interact with the atomic electrons and nuclei within the silicon. The interaction with the atomic electrons causes ionisation which leads to a measurable signal and is a short lived process that does not damage the material (or limited damage). Interactions with the nuclei can lead to permanent changes to the lattice defects of the material [25], which can degrade the performance of the device. Radiation damage is split into two types: surface and bulk. For devices operated at the LHC and HEP experiments in general, bulk damage is the biggest contribution to the radiation damage experienced by a silicon detector.

### 2.3.1 Bulk Damage

Interactions of highly energetic particles with nuclei, can displace an atom from the crystal lattice creating a point defect. These defects create additional energy levels in the band gap that can act as generation and recombination centres. The levels created close to the edge of the valence band act as acceptors changing the effective doping concentration of the material. It was shown in Equation 2.16 that the voltage required to deplete a sensor is inversely proportional to the doping concentration. Therefore for p-type materials, with increasing radiation damage the voltage required to deplete the device increases. For n-type, the effective doping concentration initially decreases meaning that the depletion voltage decreases. However eventually the n-type material becomes p-type, such that the depletion voltage required increases. The variation in the

depletion voltage and effective doping concentration as a function of fluence is shown in Figure 2.9. This process is referred to type-inversion [31] and is a very unfavourable effect because after type inversion the depletion zone grows from the heavily-doped layer in the backplane rather than from the segmented implant side. Therefore, for the device to perform as it should, the sensor would always need to be fully depleted, which is challenging for heavily irradiated devices. As a result, often n-type bulk is avoided and p-type bulk is preferred in high radiation environments.

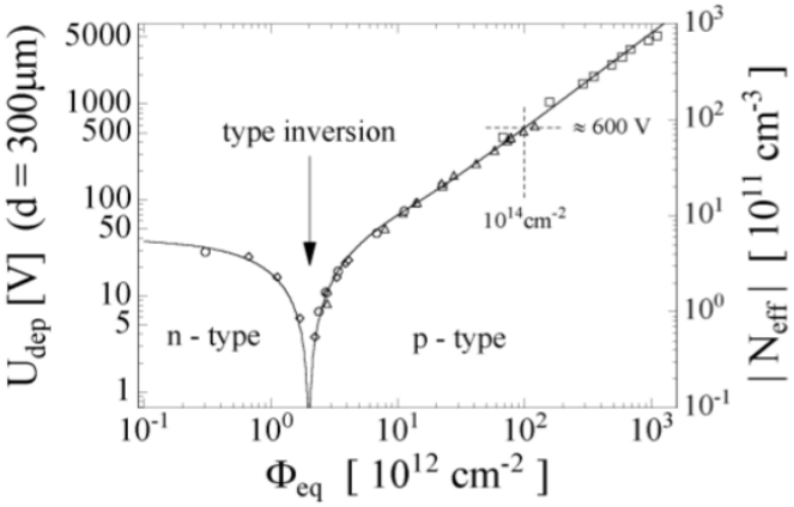


Figure 2.9: The voltage required to deplete a sensor and the change in the effective doping concentration as a function of fluence [31].

The current VELO uses n-on-n type silicon strip sensors and the type inversion of the VELO sensors was seen during the 2012 and 2013 data taking. The effective depletion as function of fluence for all $R$ and $\phi$ sensors is shown in Figure 2.10 [32]. The colours represent the different region of the sensor, with red being the strips closest to the interaction region and blue being the furthest from the interaction region. The depletion voltage decreases with fluence to a minimum of -18 V for the n-type bulk sensors. At this point, type inversion occurs at $\sim 10 - 15 \times 10^{12}$ 1MeVn$_{\text{eq}}$cm$^{-2}$, after which the depletion voltage increase is at a similar rate as the n-on-p. As previously mentioned in Section 1.2.1, one of the most upstream modules of the VELO uses n-on-p sensors. These sensors do not experience type inversion, therefore the depletion voltage only increases with increasing fluence. All of the VELO sensors are currently operating at

their effective depletion voltage or above and therefore type inversion does not yet have any detrimental effects on the charge collection.

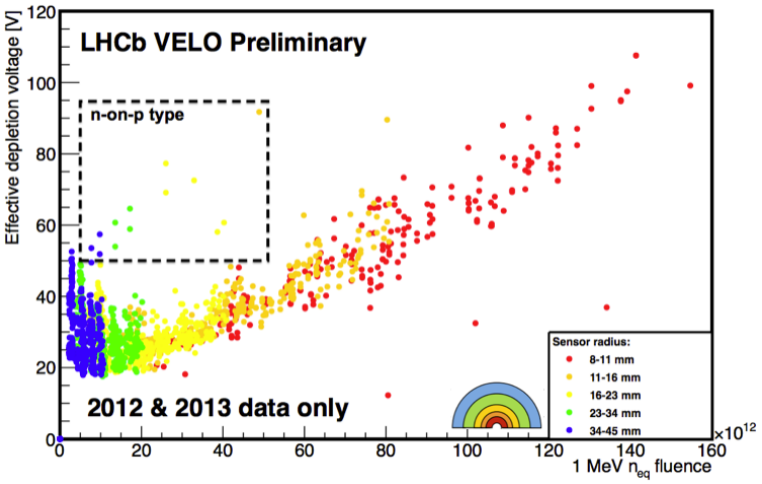


Figure 2.10: The effective depletion voltage of all sensors installed in the current VELO. The colours represent different regions of the sensor, where the radial bins are illustrated. Type inversion occurs at $\sim 10 - 15 \times 10^{12}$ $1\text{MeVn}_{\text{eq}}\text{cm}^{-2}$ [32].

As a result of the additional energy levels close to the valence band, thermal generation of charge carriers is easier. This results in an increase of current, referred to as the leakage current $I$, previously discussed in Section 2.2.4. The magnitude of this scales linearly with the fluence $\Phi$, where:

$$I = \alpha \Phi V \tag{2.18}$$

$\alpha$ is the current related damage rate and $V$ the active volume. Figure 2.11 shows the leakage current of different silicon detectors, as a function of fluence. It is seen that the damage rate is independent of the material type, process technology and the irradiation type and scales linearly with $\Phi$.

The leakage current has been constantly monitored throughout the operation of the current VELO. The leakage current for all sensors on one half of the VELO is shown in Figure 2.10. The measurements were taken at different periods: start of Run 2 after 3.23 $\text{fb}^{-1}$ of data (black), End of Year Shutdown 2015 after 3.56 $\text{fb}^{-1}$ (red), End of Year Shutdown 2016 after 5.23 $\text{fb}^{-1}$ (blue) and August 2017 after 6 $\text{fb}^{-1}$ (pink). The leakage currents are highest for modules closest to the interaction region at $z = 0$ and the overall leakage currents increase as the magnitude of collected data increases. The magnitudes of current measured in August 2017 after 6 $\text{fb}^{-1}$ are almost double that measured at

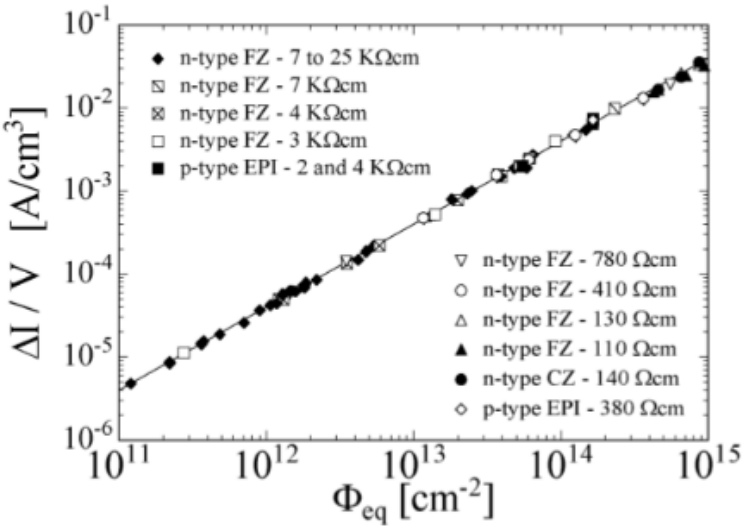


Figure 2.11: The leakage current as a function of fluence for different silicon sensors. The current scales linearly with $\Phi$ independent of the sensor and radiation type [31].

the beginning of Run 2 after 3.23 fb$^{-1}$, showing the linear nature of the leakage current increase with fluence.

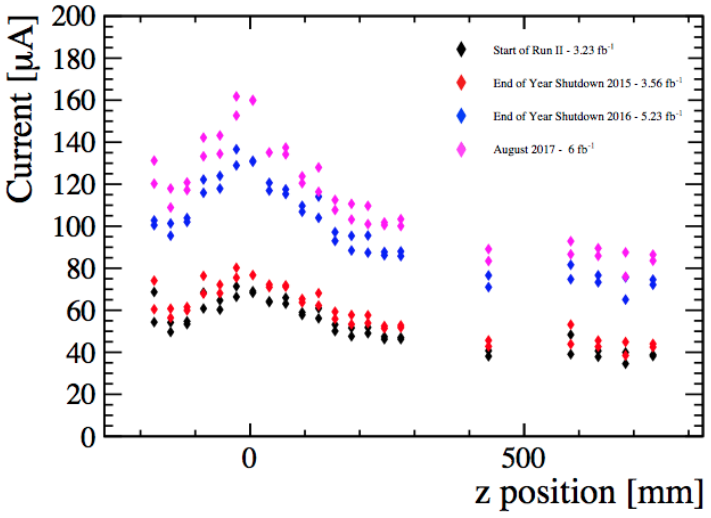


Figure 2.12: The leakage currents of sensors from one half of the VELO taken over four different periods of operation [33].

Furthermore, the increased leakage currents produce an additional source of heat. This in turn, causes a further increases in current. This is an avalanche effect referred to as thermal runaway. Therefore to suppress the leakage current, the sensors are usually operated at cold temperatures. This is one of the main motivations for the improved cooling system for the upgraded VELO. The micro-channels are etched as close to the tip of the sensor as possible to reduce the probability of thermal run away.

The additional energy levels in the depletion zone can also act as trapping centres, where electrons and holes can be captured and emitted with some time delay. If the trapping time is too long, the charge could be released too late for efficient detection and the collected signal is reduced. The trapping rate $1/\tau$ is dependent on the fluence and is given by the relation

$$\frac{1}{\tau_c} = \beta_c \Phi \tag{2.19}$$

where $\tau_c$ is the trapping rate dependant on the carrier type and $\beta_c$ is a fit parameter. The probability of charge being trapped is dependant on the velocity of the charge carriers. At higher voltages the charge carriers travel faster and hence have less probability to get captured.

To summarize, radiation has a damaging effect on the performance of a silicon sensor. The voltage required to deplete a p-bulk sensor increases with increasing fluence. The same is true for n-bulk sensors, but only after type-inversion, before which the depletion voltage initially decreases. The leakage current increases linearly with fluence and is largely dependent on the temperature. Large leakage currents create noise, decreasing the sensors S/N. Also, the heat generated from increased currents can cause an avalanche effect called thermal run away, that if great enough can destroy the sensor. Radiation induced trapping centres can decrease the collected charge, however the probability of trapping can be decreased by increasing the bias voltage.

# Chapter 3

# Sensor Prototypes and Requirements

In choosing the design of a silicon sensor there are many factors that must be considered, for example substrate type, thickness, guard ring and implant size. The main drivers in the design are the physics requirements (introduced in Section 1.2.1). For the VELO, the forward geometry of the detector and close proximity to the interaction region require a sensor which is highly radiation tolerant and able to cope with a highly non-uniform radiation profile. Often a p-type bulk is preferred as there is no type-inversion after prolonged radiation exposure and an n-type implant collecting electrons is faster than the collection of holes using a p-type implant. When considering the thickness, there is a trade-off. The greater the thickness of a sensor the higher the charge generation. However, thicker sensors lead to an increased material budget in the detector which increases the multiple scattering and therefore degrades the tracking performance. On the other hand, thinner sensors can be harder to handle mechanically and have a lower bump bonding yield. The guard rings are required to be as thin as possible to limit the inactive material around the periphery of the sensor, minimising the distance of the first active pixel to the interaction region.

In this chapter the different types of prototypes will be described, the TimePix3 ASIC used for the prototype testing is introduced and the performance requirements will be

| Vendor | Type | Thickness (μm) | Guard Ring (μm) | Implant (μm) |
|---|---|---|---|---|
| Hamamatsu (HPK) | n-on-p | 200 | 450 & 600 | 35 & 39 |
| Micron | n-on-p | 200 | 250 & 450 | 36 |
| Micron | n-on-n | 150 | 250 & 450 | 36 |

Table 3.1: Summary of the prototype sensors provided by manufacturers HPK and Micron.

discussed. Many of the requirements are for the prototypes to perform well in harsh radiation environments, therefore the irradiation program of the prototypes is introduced as well.

## 3.1 Prototype Design

Based on simulations presented in the VELO TDR [5], it was decided that the baseline design would be a 200 μm thick sensor with a p-bulk and n-type implants and guard rings size of 450 μm or less. There was a series of orders from two vendors, Hamamatsu (HPK) and Micron to produce a range of prototype sensors to be tested. A summary of the prototypes is given in Table 3.1. HPK provided 200 μm thick n-on-p sensors with implant sizes 35 μm & 39 μm and guard rings sizes 450 μm & 600 μm. The option of n-on-n sensors from HPK was possible, however due to a significantly longer delivery time it was not pursued. Micron provided both n-on-p and n-on-n sensors with the former having a thickness of 200 μm and the latter 150 μm. Both sensors have an implant width of 36 μm and an inactive edge of 250 μm or 450 μm.

Two different guard ring designs were adopted for the n-on-p and n-on-n sensors. The n-on-p design uses the traditional, single sided planar technology where the guard rings surround the outside of the active area up to the physical edge of the sensor, illustrated in Figure 3.1 (left). The n-on-n sensor's guard rings are implanted on the backplane of the sensor, illustrated in Figure 3.1 (right). This requires double sided processing which leads to a higher cost in comparison to the traditional design. However it reduces the distance to the edge as a fraction of the guard rings lie below the active area of the sensor, which is an attractive design choice for the VELO. The performance of the two guard ring designs are shown in Section 5.4.

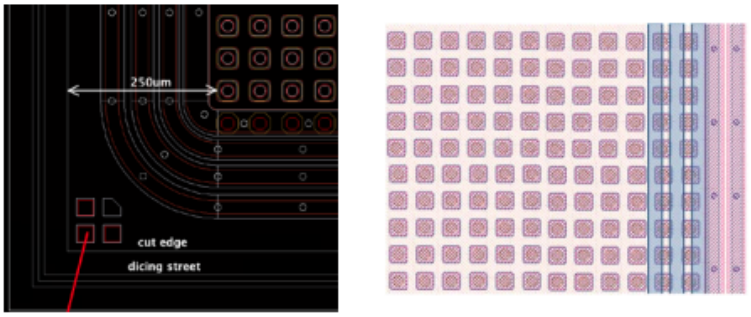


Figure 3.1: The guard ring design for Micron n-on-p (left) and n-on-n (right). For n-on-p, the guard rings are around the outside of the pixel area, whereas for n-on-n, the guard rings lie underneath the first two pixels around the periphery of the sensor.

The sensors were produced on a series of wafers, an example is shown in Figure 3.2. Typically two different sensor sizes were produced on the same wafer to optimise the use of the available area. In the example, the wafer has 12 "triples" and 14 "single" assemblies. The triple sensor design is the one that will be adopted in the VELO upgrade and will accommodate three readout ASICs as discussed in Section 1.4.1. The single sensors are produced solely for testing purposes and will accommodate only one readout ASIC.

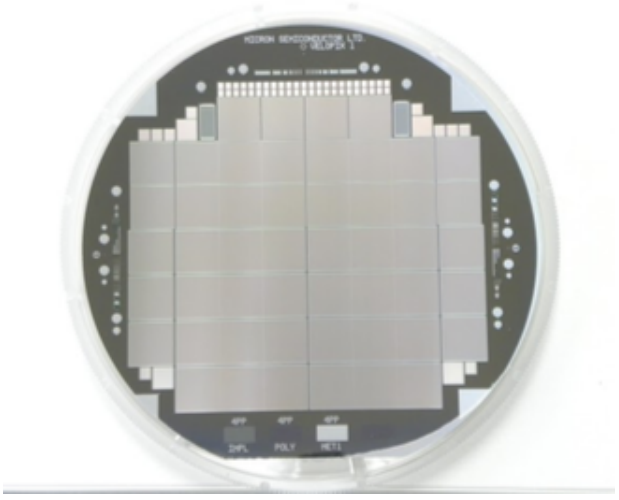

Figure 3.2: Photograph of a prototype Micron sensor wafer.

For the triples, a modification to the pixel matrix on the sensor was required. When the ASICs are diced there is a margin of inactive area around the periphery, therefore when three ASICs share one single planar sensor there will be "dead material" between neighbouring ASICs. To eliminate this inactive area, elongated pixels were introduced in the sensor pixel matrix to bridge the gap. This is illustrated in Figure 3.3 where two

columns of elongated pixels are placed between nominal 55 µm pixels. For the first round of prototypes the elongated pixels had a width of 110 µm. This was later increased to 137.5 µm for the second round of prototypes to allow a larger margin for the dicing of the ASIC wafers.

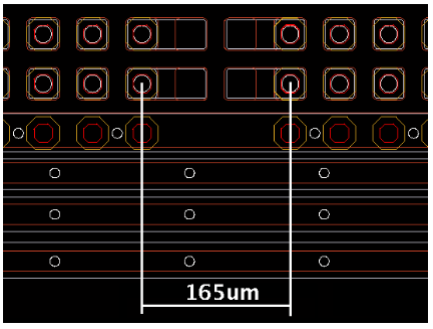


Figure 3.3: Illustration of elongated pixels of size 110 µm, bridging the gap between adjacent ASICs. This results in a distance between the two bonding pads of 165 µm.

The sensors were then diced and bonded to the readout ASICs. The use of hybrid pixel detectors has a great advantage that it allows the sensor and ASIC to be optimised separately. The TimePix3 ASIC (further discussed in Section 3.2) was used for the majority of prototype testing campaign allowing the further development of the TimePix3 into the VeloPix in parallel. A photograph of an example triple sensor bonded to a TimePix3 ASIC is shown in Figure 3.4.

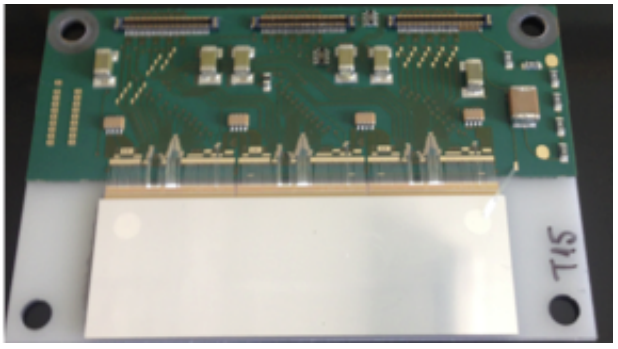

Figure 3.4: Picture of a prototype assembly of a triple sensor bonded to the TimePix3 ASIC.

| | TimePix3 | VeloPix |
|---|---|---|
| Pixel Arrangement | $256 \times 256$ | $256 \times 256$ |
| Pixel Size | $55 \times 55$ µm | $55 \times 55$ µm |
| Peak Hit Rate | 80 Mhits/s/ASIC | 800 Mhits/s/ASIC |
| Readout Type | trigger-less analogue (ToT) | trigger-less binary |
| Power Consumption | <1.5 W | <2 W |
| Max. Data Rate | 5.12 Gbps | 20.48 Gbps |

Table 3.2: Comparison between the TimePix3 and VeloPix ASICs.

## 3.2 Timepix3 ASIC

The TimePix3 is the predecessor of the VeloPix ASIC [6]. It is designed in 130 nm CMOS technology and has a matrix of $256 \times 256$ pixels each with a pitch of 55 µm. The readout is data driven and uses the super-pixel readout method. Table 3.2 compares the difference in the VeloPix and TimePix3 specifications. A key difference between the VeloPix and the TimePix3 is that the TimePix3 has an analogue readout, making it an excellent ASIC for prototype testing because it provides charge information. This additional information provided by the TimePix3 means its maximum data rate is lower, however still sufficient for the prototype testing. A schematic of the front-end electronics of one pixel and the super-pixel logic is shown in Figure 3.5 [34]. An induced signal at the input pad is amplified by the pre-amplifier and the output is compared to a threshold. The threshold value is set as a global threshold to all pixels, the method of determining the operational threshold is further discussed in Section 4.1.3.

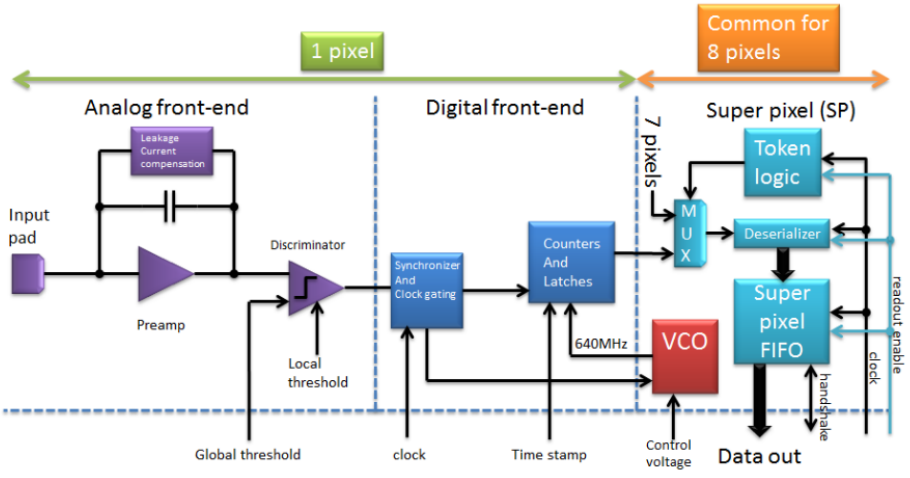


Figure 3.5: The schematic for one pixel and super pixel of a Timepix3.

The TimePix3 can be operated in different acquisition readout modes including: counting, Time of Arrival (ToA) and Time over Threshold (ToT). For the prototype testing, the TimePix3 provided simultaneous measurements of the ToA and ToT per pixel. The ToT mode measures the time that the signal in the pixel is above a certain threshold, as shown in Figure 3.6, and the ToA provides a timestamp of when the signal first crosses threshold. The ToT is an indirect measurement of the amount of charge deposited in the pixel. A high charge pulse (T2), will spend a longer time over threshold and a small charge pulse (T1) will spend a shorter time over threshold. The ToT values can then be calibrated using the method described in Section 4.1.4. Theoretically, two particles coming from the same bunch crossing should cross threshold at almost the same time. However, in reality, the time that the signal reaches the threshold depends on the magnitude of the induced pulse. This effect is called time-walk.

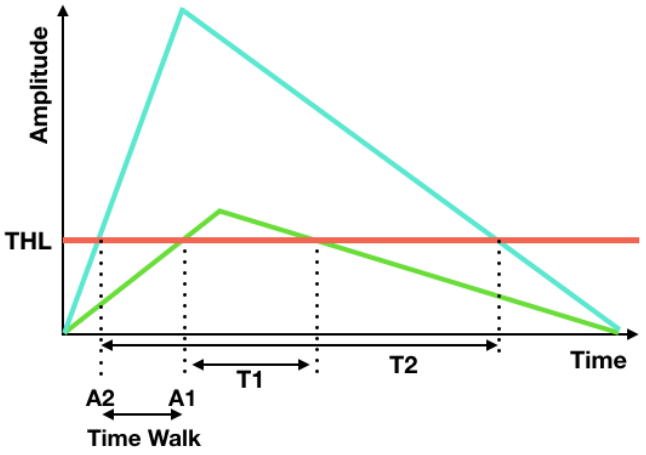


Figure 3.6: Illustration of the ToA and ToT for a small signal (A1/T1) and a large signal (A2/T2).

## 3.3 Sensor Performance Requirements

There are many parameters that define the performance of a silicon sensor. For example, depletion and breakdown voltages, the signal yield (charge collection) and the spatial resolution. These parameters are expected to degrade with increasing radiation exposure. Over the operational period of the upgraded VELO, the detector is expected to accumulate an integrated flux of up to $8 \times 10^{15}$ $1\text{MeVn}_{\text{eq}}\text{cm}^{-2}$. The effects of radiation damage were previously described in Section 2.3. To summarize, the leakage current will

increase linearly with fluence, charge will be lost due to radiation induce trapping centres and the voltage required to deplete the sensor increases. The performance requirements were outlined in the TDR [5] and to maintain a sufficient operational performance over the lifetime of the upgraded VELO the sensors are required:

- To maintain a good Signal to Noise (S/N), the sensors must collect more than 6000$e^-$ at the end of the lifetime of the VELO.
- The maximum bias voltage that the VELO power supplies can provide is 1000 V. The sensors must be able to collected the required charge of 6000$e^-$ below 1000 V and tolerate the maximum voltage without breakdown.
- A uniform charge collection efficiency >99% over the full pixel area is required before and after irradiation.
- The TDR does not state a requirement for the spatial resolution, therefore the performance of the current VELO can be used as a benchmark. The current VELO uses silicon strip sensors with varying strip pitches and has an analogue readout as described in Section 1.2.1. The spatial resolution as a function of angle was previously shown in Figure 1.6 (b). The spatial resolution resolution varies between $\sim$ 4.3 µm and $\sim$ 18 µm. The upgrade sensors will have a binary readout and hence the spatial resolution is expected to be slightly worse. The spatial resolution is the topic of this thesis and is further discussed in Chapters 6 and 7.

## 3.4 Irradiation Program

The performance requirements discussed above mostly focus on the performance after radiation exposure. This is because it is crucial that the sensors are able to perform well after years of operation and exposure to the harsh radiation environments of the LHC. Therefore the sensors need to be tested both before and after radiation exposure. A subset of the available prototypes were sent to different irradiation facilities, where they were uniformly and non-uniformly irradiated. These refer to the radiation profiles across the sensors. Uniformly irradiated sensors are studied to directly compare the

spatial resolution, timing and the charge collection and hit efficiencies between different prototypes sensors and vendors. The non-uniformly irradiated sensors most closely represent the radiation profile expected in the VELO and are used to test the high voltage tolerance of the prototypes. Different sensors were exposed to different magnitudes of fluence. Most were exposed to the full fluence of $8\times10^{15}$ 1MeVn$_{\text{eq}}$cm$^{-2}$ and a few others were exposed to half the fluence of $4\times10^{15}$ 1MeVn$_{\text{eq}}$cm$^{-2}$ or $\sim 1\times10^{15}$ 1MeVn$_{\text{eq}}$cm$^{-2}$. The majority of the analyses presented in this thesis were performed on uniformly irradiated sensors with the exception of Current-Voltage studies presented in Section 4.1.2. A more detailed description of the irradiation facilities and procedures are presented in [28].

## 3.5 Summary of Prototypes

A summary of all sensors presented in this thesis is given in Table 3.3. Sensors with names beginning with "S" identify those that are "single" assemblies and "T" identifies "Triples". If the sensors were irradiated, the profile and magnitude of fluence is given. The HPK sensors are 200 µm thick n-on-p sensors, with two different implant sizes (35 & 39 µm) and guard rings size options (450 & 600 µm). The Micron n-on-p sensors are 200 µm, which also have two different implant size (35 & 36 µm) and guard rings size options (250 & 450 µm). The Micron n-on-n sensors are 150 µm thick and have an implant size of 36 µm and two different guard ring size options (250 & 450 µm).

| Sensor | Vendor | Type | Thickness [µm] | Implant [µm] | Guard Ring [µm] | Irradiation Profile | Fluence $1\text{MeVn}_{\text{eq}}\text{cm}^{-2}$ |
|---|---|---|---|---|---|---|---|
| S4 | HPK | n-on-p | 200 | 39 | 600 | uniform | $4 \times 10^{15}$ |
| S5 | HPK | n-on-p | 200 | 39 | 450 | non-uniform | $\sim 1 \times 10^{15}$ |
| S6 | HPK | n-on-p | 200 | 39 | 450 | uniform | $8 \times 10^{15}$ |
| S8 | HPK | n-on-p | 200 | 35 | 450 | uniform | $8 \times 10^{15}$ |
| S9 | HPK | n-on-p | 200 | 35 | 600 | uniform | $8 \times 10^{15}$ |
| S11 | HPK | n-on-p | 200 | 39 | 450 | non-uniform | $8 \times 10^{15}$ |
| S12 | HPK | n-on-p | 200 | 39 | 600 | uniform | $4 \times 10^{15}$ |
| S15 | HPK | n-on-p | 200 | 35 | 450 | uniform | $4 \times 10^{15}$ |
| S17 | HPK | n-on-p | 200 | 39 | 450 | uniform | $8 \times 10^{15}$ |
| S20 | HPK | n-on-p | 200 | 35 | 450 | - | - |
| S21 | HPK | n-on-p | 200 | 35 | 450 | non-uniform | $\sim 1 \times 10^{15}$ |
| S22 | HPK | n-on-p | 200 | 35 | 450 | uniform | $8 \times 10^{15}$ |
| T2 | HPK | n-on-p | 200 | 35 | 450 | uniform | $4 \times 10^{15}$ |
| S23 | Micron | n-on-p | 200 | 36 | 450 | uniform | $8 \times 10^{15}$ |
| S24 | Micron | n-on-p | 200 | 36 | 450 | uniform | $8 \times 10^{15}$ |
| S25 | Micron | n-on-p | 200 | 36 | 450 | non-uniform | $8 \times 10^{15}$ |
| S26 | Micron | n-on-p | 200 | 36 | 450 | - | - |
| S27 | Micron | n-on-p | 200 | 36 | 450 | uniform | $8 \times 10^{15}$ |
| S29 | Micron | n-on-p | 200 | 36 | 450 | uniform | $8 \times 10^{15}$ |
| S31 | Micron | n-on-p | 200 | 35 | 250 | - | - |
| T15 | Micron | n-on-p | 200 | 36 | 450 | uniform | $8 \times 10^{15}$ |
| S30 | Micron | n-on-n | 150 | 36 | 450 | non-uniform | $8 \times 10^{15}$ |
| S33 | Micron | n-on-n | 150 | 36 | 250 | - | - |
| S34 | Micron | n-on-n | 150 | 36 | 250 | - | - |

Table 3.3: Table presents the specificatons of all protoypes presented in this thesis. If the sensor was not irradiated it is indicated by (-). Sensor names begining with “S” are “singles” and “”T” are “triples”.

# Chapter 4

# Characterisation and Testing

To determine which of the prototypes best suit the requirements of the upgrade, they were thoroughly tested. The tests were performed in a laboratory at CERN and at the SPS testbeams using the TimePix3 telescope. This chapter will discuss the two test set-ups and the different tests performed on the prototype sensors.

## 4.1 Laboratory

The ultimate test of the performance of the prototypes is undertaken at the SPS beamline. Before deployment in the testbeam, prototypes were first characterised in the lab. The goal was to determine a safe operational voltage by performing a Current-Voltage (IV) scan (Section 4.1.2), to equalize the TimePix3 ASICs to determine thresholds (Section 4.1.3), and to perform charge calibrations to convert ToT values into electrons (Section 4.1.4).

### 4.1.1 Set-up

To study the performance of the sensors in an environment similar to that of the VELO, all tests were performed inside a vacuum tank allowing the use of either dry air or vacuum conditions. The lab set up is shown Figure 4.1. The sensors were mounted on top of a peltier device, which in combination with a water/glycol chiller provided cooling

to a minimum temperature of -44 °C. Operating at low temperature prevents thermal runaway (see Section 2.3) and potential sparking that can break the sensor. The dry air or vacuum conditions stop condensation forming on a cooled sensor, and the vacuum specifically limits sparking at high voltages. The TimePix3 was controlled using the Speedy PIxel Detector Readout (SPIDR) system readout system [35] and a Keithley high voltage supply provided the bias voltage.

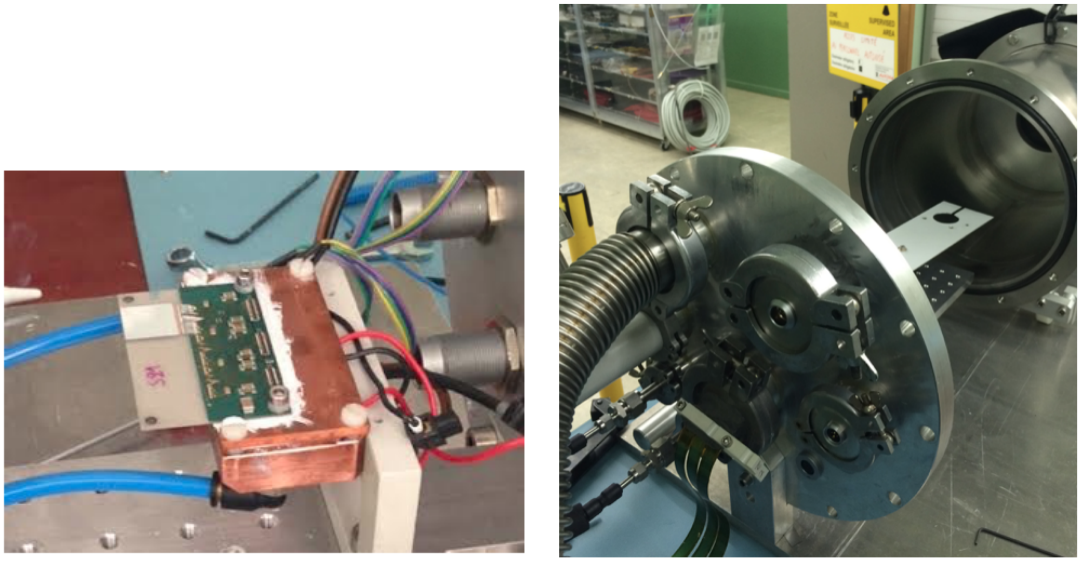

Figure 4.1: Photographs of the laboratory set-up: An example "single" sensor mounted on a peltier device (a) and the vacuum tank (b).

### 4.1.2 Current-Voltage (IV) Scans

Measuring the leakage currents using IV scans is a powerful tool when testing sensors [23]. Almost all possible problems that can occur in the production process can lead to deviations in the expected shape of an IV curve. Also, they are used to determine the depletion and safe operational voltages. The IV scan was taken in 1 V steps with a delay of 2 seconds between steps to allow the current to settle. The current was measured for voltage steps ranging from 0 to 1000 V, or stopped before breakdown. Figure 4.2 shows an example of an IV scan taken for a non-irradiated sensor, measured at a temperature of 15 °C in dry air. For low voltages the current increases until a point where the full width of the sensor is depleted. This point is visually seen at ~100 V and is referred to as the depletion voltage. Above the depletion, the current begins to

plateau. But at greater voltages the current starts to increase and electric breakdown begins. Initially the breakdown is only in certain regions with high electric fields within the sensor, but at very high voltages hard break down can occur, seen at ~850 V.

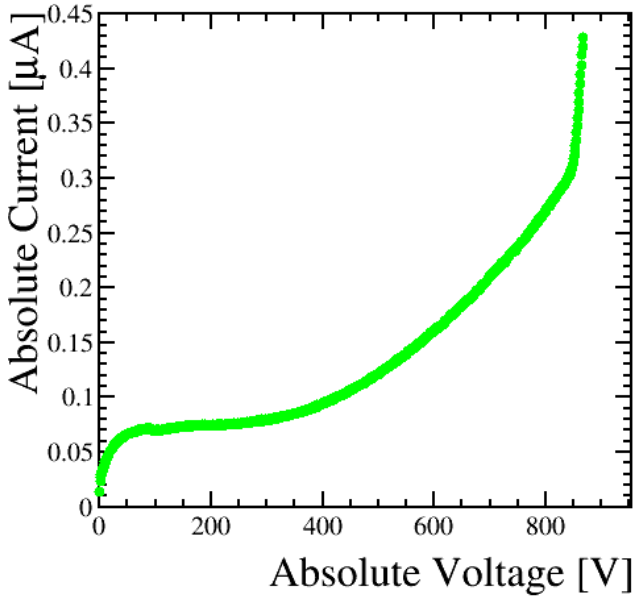


Figure 4.2: Example of an IV scan for a 200 µm thick HPK sensor.

### 4.1.3 Threshold Equalisation

Manufacturing imperfections in the TimePix3 ASIC electronics can lead to small variations in performance for the different input channels. Their responses may vary even though they share the same global threshold value. Each pixel can be tuned locally with a 4-bit trimDAC, where their threshold values are determined by an equalisation procedure [36–38]. The aim of this procedure is to determine a local pixel threshold such that all pixels have a uniform response to a set global threshold. The equalisation procedure begins by setting the local threshold to its lowest value. For each pixel, the global threshold DAC (THL) is scanned from a level of no counts (threshold above the chip noise) to a level where all the pixels count (threshold close to the noise level). This procedure is then repeated with the local threshold set to its highest value and the the THL is scanned again. Figure 4.3 shows the result of an equalisation scan. The two broad Gaussian distributions show the spread of the pixel responses during equalisation for the local threshold set at its minimum value (blue) and maximum value (red).

For each pixel, the local threshold is chosen as the THL value that gives a noise signal closest to the mid point between the two Gaussian mean peak values. The equalisation procedure is then repeated using the new local threshold. The pixel response is shown in Figure 4.3 as the narrow distribution (black). This procedure reduces the noise of the Timepix3 due to threshold dispersion. The Timepix3 ASIC has a noise level of about 60e$^-$ RMS and a typical threshold variation of around 30e$^-$ RMS. Generally the TimePix3 ASICs are operated at a threshold of 1000e$^-$ to ensure that the threshold is well above the noise [39].

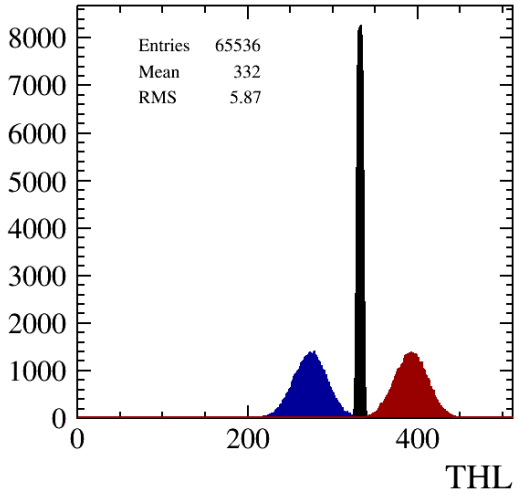


Figure 4.3: Results of an equalisation scan, the red distribution is the threshold dispersion measured at the lowest local threshold and the blue distribution is the threshold dispersion at the highest local threshold. The black distribution shows the threshold dispersion after equalisation.

### 4.1.4 Charge Calibration

The TimePix3 device measures the charge signals in units of ToT, as described in Section 3.2. To convert the ToT values to electrons, the ASIC is calibrated using the test pulse method. Pulses of known charge are injected into each of the pixels and the ToT is measured to obtain a calibration curve. Figure 4.4 is an example calibration curve for one pixel. An overall linear trend is seen for values greater than 2000e$^-$, below this a non-linear behaviour is observed. The data trend can be described by [40]

$$f(x) = p0 + p1 \cdot q - \frac{c}{(q - t)} \tag{4.1}$$

Where $p0$ and $p1$ represent the intercept and slope of the linear part of the distribution well above threshold, $c$ and $t$ parametrise the non-linear behaviour at low ToT, close to threshold. Due to variations in the pixel circuitry this procedure is done for each of the pixels allowing a charge calibration to be applied to each individual pixel.

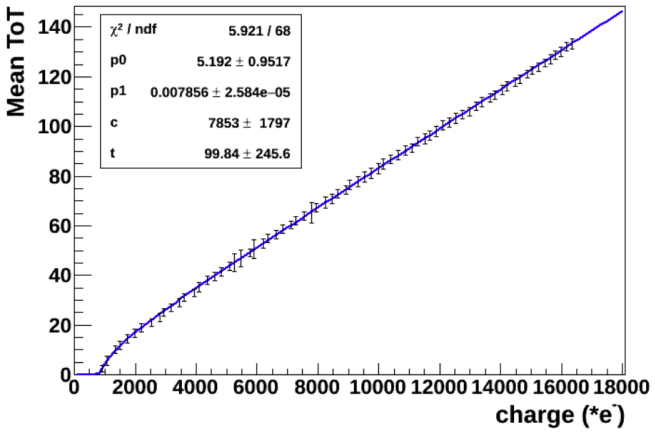


Figure 4.4: Example calibration curve for one pixel, taken from [38].

## 4.2 TimePix3 Telescope

When testing prototype sensors, the sensors are placed in charged particle beams and the response of the sensor to the incoming particles is studied. The hit positions and times of the incoming particles are reconstructed using a beam telescope. The TimePix3 telescope is a beam telescope that was specifically built for VELO Upgrade R&D [41]. An illustration of the telescope is shown in Figure 4.5. It has 8 planes of 300 µm thick p-on-n sensors bump bonded to the Timepix3 ASIC, divided equally between two arms. The planes are mounted at an angle of 9° in both $x$ and $y$ to improve position reconstruction. The positions of the telescope planes along the $z$-axis are adjustable but typically the distance between planes was 31 mm in each of the arms. There is a 200 mm gap between the two arms allowing for a Device Under Test (DUT) to be placed in the centre. The DUT is mounted on a copper block that provides cooling via a Peltier device and is housed in an air tight box circulating dry air. The DUT was installed on a motion stage allowing angular rotations and $x$ and $y$ translations. The row number of

the pixel matrix corresponds to the $y$ coordinate, and the column number of the pixel matrix is the $x$ coordinate.

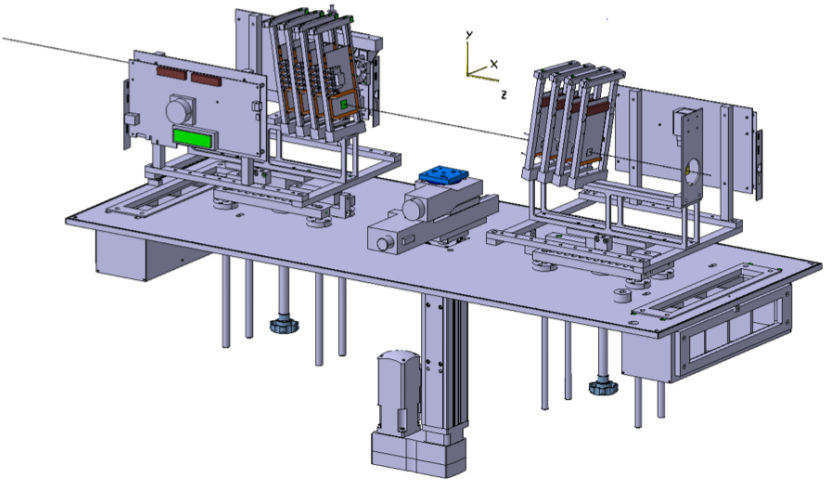


Figure 4.5: Illustration of the TimePix3 telescope consisting of 8 sensor planes divided between arms. A device under test can be installed in the centre.

### 4.2.1 Track Reconstuction

The telescope is used to reconstruct the hit position and time of the incoming particles. As a charged particle traverses each of the telescope planes, it deposits charge on one or more pixels creating a cluster in each of the telescope planes. Cluster formation and the method of reconstructing the hit position using the Centre of Gravity (COG) technique is further described in Section 6.1.1. A time stamp of the earliest pixel hit within a cluster is recorded and is used in the patten recognition to reconstruct a charged particle track. Two clusters in two adjacent planes which differ by less than 10 ns in their time stamps form a track seed. The closest cluster in the next plane, that is found within a window of 10 ns and spatial window of a cone with an opening angle of 0.01 radians is added to the track. This procedure is repeated for all planes, and tracks that have hits in all 8 planes of the telescope are fit with a linear regression, as shown in Figure 4.6. There are two types of track fits: biased and unbiased. A biased track fit is when all telescope planes (and DUT if applicable) are included in the track fit, whereas a for an unbiased track fit, the telescope plane under study is removed from the track reconstruction. For analysis performed on a DUT, the track fit is always unbiased and all telescope planes

are included in the fit. This is to limit any alignment issues (Section 4.2.2) and so that the plane under study does not bias the track fit.

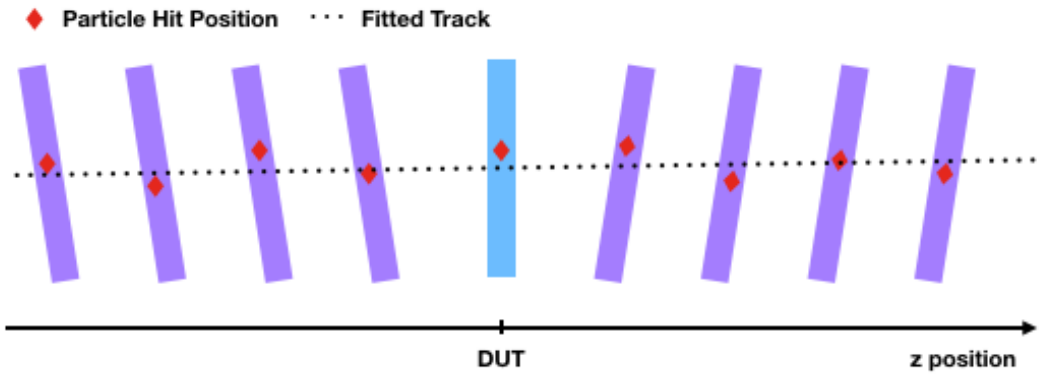


Figure 4.6: Sketch of a charged particle track through the telescope. The hit positions reconstructed using the deposited charge are shown in red markers and the fitted track shown by the dashed black line.

To determine the goodness of the track fit, the $\chi^2/n_{dof}$ is measured and shown in Figure 4.7. For the majority of tracks the $\chi^2/n_{dof}$ is less than 2, meaning that the track reconstruction algorithm is successful. Larger $\chi^2/n_{dof}$ can occur due to a variety of effects, including telescope plane misalignment or $\delta - rays$ degrading the hit position reconstruction.

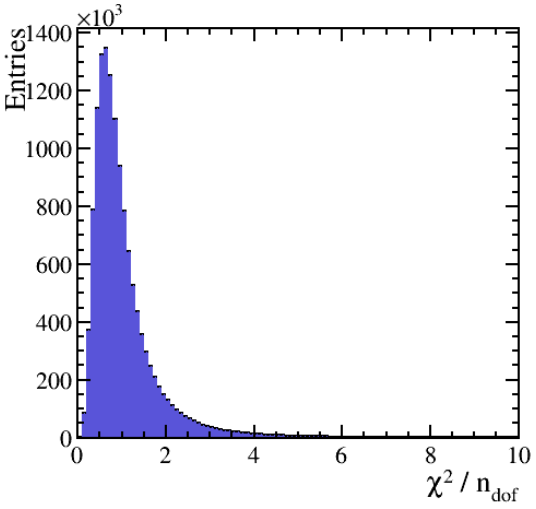


Figure 4.7: The $\chi^2/n_{dof}$ of tracks fits performed using the TimePix3 Telescope.

### 4.2.2 Alignment

A good alignment of the telescope is crucial for the subsequent analysis. The positions at which the planes are mounted in the telescope is estimated by eye with limited precision. Therefore track based alignment is required to determine their positions and rotations and correct for any misalignments. This is done using the Millipede algorithm [42], which uses the linear least squares method. It is an iterative process which aims to minimise the difference between the reconstructed sensor hit position and the track position, known as the residual difference. One way to check the success of the alignment procedure, is to plot the unbiased residuals. If the residual distribution is offset from zero, it suggests that the planes are offset in either the $x$, $y$ or $z$ direction. An example unbiased residual distribution in $y$, for one telescope plane is shown in Figure 4.8 (left). The residual distribution is centred around zero, meaning that any offsets have been corrected for. Figure 4.8 (right) shows the unbiased residual distributions in $y$ depending on the track position in $x$ ($x_{track}$). If these distributions are angled with respect to the horizontal axis, it suggests that there are misalignments in the rotation angles $\theta_x$, $\theta_y$ and $\theta_z$. For the example shown the variation is less than 0.2 µm across the beam spot and the residual width is stable. Both plots indicate that the alignment procedure was successful.

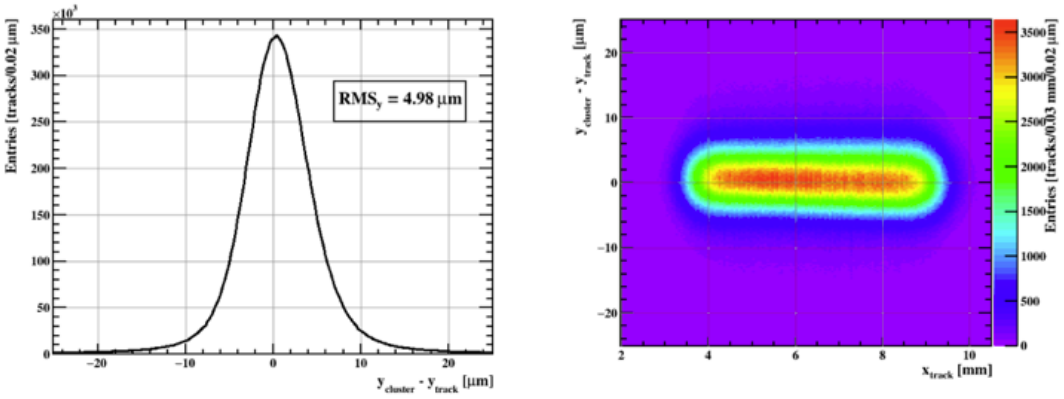


Figure 4.8: The unbiased residuals in $y$ for one of the telescope planes (left) and the unbiased residuals in $y$ as a function of the track positions in $x$ (right).

### 4.2.3 Multiple Scattering

The path of a charged particle traversing a medium is affected by many small angle scatters due to multiple Coulomb scattering with the medium nuclei [1], previously

discussed in Section 2.1. The slight deflections of particles as they travel through each of the telescope planes mean that the particle does not follow a straight line and this reduces the precision of the track hit position reconstruction. The multiple scattering angle expected for the telescope plane can be estimated using Equation 2.2. The SPS produces a particle beam of energy 180 GeV, consisting of both protons and pions. Solving Equation 2.2 for protons gives an angular width of $17.4{\times}10^{-5\circ}$ with $x/X_0$ for a telescope plane estimated to be 1.067%.

The scattering angles can also be measured using testbeam data. Using the cluster positions on each of the planes allows the measurement of scattering angles for planes 1, 2, 6 & 7. An illustration of a exaggerated track scattering on each of the telescope planes (in the front arm) is shown in Figure 4.9. The angle is estimated by solving the angle between two vectors with the relation given as an example for $\theta_2$:

$$\theta_2 = cos^{-1}\left(\frac{\vec{v_{12}} \cdot \vec{v_{23}}}{|\vec{v_{12}}| \cdot |\vec{v_{23}}|}\right) \tag{4.2}$$

where $\vec{v_{12}}$ is the vector of the track between plane 1 & 2 and $\vec{v_{23}}$ between plane 2 & 3.

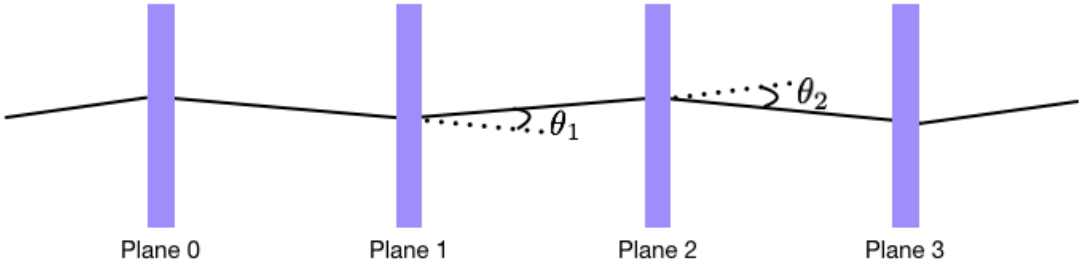


Figure 4.9: Illustration of the scattering occurring the front arm of the telescope.

The angular distributions for planes 2, 6 & 7 are shown in Figure 4.10. The distributions show a clear Gaussian-like shape centred around zero as expected. The distributions were fit with a Gaussian and the standard deviations are summarised in Table 4.1. The average angular width is $(24.8 \pm 0.9) \times 10^{-5\circ}$ which is slightly larger than the theoretical estimate of $17.4{\times}10^{-5\circ}$ calculated using Equation 2.2. This is because the distributions from data incorporate the error on the reconstructed hit positions and the pointing resolution of the telescope, both of which vary plane to plane, further described in Section 4.2.4. Overall, the multiple scattering angle is small, however, it is still expected

| Plane | Multiple Scattering Angle (°) |
|---|---|
| 2 | $23.1\times10^{-5} \pm 1.6\times10^{-5}$ |
| 6 | $26.9\times10^{-5} \pm 1.5\times10^{-5}$ |
| 7 | $24.3\times10^{-5} \pm 1.7\times10^{-5}$ |

Table 4.1: Table of the multiple scattering angular widths for plane 2, 6 & 8, taken as the standard deviation of a Gaussian fit to the distributions. The average angular width is $24.8\times10^{-5}$°.

to degrade the tracking performance of the telescope, which will be discussed in the next section.

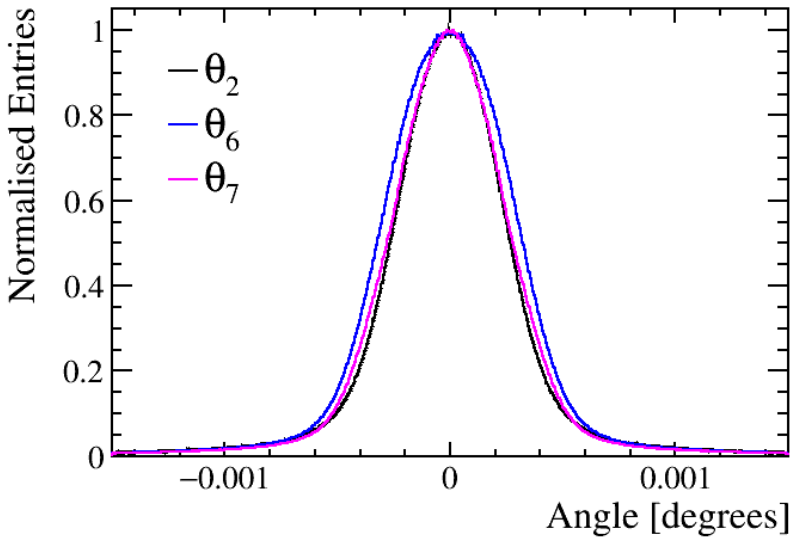


Figure 4.10: Measured scattering angle distributions for planes 2, 6 & 7.

### 4.2.4 Telescope Pointing Resolution

The performance of a telescope is quantified by its pointing resolution, which defines the precision with which the hit position of a particle can be reconstructed. The pointing resolution is not constant along the track and is dependent on the intrinsic resolution of the telescope sensors, the number of sensors in the telescope, their thickness and their relative z positions. A pointing resolution in the order of a few microns will allow for intra-pixel studies.

The pointing resolution of the telescope was estimated using a Monte Carlo simulation. In the simulation random tracks are generated with a randomly assigned scatter angle

for each telescope plane, dependent on the fractional radiation length $x/X_0$ (see Section 4.2.3). Additionally, each plane is assigned a single hit resolution. This single hit resolution for each plane can vary due to differences in ASIC thresholds and incident angle relative to the beam. Initial estimates were found by subtracting in quadrature the unbiased resolution (from data) and a reasonable first guess of the pointing resolution at the $z$ position of that plane. A track is then fit to the generated hits in the telescope and the biased resolution calculated. The pointing resolution is then measured by calculating the reconstructed position $x_{track}(z)$. The same is then done for $x_{hit}(z)$ where the reconstructed hit positions between two neighbouring planes is determined using the vector between the two hits. The residual differences ($x_{hit}(z)$-$x_{track}(z)$) can then be calculated for the different $z$ steps for multiple tracks allowing the pointing resolution to be extracted at different $z$ positions along the telescope. The simulation was then iterated several times with updated estimates of the hit errors to try and optimise the correspondence between the biased resolution measured in data to that of the simulation. The single hit resolutions of the planes were found to be between 3.7 - 4.2 μm for $x$ and 2.8 - 3.4 μm for $y$.

Figure 4.11 shows a plot of the pointing resolution in the $x$ direction. The biased resolution from data is compared to simulation. The pointing resolution varies depending on the $z$ position. The best achievable pointing resolution is found at the centre of the telescope and $\sigma_x = 1.69 \pm 0.16$ μm in $x$ and $\sigma_y = 1.55 \pm 0.16$ μm in $y$. The pointing resolution as a function of the $y$-coordinate can be found in Appendix A.

As previously discussed the single hit resolution for each plane can vary due to differences in ASIC thresholds and incident angle relative to the beam. For sensors that have a lower threshold relative to the rest, the charge collection can be larger and spread over more pixels increasing the cluster size. For sensors placed at slightly larger angles than the rest, the charged particle generates more charge and traverse more pixels, again increasing the cluster size. The cluster size contributes to the precision with which the sensor hit position can be reconstructed, therefore leading to variations in the spatial resolution (further discussed in Section 6.1.1). Figure 4.12 shows the biased resolutions from data, compared to the mean cluster size in column, for each of the telescope

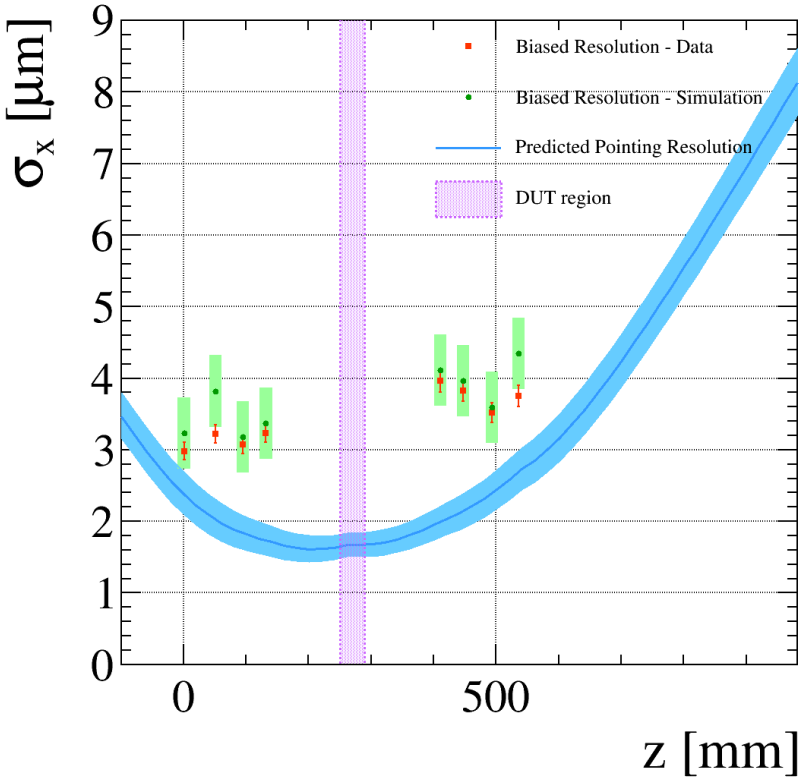


Figure 4.11: The pointing resolution in $x$ as a function of $z$. The best achievable pointing resolution is found at the centre of the telescope and $\sigma_x = 1.69 \pm 0.16$ µm in $x$

planes. Generally, a larger cluster size results in a better spatial resolution, which is the behaviour observed in Figure 4.12. The equivalent plot for the $y$-coordinate can be found in Appendix A.

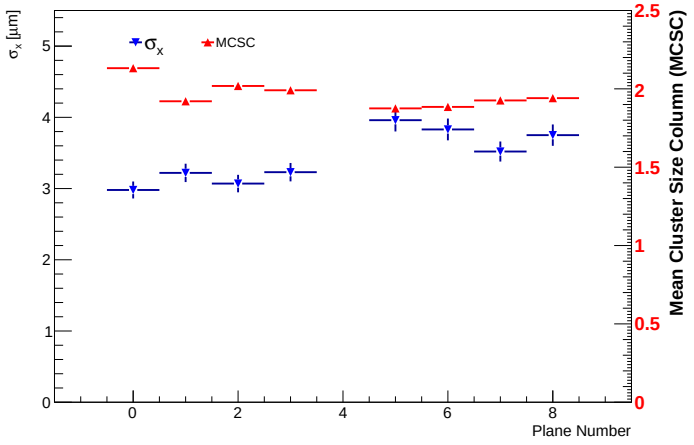


Figure 4.12: The biased resolution in $x$ (blue) and the mean cluster size in columns (MCSC) (red) for each of the telescope planes.

# Chapter 5

# Performance of the Prototypes

In this chapter, a summary of the results from different testbeam analyses will be presented. The studies include the high voltage (HV) tolerance after irradiation, the charge collection and efficiency both before and after irradiation, and an evaluation of the different guard ring designs. These studies were performed to determine which of the prototypes best fit the requirements of the VELO, previously outlined in Section 3.3. A colour scheme is introduced to identify the different prototypes types which follows, unless otherwise stated: green for HPK sensors, blue for Micron n-on-p sensors and purple for Micron n-on-n sensors.

## 5.1 Charge Collection

The generation of charge from a traversing charged particle though a silicon sensor was previously described in Section 2.2. A charged particle will generate ~ 80 electron-hole pairs per micron of traversed silicon. Therefore, for a fully depleted 200 μm thick sensor, the magnitude of generated charge is expected to be approximately ~ 16000$e^-$ and ~ 12000$e^-$ for a 150 μm thick sensor. At voltages below depletion, the full sensor bulk is not depleted therefore not all of the charge generated is collected.

The method of measuring the depletion voltage for a sensor was previously described in Section 2.2. This measurement was repeated for all sensors tested at testbeam to

determine the depletion voltages for the sensor prototypes. Figure 5.1 shows the most probable value's (MPV) of the charge distributions as a function of the bias voltage for a collection of different prototypes pre-irradiation. For the HPK (green) and the Micron n-on-p (blue) sensors, there is a steep rise in the charge collection with increasing bias voltage until depletion is reached. After depletion, the charge signal plateaus. Both collect a maximum charge signal of $\sim 16000e^-$, which compares well with the estimate. Even though the HPK and Micron n-on-p sensors are the same thickness (200 µm), they have different depletion voltages, ~ 120 V for HPK and ~ 40 V for Micron n-on-p. The differences are because of the different doping concentrations, as described in Equation 2.16. The Micron n-on-n sensors (purple) collect a maximum charge signal of $\lesssim 12000e^-$, due to their smaller thickness of 150 µm which also compares well with the estimate. It is difficult the extract the exact depletion voltage for the Micron n-on-n sensors as there was no data collected below 40 V and the steep increase in charge collection before depletion is not visible. Therefore the expected depletion voltage of a Micron n-on-n sensor is assumed to be $\lesssim 40$ V.

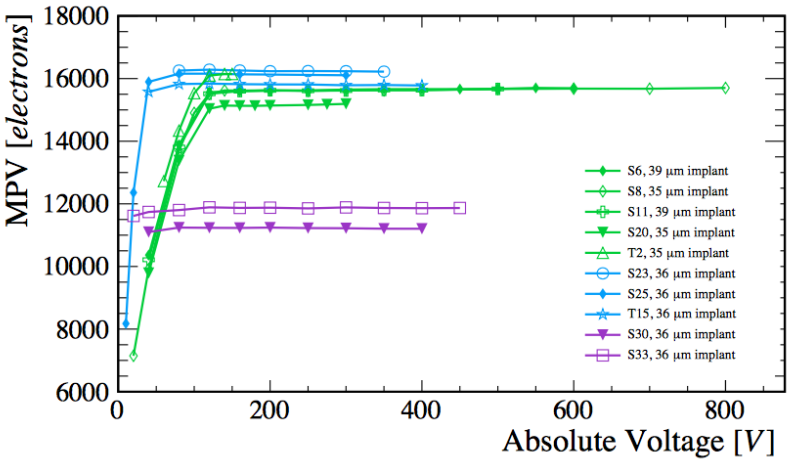


Figure 5.1: Most probable collected charge as a function of bias voltage for un-irradiated sensors, taken from [28].

For irradiated sensors, the radiation induced trapping centres act like p-type doping which in turn alters the depletion voltage, as described in Section 2.3. For the prototype sensors presented, the voltage required to deplete the sensors is expected to increase. Figure 5.2 shows the MPV as a function of bias for a collection of irradiated prototypes. They were exposed to a fluence of $8\times10^{15}$ $1\text{MeVn}_{\text{eq}}\text{cm}^{-2}$, which is the full expected dose

at the tip of the sensor at the end of the VELO's lifetime. The radiation profile was uniform across the sensor. The collected charge increases with bias as expected, however the collected charge does not plateau, meaning that the sensor does not reach full depletion at bias voltages below 1000 V. All prototype types follow the same trend, suggesting that there is no dependence on the thickness and type post irradiation. In terms of the performance requirements, all sensors collect the minimum charge requirement of 6000$e^-$ post-irradiation at a bias voltage ~ 800 V, which is well below the maximum 1000 V allowed.

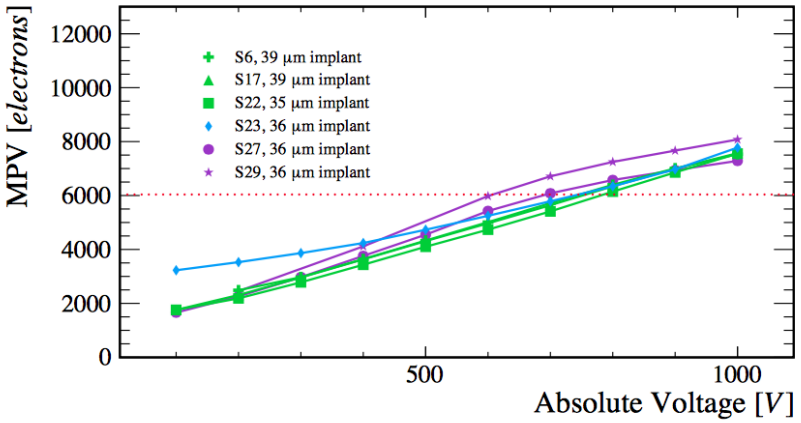


Figure 5.2: Most probable collected charge as a function of bias voltage for post-irradiated sensors, taken from [28].

## 5.2 High Voltage Tolerance

As discussed above, irradiated sensors need to operate at very high bias voltages to collect sufficient charge. It was shown in Section 2.2.4, that the leakage current increases linearly with fluence, meaning higher currents are expected for irradiated sensors. The sensors must be able to tolerate high voltages without breakdown, where the VELO upgrade specifically requires that they do not breakdown before 1000 V.

The IV scans were repeated once the sensors had been sent to the irradiation facilities using the method previously described in Section 4.1.2. The vacuum was used to avoid sparking and the sensors were cooled down to -30 °C to avoid thermal runaway. Figure 5.3 shows the IV curves measured for five sensors which were non-uniformly irradiated, two at $4\times10^{15}$ 1MeVn$_{eq}$cm$^{-2}$ and three at the maximum $8\times10^{15}$ 1MeVn$_{eq}$cm$^{-2}$.

All sensors reach 1000 V without breakdown. The current is higher for the sensors that were exposed to the maximum fluence, as expected. The trends are distinctively different from the un-irradiated distribution, see Figure 4.2. There is no "turning" point in the trend to signify that the sensor bulk is depleted. This suggests that after the maximum fluence, the full thickness of the sensor cannot be depleted at a bias voltage of 1000 V.

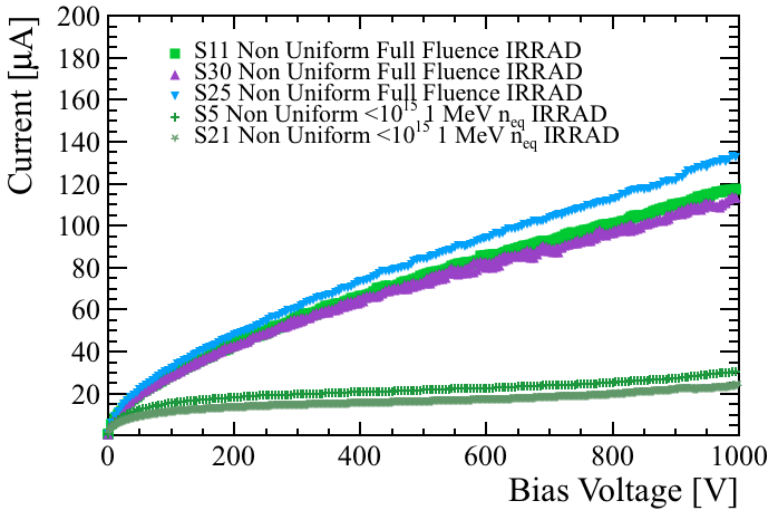


Figure 5.3: Example IV curves from 3 sensors exposed to the full fluence and 2 at half fluence, taken from [43]. All measurements were taken when the sensors were cooled down to a temperature of -30 °C. Green for HPK sensors, blue for Micron n-on-p sensors and purple for Micron n-on-n sensors.

## 5.3 Charge Collection Efficiency

Efficient track reconstruction is vital for a good physics performance. Sometimes, a charged particle traverses a sensor and the deposited charge does not exceed the threshold, meaning that the particle is not detected. This reduces the efficiency, where the cluster finding efficiency is defined as the probability of finding a cluster given the presence of a track. Clusters are introduced in Section 6.1.1 and refer to a single pixel or group of neighbouring pixels that measure a charge signal above threshold. The method of extracting the efficiency is further described in [28].

For pre-irradiated sensors, the sensor is expected to be very efficient. The most probable amount of collected charge for a fully depleted sensor is about ~16000$e^-$ or ~12000$e^-$

for either thickness. The threshold to detect a hit is 1000$e^-$. Hence, nearly all hits are detected. Figure 5.4 shows the efficiency as a function of bias for a range of prototype sensors pre-irradiation. There is a steep increase in the efficiency at very low bias which then plateaus at an efficiency of ~ 99.9%. The voltage at which the peak efficiency is reached is almost identical for all prototypes and is much less than the full depletion voltages. This is because only a small fraction of the charge needs to be collected in order to reach the 1000$e^-$ threshold.

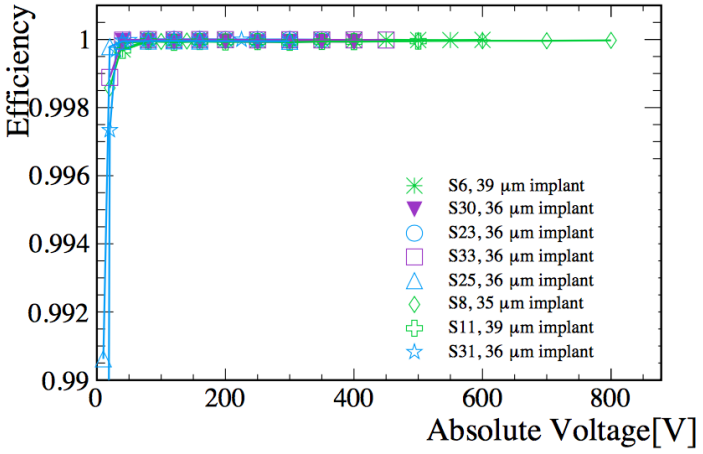


Figure 5.4: The cluster finding efficiency as a function of bias for pre-irradiated prototypes sensors, taken from [28].

It was shown in Figure 5.2, that none of the irradiated prototypes reach full depletion below 1000 V and therefore the charge collected is much less. This can cause inefficiencies in the sensors because there is a higher probability that the collected charge does not reach threshold. Figure 5.5 shows the efficiency as a function of the bias voltage for a range of prototype sensors post-irradiation. The sensors were uniformly irradiated to the full fluence of $8 \times 10^{15}$ $1\text{MeVn}_{\text{eq}}\text{cm}^{-2}$. The efficiency at low voltages is much less than that measured pre-irradiation. However, as the voltage tends towards 1000 V the efficiency tends towards 99%. This is because at higher bias voltages, the charge collection is larger and the drift velocities are higher reducing the probability of the charge trapping.

The efficiency can also be studied at the intra-pixel level to determine where in the pixel the greatest inefficiencies occur. Figure 5.6 compares the intra-pixel efficiencies of two uniformly irradiated 200 µm thick HPK sensors with different implant sizes operated at

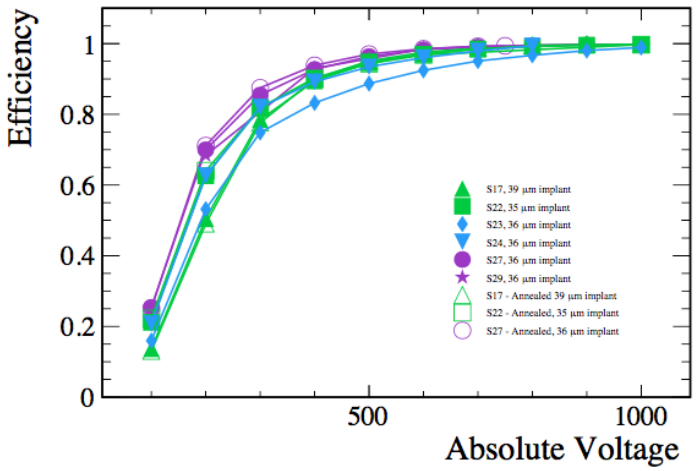


Figure 5.5: The cluster finding efficiency as a function of bias for post-irradiated prototypes sensors, taken from [28]. The sensors were irradiated to the maximum dose of $8 \times 10^{15}$ 1MeVn$_{eq}$cm$^{-2}$.

300 V: S22 an implant size of 35 µm (a) and S17 an implant size of 39 µm (b). In both sensors the highest efficiency can be seen in the centre of the pixel with the efficiency decreasing towards the corners. However, a higher efficiency is seen over a greater area for the sensor with the larger implant. The inefficiencies at the very corners of a pixel are due to the charge division. When a particle hits at the corner of a pixel, the charge can be shared between up to four neighbouring pixels, meaning that the magnitude of charge measured in each pixel implant is small. This decreases the probability that the charge measured exceeds the ASIC threshold. Therefore, to achieve a higher efficiency in HPK sensors at lower bias voltages, a larger implant is more effective. Charge sharing, its dependence on the intra-pixel hit location and pixel implant size is further described in Section 6.1.1.

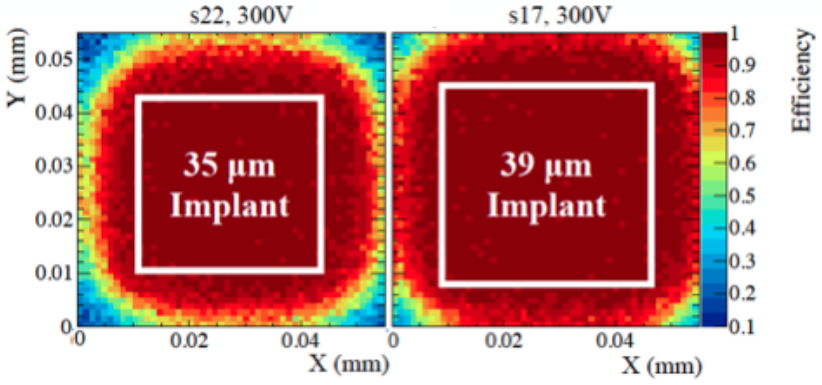


Figure 5.6: The intra-pixel cluster finding efficiency for two 200 µm thick HPK sensors operated at 300 V post-irradiation, taken from [28]. The two sensors differ in implant size: S22 an implant size of 35 µm (a) and S17 an implant size of 39 µm (b).

## 5.4 Guard Ring Design Comparisons

As discussed in Section 1.4, the highest occupancy in a sensor installed in the VELO, will be at the very edge closest to the interaction region. At this edge, it is crucial that the guard rings work effectively. The role of the guard rings is to establish a smooth voltage drop between the biased pixel matrix and the cut edge of the sensor, previously described in Section 2.2.3. Furthermore, the guard rings also have to collect any charge deposited by charged particles traversing through the guard ring area. If the guard rings are not successful at collecting the full charge, the charge can be collected by the first row/column of active pixels in the sensor, increasing the occupancy. A sketch of a charged particle traversing the guard rings is shown in Figure 5.7.

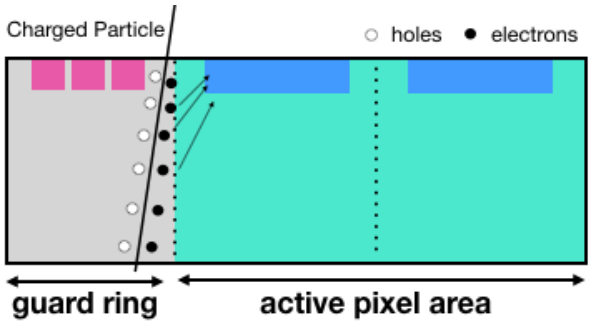


Figure 5.7: Illustration of the edge of a sensor, showing the guard rings and active pixels. A charged particle crosses the guard rings area. If the guard rings are not successful at collecting the generated charge carriers, they can be collected by the first row/column of active pixels.

The performance of the guard rings of pre-irradiated sensors was studied by measuring the total charge in a cluster as a function of the intra-pixel track position in $x$, shown in Figures 5.8. The analysis includes tracks that cross the guard ring area and not only the active area of the sensor. The physical edge of the sensor is illustrated with a vertical green line and the first few columns of active pixels are illustrated by dashed black lines. Therefore the guard rings lie between the physical edge of the sensor and the first column of pixels for the n-on-p sensors. The n-on-n guard rings are implanted on the backplane of the sensor and cover less area around the periphery of the sensor and lie beneath the first two columns/rows of pixels, as described in Section 3.1. Figure 5.8 (a) shows the performance for a 200 µm thick Micron n-on-p sensor (S26) that has a guard ring size of 450 µm. Beyond the first column of pixels and into the guard ring area there are

significant charge deposits, the magnitude of which decrease with increasing distance from the first column in pixels. This suggests that the guard rings are not effectively collecting the charge from traversing particles and the charge is collected in the first column of pixels, increasing the occupancy. Figure 5.8 (b) shows the performance for a 150 μm thick Micron n-on-n sensor (S33) that has a guard ring size of 250 μm. In comparison to Figure 5.8 (a), there are minimal charge deposits measured in the guard ring area outside of the active pixel area. However, the measured charge in the first column of pixels is less than that of the neighbours. This therefore suggests that the guard rings that lie beneath the first column of pixels are collecting charge from charged particles traversing the active area of the sensor. Reduced charge collection, can lead to lower efficiencies and poorer spatial resolution. Figure 5.8 (c) shows the performance for a 200 μm thick HPK n-on-p sensor (S20) that has a guard ring size of 450 μm. The charge collection across the first four columns of pixels is constant and the charge collection stops beyond the pixel matrix.

The guard ring behaviours presented above are the same for all prototypes of the same type. For example, all Micron n-on-p sensors had ineffective guard rings, as do the Micron n-on-n. Therefore the HPK n-on-p sensors are the only guard ring design that perform as they should and successfully collected charge from charged particles traversing the guard rings region.

## 5.5 Summary

The charge collection and efficiency of the sensor prototypes was measured before and after irradiation. The 200 μm thick sensors yielded ~ 16000$e^-$ signals pre-irradiation when operated at the depletion voltage and above. The 150 μm sensors yielded less charge at $\lesssim$ 12000$e^-$ signals, as expected. Therefore, a thicker sensor is a more favourable design choice in terms of charge generation. The 200 μm Micron n-on-p sensor reaches full depletion at a lower voltage than that of the HPK sensors, due to the differences in doping concentrations. Post irradiation, all sensors are display most probable cluster signals of 6000$e^-$ or more at bias voltages ~ 800 V or greater. All prototypes presented

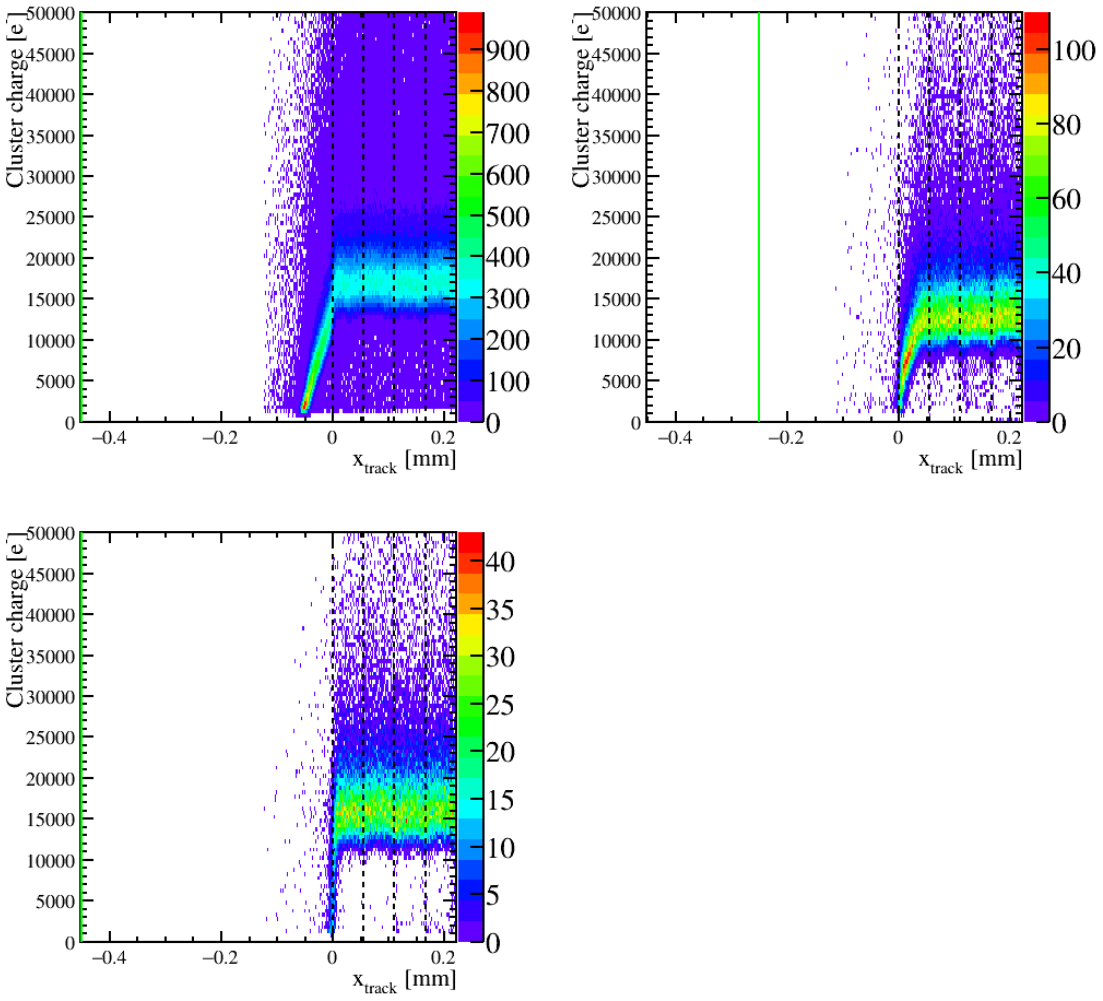


Figure 5.8: The measured charge in a cluster depending on their track position within a pixel, taken from [44]. (a) A 200 µm thick Micron n-on-p sensor (S26) with a guard ring size of 450 µm. (b) A 150 µm thick Micron n-on-n sensor (S33) that has a guard ring size of 250 µm. (c) A 200 µm thick HPK n-on-p sensor (S20) that has a guard ring size of 450 µm. The green vertical line illustrates the physical edge of the sensor and the dashed vertical line identify different columns of active pixels.

were shown to be able to tolerate 1000 V without breakdown. For all sensors an efficiency greater than 99% was measured both before and after irradiation. Higher bias voltages were required post irradiation to recover the efficiency. At lower bias, it was seen that pixels with smaller implants had more inefficient corners than that of pixels with larger implants. Therefore a larger implant is more favourable for optimising the efficiency in irradiated sensors.

The guard ring performance for pre-irradiated sensors was studied for three different prototype sensor types. Both Micron designs did not work as they should, with the

n-on-p design not effectively collecting the charge from the inactive area and the n-on-n design collecting charge from the active pixel matrix. Both of these would degrade the performance of the VELO, since the highest density of tracks pass through the very corner of the sensors, as shown Section 1.4. The HPK guard ring design performed as it should.

From the testbeam analysis presented, the Micron n-on-p design would provide the largest charge generation at the lowest bias voltage. However HPK provided prototypes with the largest implant option of 39 µm, resulting in more efficient corners post-irradiation at low voltages. The HPK sensor design also has a sufficient guard ring design, making HPK sensors the strongest candidate for the VELO upgrade. The only requirement outlined in Section 3.3, not discussed thus far is the spatial resolution. The spatial resolution is the main subject of this thesis and will be studied in the following chapters.

# Chapter 6

# Spatial Resolution Performance of the Prototypes Pre-Irradiation

Spatial resolution is the measure of accuracy to which the hit position of a particle is reconstructed. The resolution depends on many design choices, like the pixel pitch, thickness, the choice of read out (binary or analogue), operational parameters like the bias voltage and thresholds, and the reconstruction algorithm [23]. The spatial resolution is defined by the difference between the position predicted by the track, provided by the telescope (discussed in Section 4.2) and the hit position reconstructed using the sensor. This is known as the residual difference. The width of the residual difference is the spatial resolution. In this chapter, the spatial resolution of non-irradiated prototypes will be presented. Firstly, the method of measuring the spatial resolution is explained in detail in for a sensor placed perpendicular to the beam, operated at the depletion voltage. Then, the variation of the spatial resolutions with the bias voltage and the track angle is studied. For all studies, the binary and analogue spatial resolutions are compared.

## 6.1 Charge Sharing and Position Reconstruction

When designing a sensor for particle detection and reconstruction different factors need to be considered. As described in Section 2.2.2, a traversing charged particle will initiate a cloud of mobile charge carriers. These charge clouds are typically around $5-10$ µm wide. The movement of mobile charge carriers induces a signal on the read-out electrodes. The charge measured at these electrodes depends on the electric field configuration and the distance between all moving carriers and the electrodes. The latter is determined by the device thickness and the pixel pitch. If the pixels are large, the charge is collected by only a few electrodes. This typically leads to one electrode having a high signal and the neighbouring pixels having a very small signal. This high signal leads to a high efficiency, but the small signal on the neighbouring pixels will have a small Signal to Noise (S/N) ratio and thus limit the position resolution. If the pixel pitch is much larger than the width of the charge cloud, the charge will be collected by only one pixel for many tracks. For such hits, it is impossible to improve the hit position estimate from simply the centre of the pixel as there is no additional information. If the pixels are small, charge can be spread over many pixels which will all collect a small fraction of the charge. The lower signals lead to a smaller S/N but the information on the neighbouring pixels allows the improvement of the hit position estimate. Having a smaller pitch and hence higher granularity can help reduce the occupancies in high particle densities and improve pattern reconstruction. The sensor design for the VELO upgrade has a pixel pitch of 55 $\mu m^2$ and the prototypes have a range of different implants size from $35-39$ µm where the pixel pitch was limited by the area required for the readout ASIC. This section will discuss how charge is shared in the sensor and how pixel clusters are formed. From this, the method of reconstructing the hit position is described and the spatial resolution measured.

### 6.1.1 Pixel Clusters

Because of the finite width of the charge clouds generated in the sensor, it is the hit position within a pixel and incident angle of a particle that determines if charge is shared

between pixels. Figure 6.1 is an illustration depicting four different scenarios for particle tracks travelling close to the perpendicular. If a track crosses a sensor near the centre of a pixel, charge is not likely to be shared with another pixel creating a cluster of size 1. If the track crosses at the edge between two pixels then it is likely that charge is shared between two pixels creating a cluster of size 2 and if a track hits near the corner of a pixel the charge can be shared between 3 or 4 pixels.

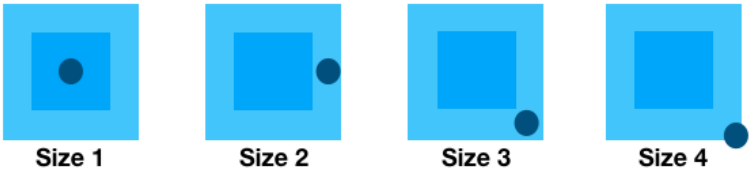


Figure 6.1: Illustration showing different incident hit positions that determine the size of the pixel cluster, for perpendicular tracks.

These scenarios can be observed in real data. A sensor was placed perpendicular to the beam and operated at 40 V. Figures 6.2 show the track hit locations for clusters of size 1, 2, 3 & 4, extracted from the telescope data. For size 1 clusters the majority of the tracks pass through the centre of the pixel. For size 2 clusters the tracks hit close to the edges of the pixels, with size 3 and 4 hits close to the corners.

These plots will have slightly different shapes depending on the size of the pixel implant and bias voltage. For example, a larger implant is expected to have a greater area of one pixel clusters in comparison to an implant of a smaller size. This is proven in Figure 6.3, where the projection of $x_{track}$ along the $x$-axis of the size 1 distribution (Figure 6.2 (a)) is plotted for two sensors which differ in implant size. This shows that there is less charge sharing between pixels if the implant is larger. This suggests that a smaller implant is more attractive when designing a pixel detector for position reconstruction. However, a larger implant reduces the probability that charge is lost and improves efficiency as shown in Section 5.3. The distribution variations depending on the bias voltage are presented in Section 6.3.

The charge sharing only improves position reconstruction if the signal on the neighbouring pixels has sufficient S/N. Furthermore, for the TimePix3 to register the charge in a pixel, the signal needs to exceed the minimum threshold set. If the charge shared does not reach threshold, the cluster remains size 1. If the signal does reach threshold, and

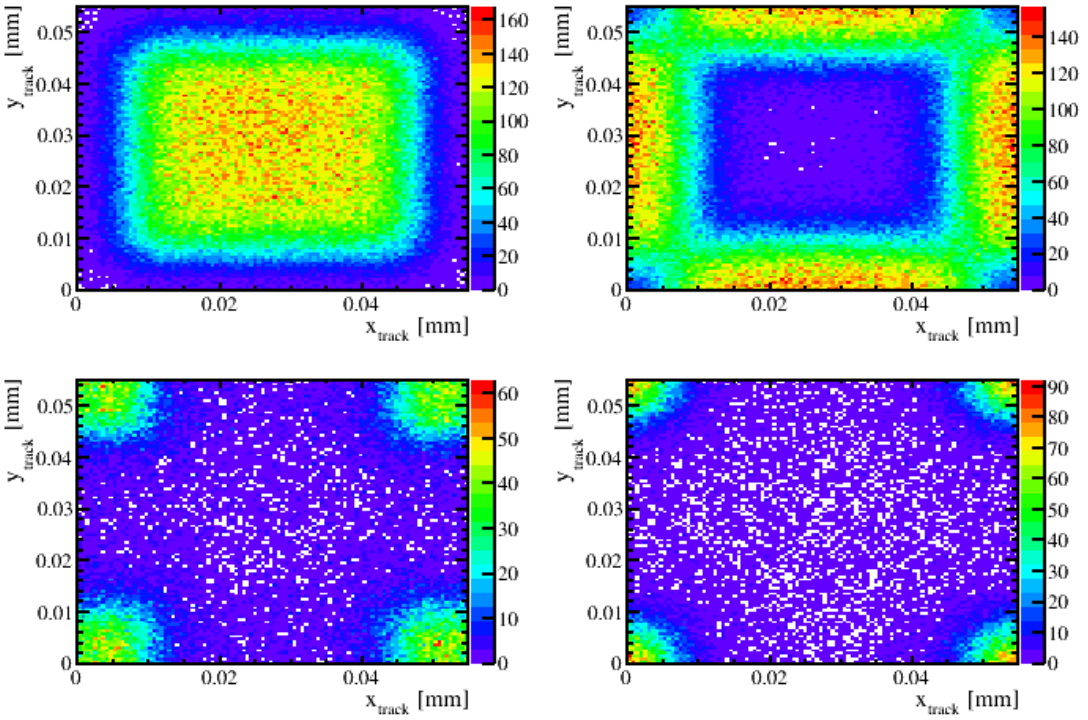


Figure 6.2: The intra-pixel track positions depending on cluster size. (a) size 1, (b) size 2, (c) size 3 and (d) size 4 for sensor S25.

the charge signal is small and close to the threshold value, this leads to a poor S/N ratio and is influenced by non linear effects (further discussed in Section 6.2.1). Figure 6.4 shows examples of different cluster shapes and sizes taken from data. The pixel with the largest ToT value is referred to as the seed pixel. For two pixel clusters, the charge on both pixels depends on the hit position of the track. This is demonstrated in Figures 6.5 (a) & (b), where the ToT value in the seed pixel (a) and the ToT value in the neighbouring pixel (b) for size 2 clusters are plotted depending on the track position $x_{track}$ within a pixel. For the seed pixel, the ToT is larger for tracks hitting closer to the centre of the pixel and the ToT decreases for tracks closer to the edge of the pixel as the charge division becomes more equal. In the neighbouring pixel, the opposite effect happens, the ToT values decrease for tracks that hit closer to the centre of the seed pixel.

For a particle hitting the corner of a pixel, sharing charge with four pixels, it is likely that an equal and smaller magnitude of signal is measured by each of the pixels, as seen in the example Figure 6.4. This is expected for a hit on the very corner of a pixel because the distance between the neighbouring implants is the same. But if the hit is

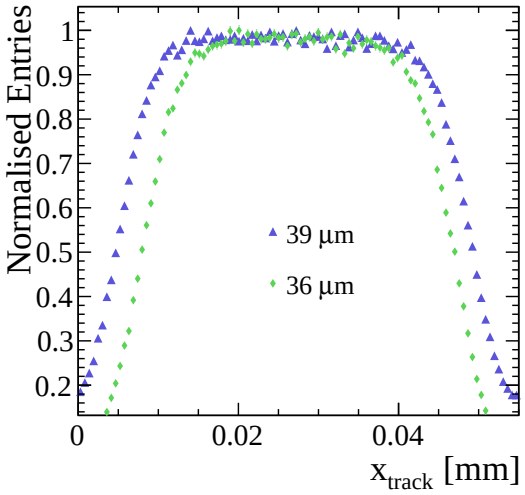


Figure 6.3: The comparison of the area at which one pixel clusters occur within a pixel for two different implant sizes. Sensor S25 has an implant size of 36 µm and was operated at 40 V and sensor S11 has an implant size of 39 µm and was operated at 120 V. The operational voltages chosen are the expected depletion voltages.

slightly offset from the corner of the pixel, the charge on the fourth pixel may not reach threshold leading to a cluster of size 3. The variations in charge division depending on cluster size is further studied, by plotting the ToT distributions measured by each of the pixels in a cluster, shown in Figure 6.6 (a) for size 3 and Figure 6.6 (b) for size 4. For size 3 clusters, the ToT values measured in the seed cluster are much larger than those measured in the 2 neighbouring pixels. For the size 4 clusters, the difference in ToT values measured in the seed pixel and the neighbouring pixels is much smaller, showing that the charge division is more equal for size 4 cluster. Also, the magnitude of ToT values in the size 4 seed pixel is smaller than that of the seed pixel in size 3 clusters as shown in Figure 6.6 (c).

As discussed above, the amount of charge sharing between pixels and hence the cluster size is largely dependent on the incident position of the track. For perpendicular tracks, due to the size of the implant and the width of the charge cloud, the majority of pixel clusters are size 1. This is shown in Figure 6.7. There are around half as many size 2 cluster and many less size 3 and 4 clusters. The formation of clusters greater than size 4 is very rare. It is also important to note that, the majority of clusters that are size 3 and 4 will have a pixel width of 2 in each direction. For example, it is very unlikely that a cluster of size 3 will be three pixels wide. The majority of the time they are “L”

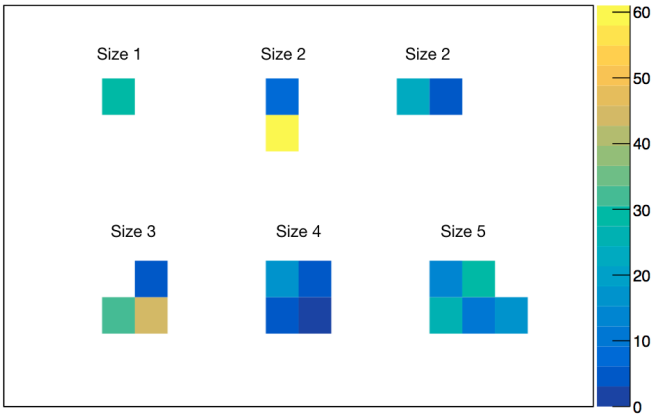


Figure 6.4: Example of different cluster shapes and sizes taken from data. The colours represent the ToT amplitudes measured in each of the pixels, where the scale is shown in the z axis

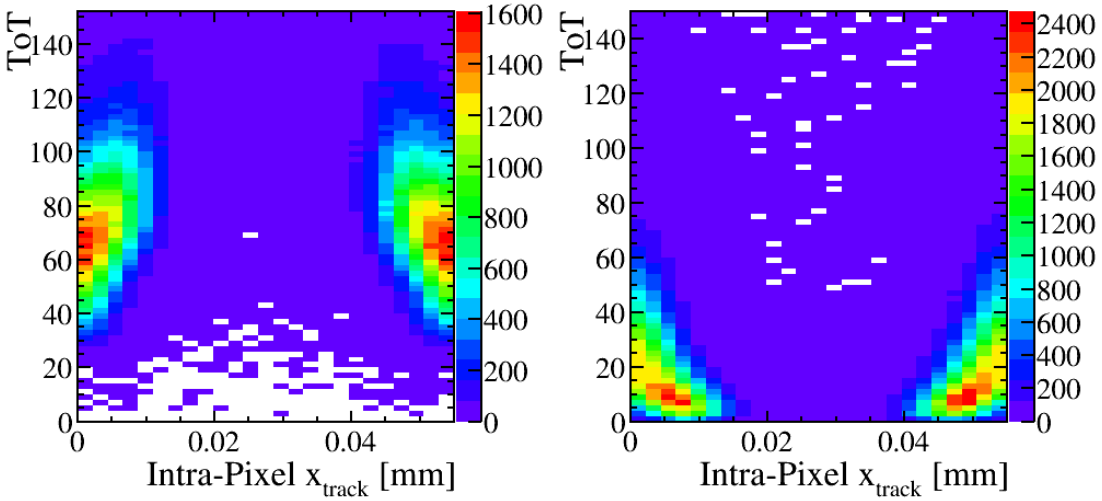


Figure 6.5: The ToT values measured in the seed pixel (a) and the ToT values measured in the neighbour (b) for a two pixel cluster plotted as a function of the intra-pixel track position $x_{track}$ (within the seed pixel) for sensor S25.

shaped as shown in Figure 6.4.

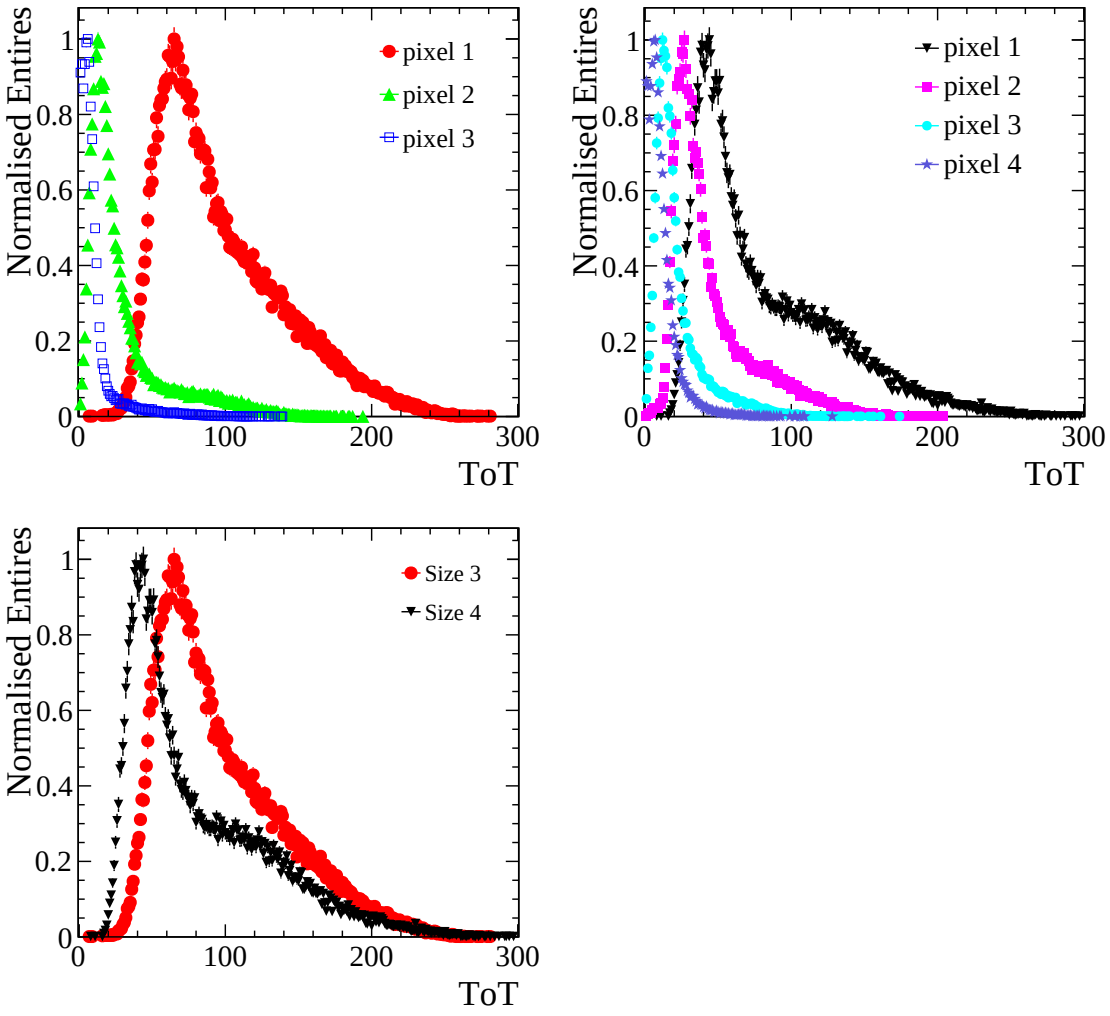


Figure 6.6: The ToT distributions measured in each pixel in a cluster for sensor S25. The seed pixel (pixel 1) for size 3 clusters (a) measures higher ToT values in comparison to the two neighbouring pixels. For size 4 clusters (b), the measured ToT in each pixel is smaller in magnitude but more equal. The ToT distributions of the seed pixels in size 3 and size 4 clusters are compared (c), where higher ToT values are measured in the size 3 clusters, as expected.

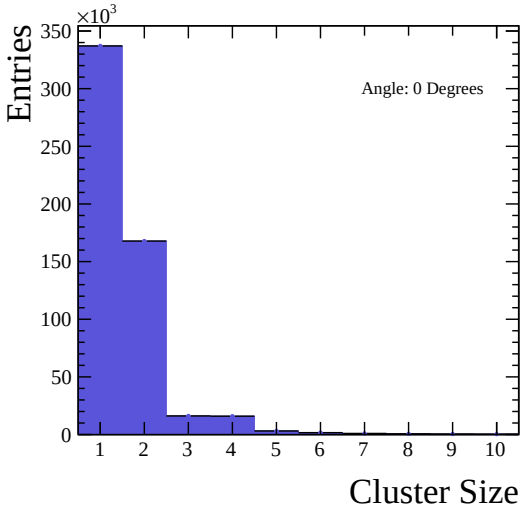


Figure 6.7: The cluster size distribution for perpendicular tracks for sensor S25. The majority of clusters are size 1 and the creation of clusters greater than size 4 is very rare.

### 6.1.2 Hit Position Reconstruction

Using the pixel clusters, the hit position of a particle is reconstructed. If the cluster is size 1, the hit position is taken as the centre of the pixel. If the cluster size is greater than 1, the hit position is derived using two different algorithms depending on the readout type. For sensors with an analogue readout, the most commonly used reconstruction algorithm is the Centre of Gravity (CoG) technique. The reconstructed hit position $x$ is weighted in terms of the charge fraction in every pixel associated to the cluster, given by:

$$x = \frac{\sum_{cluster} S_i \cdot x_i}{\sum_{cluster} S_i} \tag{6.1}$$

where $x_i$ is the position of the $i^{th}$ pixel in the cluster and $S_i$ is the signal measured in each of the pixels. The CoG algorithm assumes that the interpolation of the position between the pixels is linear with the charge distribution. However this is not exactly true, and will be discussed in the Section 6.2.1.

For a binary readout system, it is only known that a signal crossed threshold and hence the signal amplitude is not known. Therefore Equation 6.1 simplifies to:

$$x_{binary} = \frac{1}{N} \sum x_i, \tag{6.2}$$

where $N$ is the number of pixels and $x_i$ is the centre of the $i^{th}$ pixel.

## 6.2 Introduction to Spatial Resolution Measurements

### 6.2.1 Analogue Spatial Resolution

Knowing both the reconstructed hit position of the sensor and the predicted track position from the telescope, the residual difference $x - x_{track}$ is calculated. Figure 6.8 shows the residual distribution for the $x$ coordinate for S25 placed perpendicular to the beam and operated at 40 V. To obtain the spatial resolution, the width of the distribution needs to be extracted. As there is no theoretical expectation for the residual distribution,

it was chosen to fit the distribution with a Gaussian and take the standard deviation $\sigma$ as the spatial resolution, even though the shapes of the distributions are not necessarily Gaussian in nature [45]. The $\sigma$ given by the Gaussian fit for S25 is $11.96 \pm 0.05$ µm. However it is important to note that $\sigma$ incorporates not only the intrinsic resolution of the sensor $\sigma_{intrinsic}$ but also the telescope pointing resolution $\sigma_{telescope}$:

$$\sigma^2 = \sigma^2_{intrinsic} + \sigma^2_{telescope} \tag{6.3}$$

The pointing resolution of the telescope was studied in Section 4.2.4, and was measured as $\sigma_{telescope} = 1.69 \pm 0.16$ µm in the $x$ direction. Therefore the intrinsic resolution of S25 in the $x$ direction is $\sigma_{intrinsic} = \sigma_x = 11.85 \pm 0.17$ µm.

As mentioned above, the residual distribution is clearly not Gaussian in shape; it has a distinctive double peak structure. As a comparison, the residual distribution is shown using calibrated data (red) and using un-calibrated data (black) in Figure 6.9. The calibration procedure was previously introduced in Section 4.1.4. The double peak feature is still prominent in the calibrated residual distribution. The RMS for the calibrated distribution is 13.31 µm and the RMS for the un-calibrated residual is 13.92 µm. From the Gaussian fits, $\sigma_{calibrated} = 11.82 \pm 0.06$ µm and $\sigma_{un-calibrated} = 11.96 \pm 0.05$ µm. Generally there is a small improvement in the spatial resolution when using calibrated data, however since the change is small, by default the charge calibration is not used.

To understand this double peak feature, the residual distribution was split depending on the cluster size. Figures 6.10 (a), (b), (c) & (d) show the residual distributions for cluster sizes 1, 2, 3, & 4 respectively. For size 1, the reconstructed hit position is automatically assumed to be the centre of the pixel. This results in a distribution that has a top hat shape convoluted with a Gaussian, shown in Figure 6.10. Assuming the sensor is hit by a uniform density of particles, the box distribution is defined by the implant, which is where the majority tracks that create one pixels cluster occur. The smooth falling edges of the Gaussian are due charge diffusion and the telescope resolution. In the case of diffusion, if a particle is incident on an area outside of the implant, charge is shared with the neighbouring pixel, however if this charge does not reach threshold the cluster

remains size 1 and the residual difference between the track and the centre of the pixel is larger. The size 2 (b) & size 3 (c) distributions are both similar is shape and have the distinctive double peak structure seen in the full distribution (Figure 6.8). This feature is because of non-linear charge sharing between pixels. It will become clear below, that non-linear charge sharing influences pixels that have ToT values that are small. Since the signals measured by each pixel in a size 4 cluster are small, the non-linear charge effects cancel, meaning the double peak feature is not present in the distribution (d).

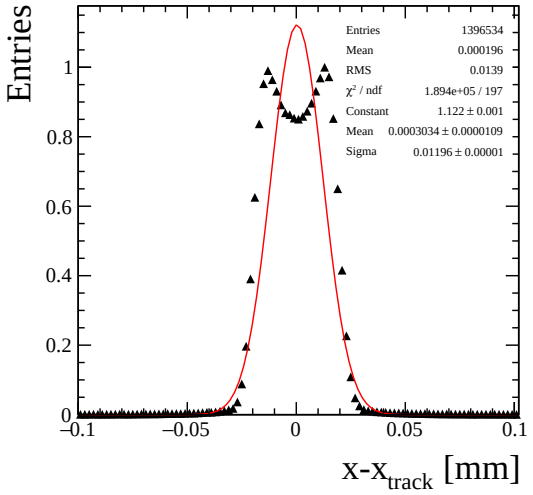


Figure 6.8: Example residual distribution for a sensor (S25) with analogue readout positioned at zero degrees relative to the beam.

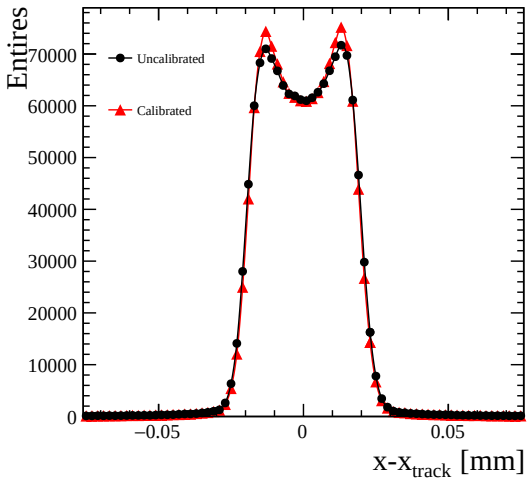


Figure 6.9: Comparison of the residual distribution using calibrated (red) and uncalibrated data (black) for sensor S25 positioned at zero degrees relative to the beam.

To understand non-linear charge sharing and the contributions to the two peak structure, the residual distributions were studied at the intra-pixel level. The tracks positions were

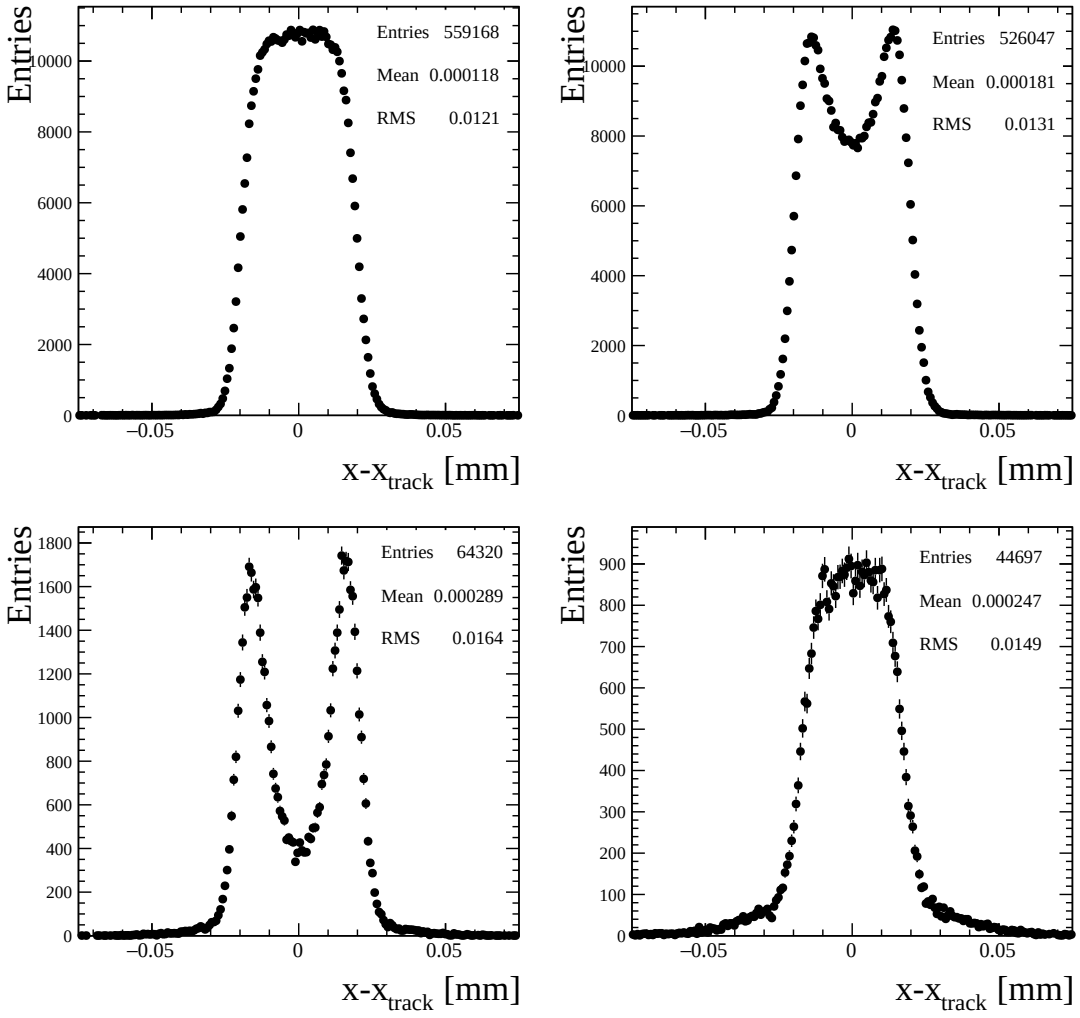


Figure 6.10: The residual distribution in $x$ depending on the cluster size for sensor S25: size 1 (a), size 2 (b), size 3 (c) and size 4 (d).

superimposed within the area of one pixel and the pixel was split into a $5 \times 5$ grid as illustrated in Figure 6.11. The example sensor studied (S25) has an implant size of 36 µm, meaning that the implant impinges a distance of 1.5 µm into the periphery bins. The residual differences were plotted depending on the track position and cluster size. The size 1 distribution is not influenced by non-linear charge sharing and the fraction of clusters that are size 3 and 4 is small for perpendicular tracks, therefore the grid plots for these cluster sizes can be found in the Appendix B. The intra-pixel grid plot for size 2 clusters is shown in Figure 6.12. The entries in the top and bottom row, specifically bins 5,10,15 & 9,14,19 are from size 2 clusters that have a pixel width of 2 in the $y$-direction (size 1 in $x$), hence the box like shape of the distributions in these bins. For clusters with a pixel width of 2 in the $x$-direction, the events of interest are in the very left and very

right of the grid, in bins 1,2,3 & 21,22,23. The distributions are asymmetric in shape, with a peak off centre. To further understand the behaviour of these distribution, the ratio of the ToT amplitudes in each of the pixels was measured. For size 2 clusters in the $x$-direction, the lowest ToT amplitude, $\mathrm{ToT}_{neighbour}$ was divided by the highest, $\mathrm{ToT}_{seed}$:

$$ToT_{ratio} = \frac{ToT_{neighbour}}{ToT_{seed}} \tag{6.4}$$

If the two amplitudes are similar in height the ratio will be close to 1 and if they are very asymmetric the ratio will be closer to 0. As an example, the $ToT_{ratio}$s measured in bin 2 are compared with the residual distribution of the same bin, is shown in Figure 6.13. There is a high proportion of entries that have a low $ToT_{ratio}$ and large residual difference. These clusters give rise to the peaks of the residual distribution. As the ratios tend towards 1, the residual difference decreases and tends towards zero. As a comparison, the $ToT_{ratio}$ was measured for all clusters size 2 in $x$ and compared with the residual distribution, shown in Figure 6.13 (b). The low $ToT_{ratio}$s lie beneath the double peak feature, symmetric around zero. The occurrence of equal charge sharing is small, therefore there are less statistics in this region leading to the dip in the residual distribution around zero.

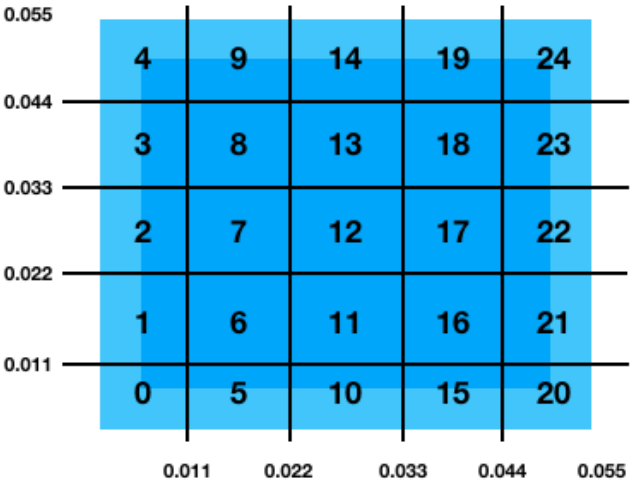


Figure 6.11: Illustration of the division of a single pixel into a $5 \times 5$ grid.

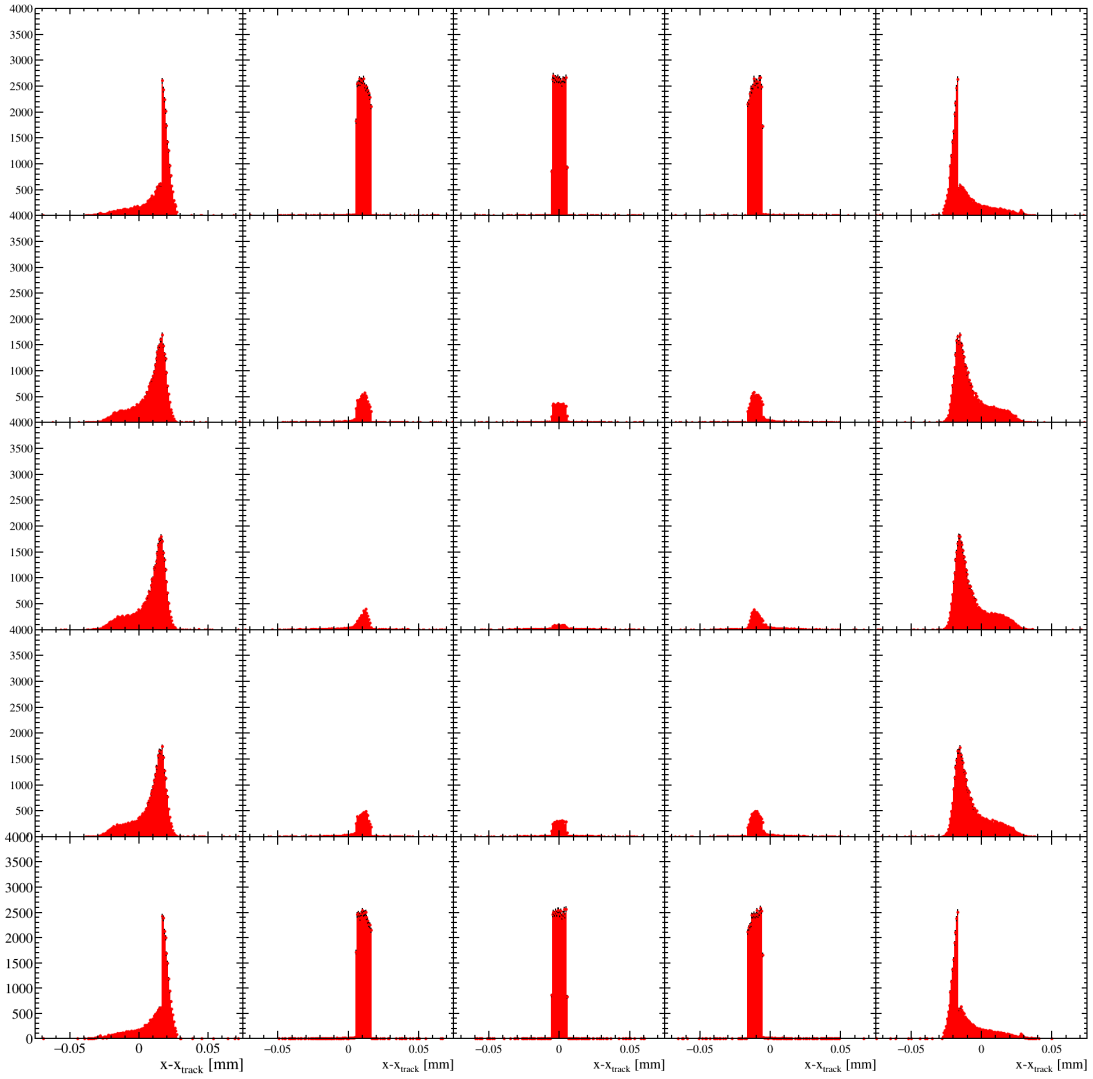


Figure 6.12: The analogue size 2 residual distributions depending on which bin the intra-pixel track position is assigned to, as illustrated in Figure 6.11 (S25).

The correlation of the hit positions and track positions is not linear across the pixel area. Figure 6.14 shows the correlation of the $x_{track}$ position as a function of the hit position $x$ for size 2 clusters in the $x$-direction, interpolated within the area of one pixel for the prototype sensor, S25 perpendicular to the beam. For particles that traverse close to the centre of a pixel, most of the charge is deposited in one pixel and only a small amount in the neighbouring pixel. Due to non-linear charge sharing the hit position is reconstructed disproportionately away from the track intercept and closer to the centre of the pixel. Therefore the non-linear charge sharing is position dependent and affects smaller charge signals more than larger signals. For tracks that traverse at the edge between the two pixels, the charge sharing is more equal and the two signals

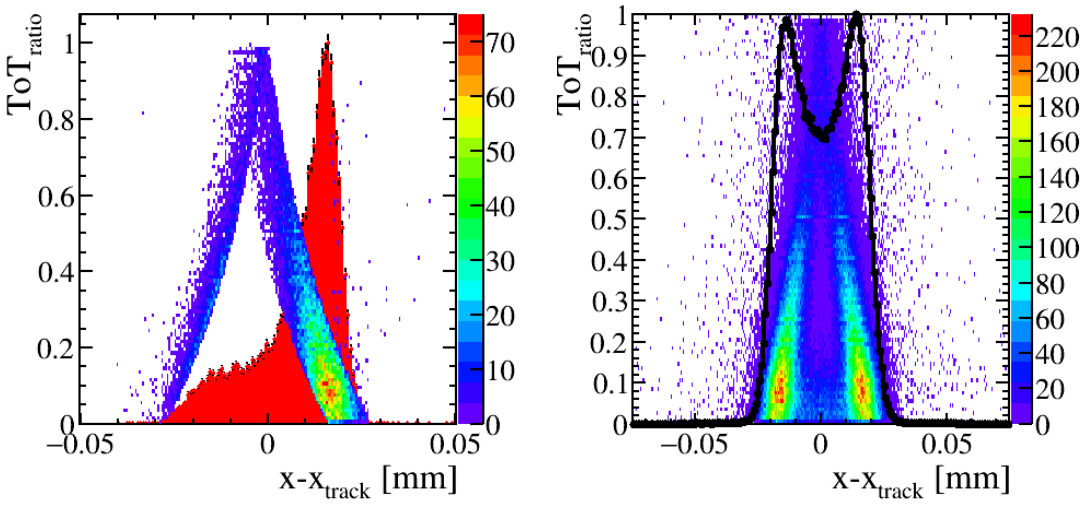


Figure 6.13: The $ToT_{ratio}$s plotted as function of the residual difference for bin 2 (a) for sensor S25. Underlain is the residual distribution for bin 2. As a comparison the same plot is shown for the full intra-pixel matrix (b).

are more likely to be much larger than the threshold resulting in a good hit position reconstruction. Therefore, it is more likely that clusters with very asymmetric charge values will have an poorly reconstructed hit position.

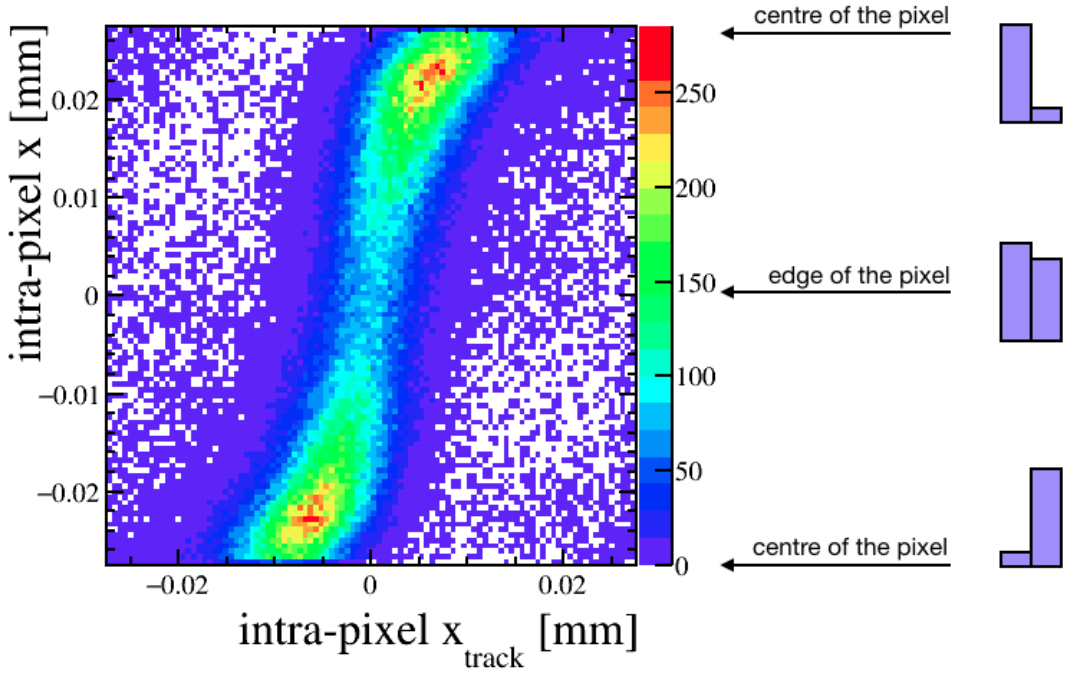


Figure 6.14: The correlation of the intra-pixel track position $x_{track}$ and the intra-pixel reconstructed hit position $x$ for perpendicular tracks for sensor S25. The plot has been arranged such that particles traversing close to the edge of the pixel in the centre, as illustrated by the arrows.

### 6.2.2 Non-Linear Corrections

The non-linear feature can be corrected for using Figure 6.14. By fitting Gaussian distributions to the intra-pixel track position distributions for fixed reconstructed intra-pixel hit positions, a position calibration curve was obtained. Figures 6.15 (a), (b) & (c) are example intra-pixel track position distributions for three different fixed intra-pixel hit positions (bins), fitted with a Gaussian. The centre of each bin for the hit positions was then plotted as a function of the mean from the Gaussian fits, creating the calibration curve shown in Figure 6.16. The calibration curve was fitted with a $5^{th}$ order polynomial and a new corrected hit position $x'$ was obtained using:

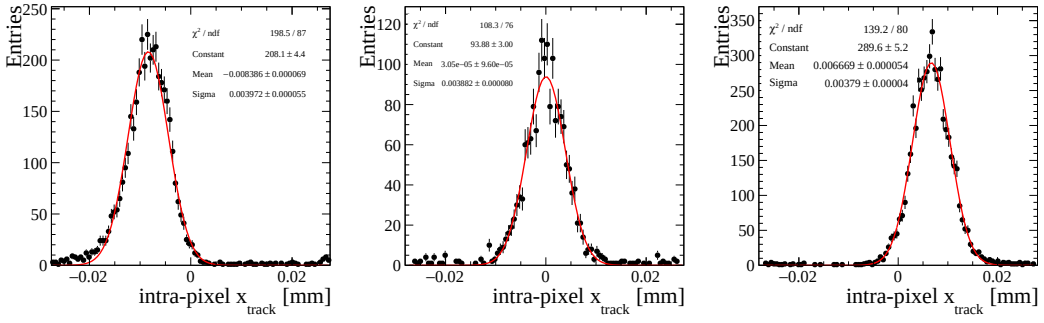


Figure 6.15: The intra-pixel track position distributions for three different fixed intra-pixel hit positions fitted with a Gaussian (S25).

$$x' = \sum_{i=0}^{5} a_i x^i \tag{6.5}$$

where $a_i$ are constants from the fit and $x$ is the original reconstructed hit position. The residual difference is then recalculated using the new hit position $x'$ and the track position. Figure 6.16 shows the corrected residual (red) and the uncorrected residual (black) for size 2 clusters in the $x$-direction. There is a clear improvement in the residual distribution using the correction. The $\sigma$ for the uncorrected distribution is 12.90 ± 0.11 µm and 3.81 ± 0.06 µm for the corrected distribution. The same method can be used to correct for size 3 and 4 clusters. The correlation of the intra-pixel $x_{track}$ positions plotted as a function of the intra-pixel hit positions $x$ for cluster sizes 3 and 4 are shown in Figures 6.17 (a) & (b) respectively. The tracks that are most likely to create size 3 clusters, hit close to the corner of the pixel, but closer to the centre of the pixel than tracks creating size 4 clusters, as shown in Figure 6.2. This means that they are effected

by the non-linear charge sharing due to their asymmetric charge division between the pixels in the cluster, therefore the entries in the size 3 distribution are at the corner of the plot. For the size 4 distribution, the charge division is more symmetric, meaning the non-linear effects are minimal and the entries are more linear. Therefore to create a calibration curve that can correct for these clusters, the two distributions need to be combined, as shown in Figure 6.17 (c). The calibration curve was then fit, using the method described above and is shown in Figure 6.17 (d).

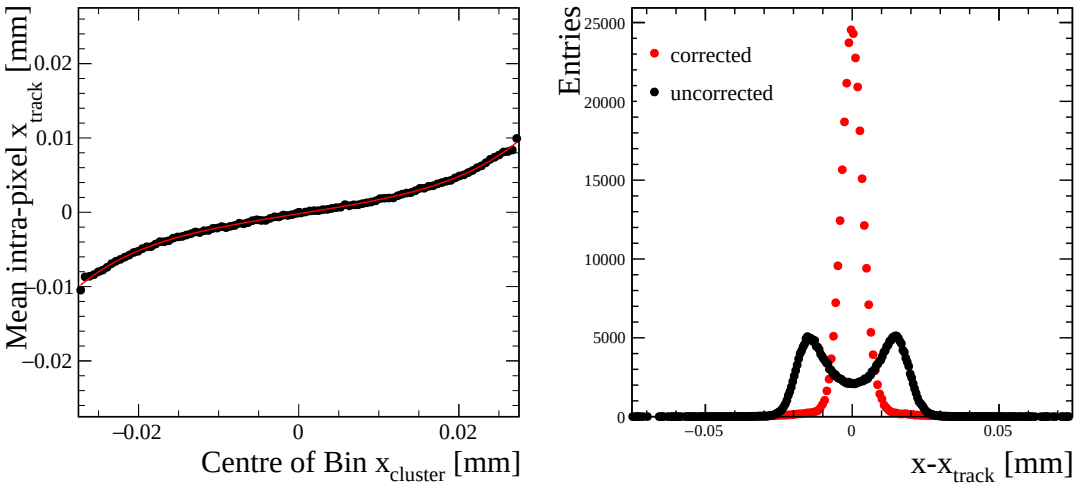


Figure 6.16: The fit calibration curve (a). A comparison of the uncorrected (black) and corrected (red) residual distributions for size 2 clusters in $x$ (b) for sensor S25.

Figure 6.18 (a) is a comparison of the uncorrected and corrected residual for size 3 and size 4 clusters combined. When fit with a Gaussian, the uncorrected $\sigma$ is $14.16 \pm 0.17$ µm and the corrected $\sigma$ is $4.55 \pm 0.16$ µm. This is the same magnitude of improvement seen for the size 2 distribution. To measure the overall improvement, the corrected residual distributions for size 2, 3 and 4 are combined with the size 1 distribution shown in Figure 6.18 (b) (red). For comparison, the equivalent uncorrected residual is shown (black). The results of Gaussian fits to the two residual distributions gives an uncorrected $\sigma$ of $11.69 \pm 0.06$ µm and a corrected $\sigma$ of $10.14 \pm 0.06$ µm. Because of the higher number of the size 1 clusters for perpendicular tracks, the width of the corrected residual is dominated by the "top hat" distribution. The size 1 distribution is limited by the size of the pixel implant therefore no further corrections can be made.

Overall, the correction only made a small improvement to the spatial resolution. The

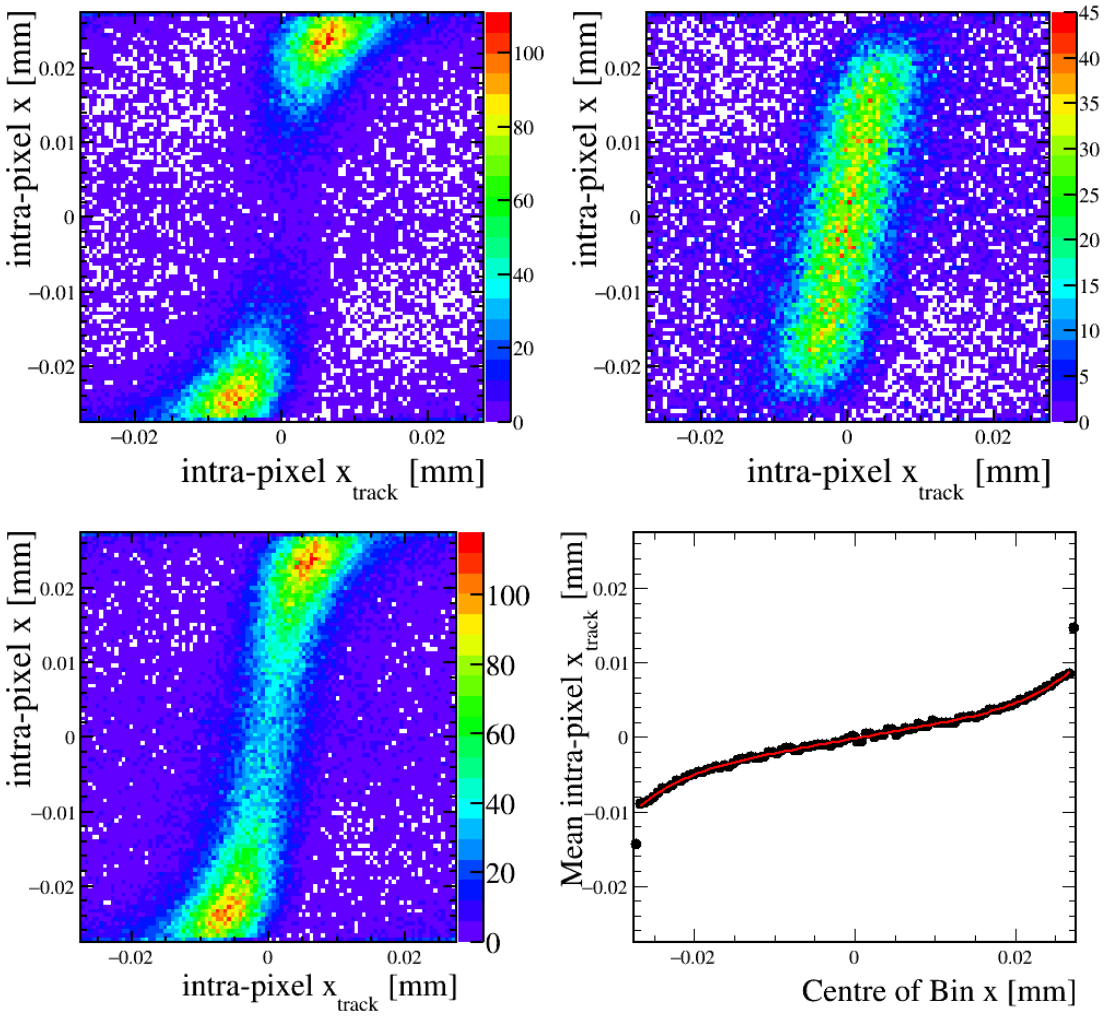


Figure 6.17: The correlation of the intra-pixel track position $x_{track}$ as a function of the intra-pixel reconstructed hit position $x$ for perpendicular tracks for size 3 (a) and size 4 (b) for sensor S25. The two distributions combined (c) to obtain a calibration curve (d).

correction relies on calibration curves obtained from the correlations of the intra-pixel tracks positions and the intra-pixel hit positions, which have previously only been shown for perpendicular tracks. These distributions vary depending on the angle of the track and the bias voltage, requiring new calibrations curves, presented in Section 6.6. Furthermore, tracks traversing at an angle generate more charge spread over more pixels. This reduces the non-linear charge sharing effects and thus improves of the spatial resolution without the need for a correction, see Section 6.4.2. This concludes that this correction is not practical given that only a small improvement is seen for perpendicular tracks.

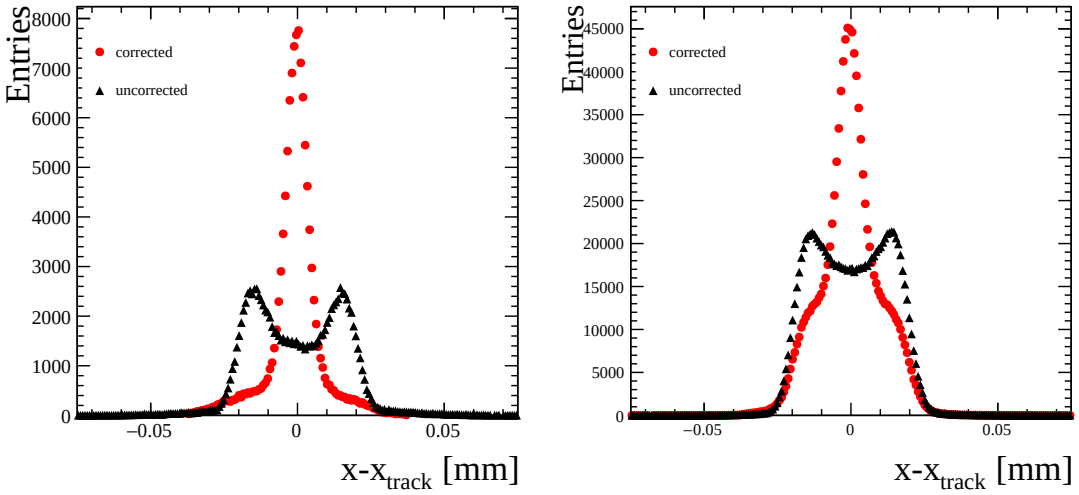


Figure 6.18: A comparison of the corrected and uncorrected size 3 and size 4 combined residual distributions (a) and a comparison of the corrected and uncorrected residual distributions for cluster sizes 1 through 4 (b) for sensor S25.

### 6.2.3 Binary Spatial Resolution

The TimePix3 device is used for prototype testing as it is an excellent general purpose ASIC, providing ToT information which is useful for performance studies on the silicon sensors, specifically those that require charge information. However, the VeloPix ASIC developed for the upgrade has a binary readout. To determine the expected VeloPix performance in the terms of the spatial resolution, the TimePix3 can mimic binary readout using only the pixel coordinates of the pixels above threshold. The reconstructed binary hit position is calculated using Equation 6.2.

For a binary detector, the spatial resolution can be calculated analytically [23]. Assuming that there is zero charge sharing between pixels the binary spatial resolution is given by:

$$\sigma^2_{binary} = \frac{\int_{-p/2}^{p/2}(x_r - x_m)^2 D(x_r)dx_r}{\int_{-p/2}^{p/2} D(x_r)dx_r} \tag{6.6}$$

where $p$ is the pixel pitch and $D(x_r)$ is the density distribution of the particles incident on the sensor. Setting the centre of the pixel to 0, $x_m = 0$ and assuming that the beam is homogeneous over a pixel, $D(x_r) = 1$, the equation simplifies to:

$$\sigma^2_{binary} = \frac{\int_{-p/2}^{p/2}(x_r)^2 dx_r}{\int_{-p/2}^{p/2} 1 dx_r} = \frac{p^2}{12} \quad thus \quad \sigma_{binary} = \frac{p}{\sqrt{12}} \tag{6.7}$$

A VELO upgrade sensor has a pixel pitch of 55 µm giving a theoretical estimation of $\sigma_{binary}$ = 15.9 µm. In reality, charge is shared between pixels. For perpendicular tracks it was shown that charge sharing was highly dependent on the hit position within a pixel, see Figures 6.2. It was also shown that tracks creating size 1 clusters mostly hit within the area of the implant. Therefore a more accurate estimation of the binary spatial resolution can be calculated by replacing the pixel pitch in Equation 6.7 with the implant size. For example, for a sensor with an implant size of 36 µm, the predicted binary spatial resolution would be 10.4 µm for size 1 clusters.

The binary position reconstruction is limited to the centre of the pixel for size 1 clusters and the very edge between two pixels for size 2, 3 and 4 clusters (for perpendicular tracks only). Therefore the binary spatial resolution is expected to be worse than the analogue resolution due to the lack of charge information used to reconstruct the analogue hit position. The binary residual distribution in $x$ for all cluster sizes is shown in Figure 6.19 for sensor S25. There is a distinct difference in the shape of the binary residual distribution in comparison to the analogue distribution shown in Figure 6.8. The double peak feature in the analogue distribution is not present in the binary distribution because non-linear charge sharing does not effect the binary position reconstruction due to the ToT information not being used. A Gaussian fit gives a resolution of $\sigma_{binary,x}$ = 10.94 ± 0.06 µm, subtracting the telescope pointing resolution gives an intrinsic sensor resolution of 10.79 ± 0.17 µm. Sensor S25 has an implant size of 36 µm and the previous estimation of the binary resolution for an implant of this size was 10.4 µm, which compares well with the resolution extracted from data. The reason that the a larger resolution is seen in data is because of the diffusion. For particles traversing close to the edge of the implant, the charge can diffuse to the neighbouring pixel. If the charge on the neighbour does not reach threshold then the cluster remains size 1. This means that the area with which size 1 clusters occurs in a pixel is slightly larger than the implant size for perpendicular tracks.

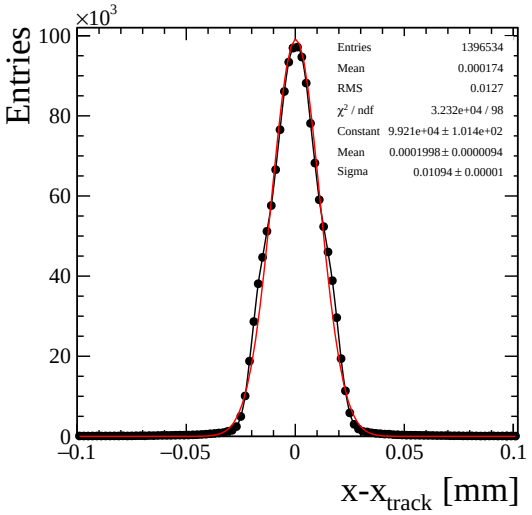


Figure 6.19: Residual distribution for sensor S25 using the binary hit reconstruction algorithm at zero degrees relative to the beam.

To compare the different contributions to the binary residual distribution it was plotted depending on the cluster size, shown in Figures 6.20. The size 1 distribution (a) is identical to that of Figure 6.10 (a), as expected. The residual widths begin to decrease with increasing cluster size. This is can be understood by considering both the reconstructed hit position and the track position. As discussed in Section 6.1.1, the size 3 and 4 clusters are likely to have a pixel width of two in each direction. Therefore, the reconstructed hit position will be on the very edge between the two pixels. This means that the reconstructed hit position for clusters size 2, 3 and 4 will be the same and any variations in the residual width comes from the track positions. The intra-pixel track positions that lead to the different cluster sizes was shown in Figures 6.2. It was shown that tracks forming size 3 and 4 clusters occur mostly close to the corners of the pixel. These areas are smaller in width than the area with which size 2 clusters occur, which explains the smaller position resolution.

In the VELO upgrade TDR [5], a simulation was performed to predict the binary residual distributions. Figure 6.21 compares the distributions for all cluster sizes (black), size 1 (red) and size 2 (purple). The shapes and widths compare well with the TimePix3 binary distributions. This is reassuring that when coupled to VeloPix ASIC, the prototype sensors should be able to deliver the expected binary resolution simulated in the TDR.

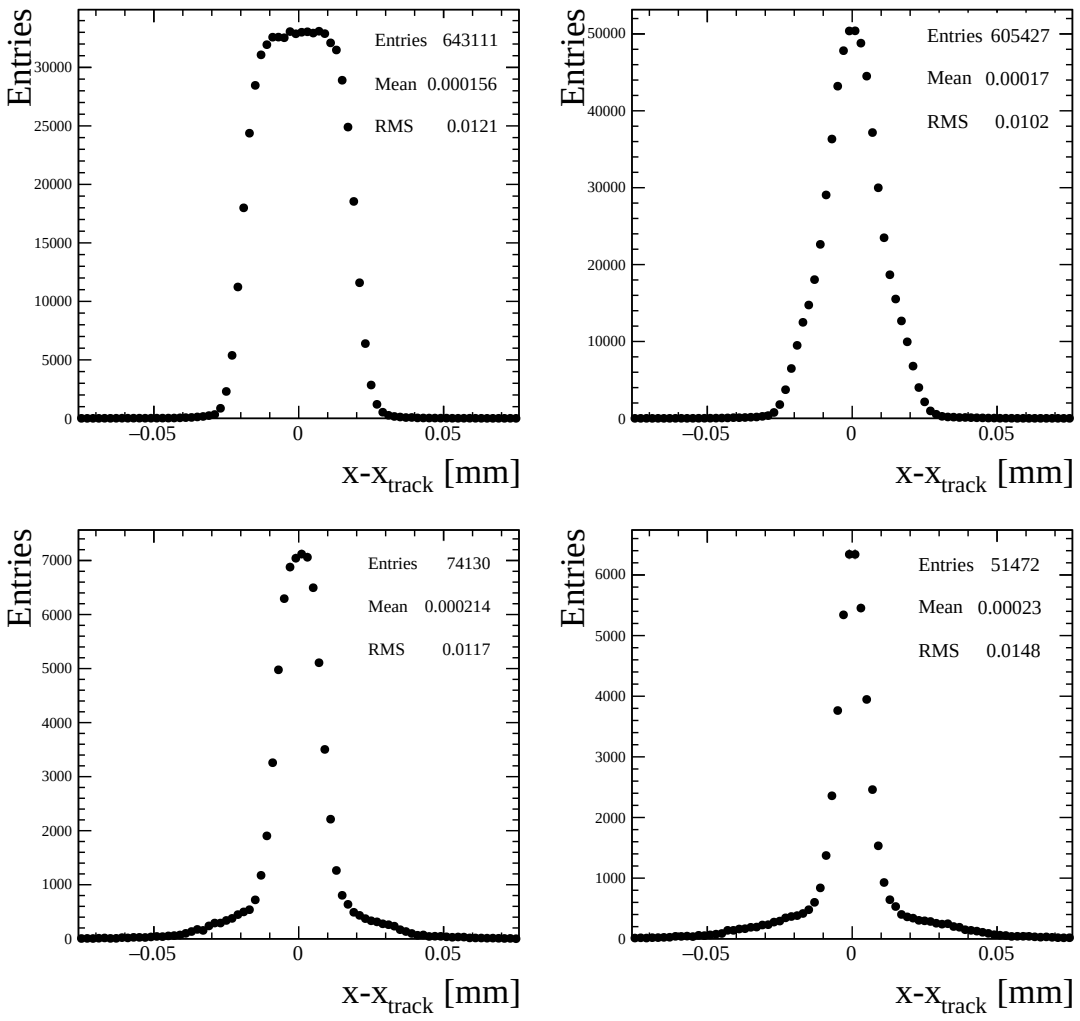


Figure 6.20: The binary residuals depending on cluster sizes 1 (a), 2 (b), 3 (c) and 4 (d) for sensor S25.

Previously for the analogue residual distribution the $ToT_{ratio}$s of size 2 clusters was plotted depending on the residual difference given by the same cluster (Figure 6.13). This identified that asymmetric charge sharing resulted in larger residual differences. For a real binary ASIC, this measurement would not be possible. But since the TimePix3 is an analogue ASIC imitating a binary ASIC the $ToT_{ratio}$s can be measured and plotted depending on the binary residual difference, as shown in Figure 6.22. Overlain is the binary residual distribution for size 2 clusters (in $x$). Similarly, the largest residual differences come from clusters with asymmetric charge sharing, although the residual differences are generally smaller. The size 2 residual differences are governed by the hit positions with in a pixel that lead to size 2 clusters, see Figure 6.2 (b). Hits close to the implant, share less charge with a neighbouring pixel than that of a hit close to the

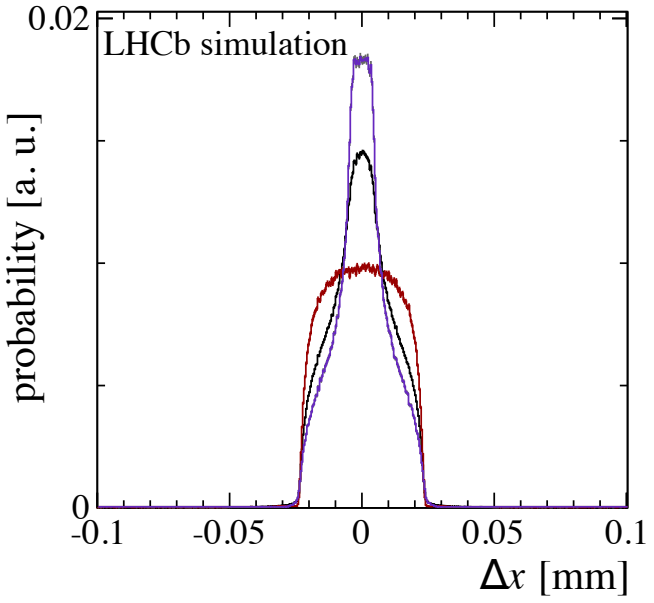


Figure 6.21: Binary residual distributions using LHCb simulation for all cluster sizes (black), size 1 (red) and size 2 (purple).

very edge of a pixel. Therefore tracks traversing furthest from the edge of a pixel, that still result in a size 2 cluster have a higher probability of asymmetric charge sharing and result in the largest residual differences.

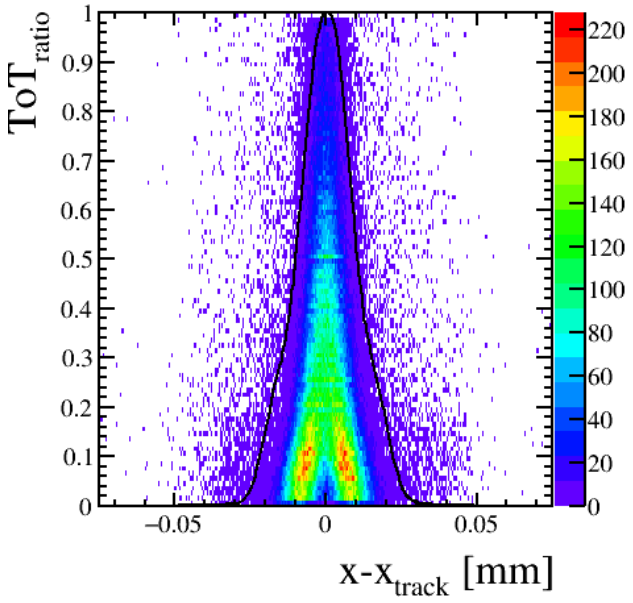


Figure 6.22: The $ToT_{ratio}$s depending on the binary residual difference for size 2 clusters in $x$. Overlain is the normalised binary residual distribution for sensor S25.

### 6.2.4 Analogue and Binary Comparisons

As previously discussed, the two different hit position reconstruction algorithms, analogue and binary result in different spatial resolutions. The spatial resolutions using both reconstruction algorithms are expected to be similar for perpendicular tracks because size 1 clusters dominate the distribution, with the analogue distribution being slightly better due to the ToT information being used in the reconstruction for cluster sizes greater than 1. In reality this was not true because of the non-linear charge sharing degrading the analogue spatial resolution. The measured spatial resolution for perpendicular tracks was 11.8 μm for analogue (before correction) and 10.9 μm for binary. Figure 6.23 (a) shows a plot of the residual differences using the analogue position reconstruction vs the residual differences using the binary reconstruction, for two pixel clusters in the $x$ direction. The distribution is anti-correlated, meaning that a positive binary residual difference gives a negative analogue residual, and vice versa. This can be explained using the illustration in Figure 6.23 (b). For two pixel clusters, the binary hit reconstructed position is the edge between pixels. For analogue, the non-linear charge sharing means the reconstructed position is pulled disproportionately away from the track intercept and closer to the centre of the pixel. With the residual difference calculation being $x - x_{track}$ this results in a positive binary residual difference and a negative analogue residual difference, for this example. The opposite is expected for a hit on the opposite side of the pixel.

To further prove that the positive and negative residual differences are dependent on the side (left or right) of the pixel the particle hits, the intra-pixel track positions were plotted depending on which bin they occurred, illustrated by the rectangles overlain in Figure 6.23 (a). The intra-pixel plots are shown in Figure 6.24 for each bin, left to right.

## 6.3 Bias Voltage

As described in Section 2.2.1, a reverse voltage is applied to a sensor to increase the width of the depletion zone. The bias voltage is directly related to the strength of the electric field and the drift velocity of the charge carriers. Therefore different bias

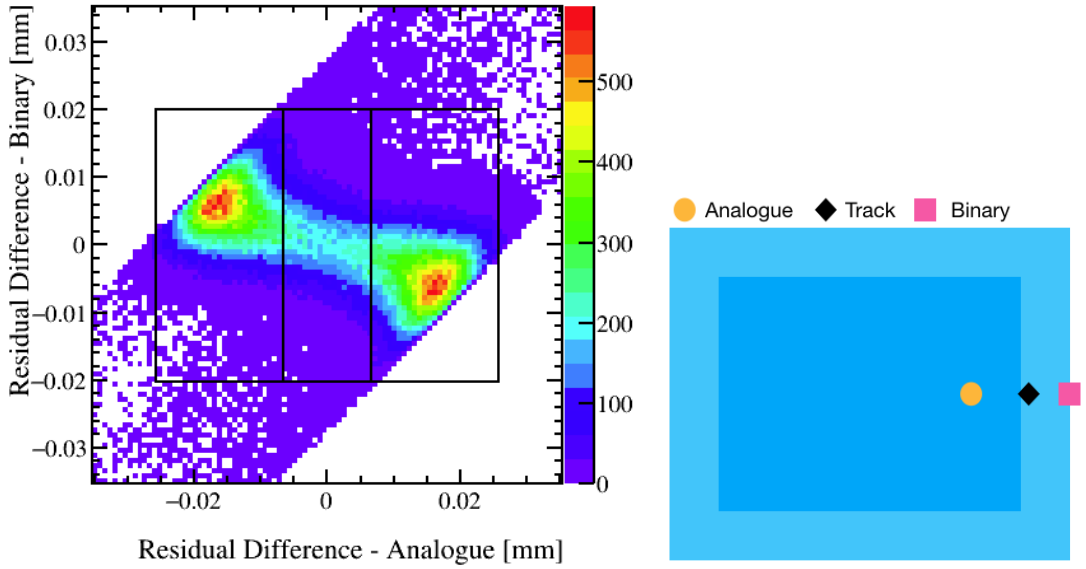


Figure 6.23: (a) The anti-correlation of the analogue residual difference and the binary residual difference for size 2 clusters in $x$, for tracks perpendicular to the sensor (S25). (b) Illustration depicting example binary hit (square), analogue (circle) and track positions within a pixel.

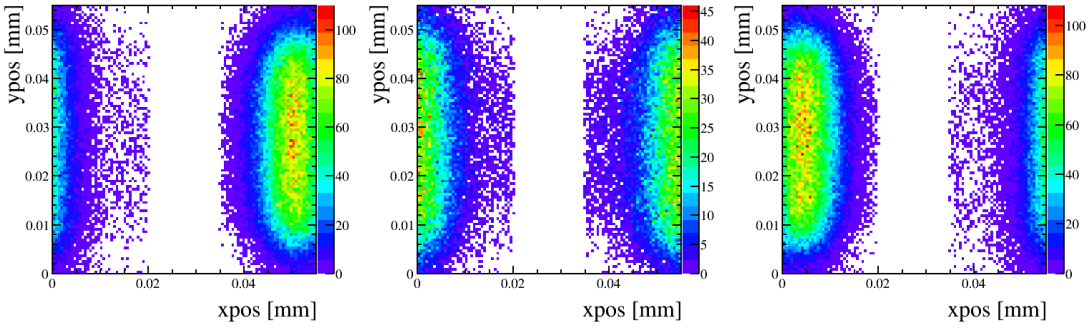


Figure 6.24: The intra-pixel track positions for size 2 clusters in $x$ depending on the bins illustrated in Figure 6.23 for sensor S25.

voltages lead to variations in the charge sharing. The precision at which the position of a charged particle can be reconstructed is dependent on how charge is shared between the pixels, therefore the spatial resolution will vary with the applied bias voltage.

High bias voltages create stronger electric fields, resulting in higher drift velocities and shorter drift times meaning that there is less time for the charge to diffuse laterally to neighbouring pixels. For lower bias voltages, the electric field is weaker and the charge collection time is longer, allowing more time for charge carriers to diffuse. Furthermore, for bias voltages below the full depletion voltage, less charge is generated, leading to smaller cluster signals. Consequently, the division of the charge is different. For lower

bias voltages, more charge is collected in the neighbouring pixels compared to a seed pixel, than at a higher bias. This is quantified by measuring the $ToT_{ratio}$s, first introduced in Section 6.2.1. Figures 6.25 show the $ToT_{ratio}$ distributions of size 2 clusters for a range of different bias voltages for a HPK sensor that has a depletion voltage ~ 120 V. Figures 6.25 (a) and (b) shows the $ToT_{ratio}$s for voltages at depletion and below. It is seen that the peak of the $ToT_{ratio}$ distribution decreases with increasing bias, where $ToT_{ratio}$s tending towards zero represent clusters that have very asymmetric charge division. Clusters with asymmetric charge division, where the second pixel in the cluster has a charge value close to threshold are more susceptible to non-linear charge sharing effects that degrade the hit position reconstruction (Section 6.2.1). This suggests that it is favourable to operate the sensor at lower bias voltages. However, the charge collected in an under depleted sensor is smaller resulting in a poor S/N, and often the charge shared with a neighbouring pixel does not reach threshold leading to a size 1 cluster, degrading the spatial resolution. Figures 6.25 (c) and (d) shows the $ToT_{ratio}$ distributions for voltages above the depletion voltage. There are minimal changes to the $ToT_{ratio}$ distributions as the bias increases. At this point, the probability that charge is shared with a neighbour is reduced leading to a size 1 cluster. If size 2 clusters do occur, the charge division is roughly the same for all bias voltages above depletion.

The variations in the cluster sizes due to the applied bias voltage are shown in Figures 6.26 (a) and (b). In Figure 6.26 (a) the fraction of clusters of a particular size as a function of bias are presented for a 200 µm HPK sensor. As discussed above, the diffusion of charge between neighbouring pixels is largest for very low bias voltages, but the majority of clusters remain size 1 because the charge collected by the neighbour is not high enough to reach threshold. The magnitude of charge generated increases as the bias increases closer to the depletion, meaning that the probability that the shared charge will reach threshold also increases. This increases the fraction of size 2 clusters and consequently decreases the number of size 1. The largest fraction of size 2 clusters occurs at the depletion voltage. Above depletion, the electric field strength continues to increase, reducing the charge sharing and therefore increasing the fraction of size 1 cluster again. As a comparison, the fraction of clusters of a particular size as a function of bias are presented for a 150 µm thick Micron sensor in Figure 6.26 (b). No data

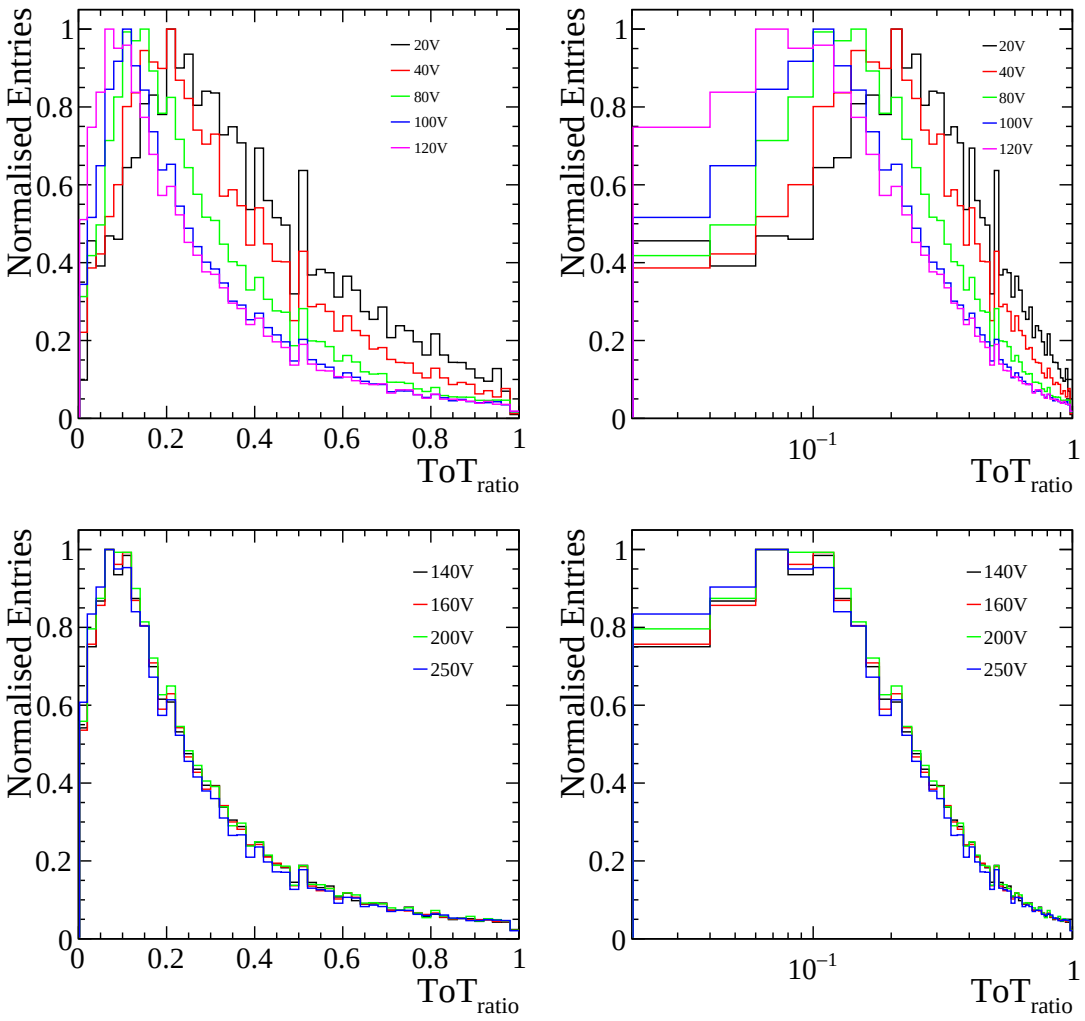


Figure 6.25: The $ToT_{ratios}$s measured for size 2 clusters for a range of different bias voltages for an example HPK sensor (S8). The voltages at depletion and below are show in (a) and (b) and the voltages above deletion in (c) and (d).

was collected for this sensor below the depletion voltage, therefore the size 1 clusters dominate for the full range of bias voltages presented. However, both sensors have a similar behaviour for voltages above depletion.

As discussed in Section 6.1.1, besides the bias voltage the cluster size depends on the hit position of the charge particle within the pixel. For low bias voltages, the width of the charge cloud is large because of the diffusion, but due to the small amount of generated charge the particle would need to hit very close to the pixel edge to create a size 2 cluster. At depletion the sensor bulk is fully depleted and the electric field strength is not too strong that charge can still easily be shared with a neighbour. Therefore a particle can hit relatively close to a pixel implant and charge can still reach threshold in a neighbouring

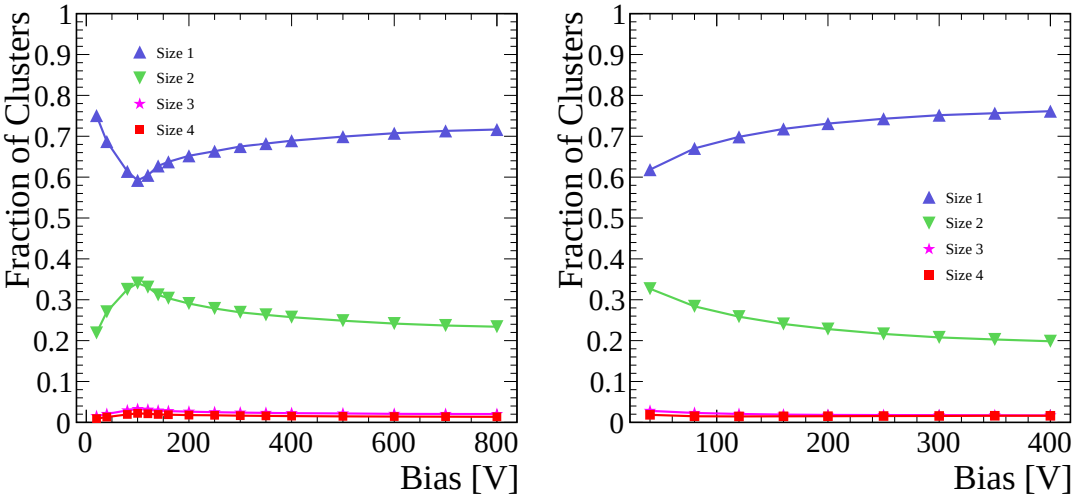


Figure 6.26: Fraction of clusters as a function of bias voltage for a HPK 200 µm thick sensor (S8) (a) and a Micron 150 µm thick sensor (S30) (b).

pixel, increasing the probability of size 2 clusters, as shown in Figure 6.26 (a). Above the depletion, due to the increased field strength and reduced charge sharing, a particle needs to again, hit close to edge of a pixel to create a size 2 pixel. The area of the pixels at which tracks traverse that give rise to size 2 clusters was previously presented for a sensor operated at the depletion voltage placed perpendicular to the beam. An example is shown as a reminder in Figure 6.27. The width of the regions at which size 2 clusters occur in $x$ is quantified by plotting their projections along the $x$-axis. To study only the contributions for size 2 clusters in $x$, only entries in the $y$ range of 0.010 mm to 0.045 mm were included, limiting contributions from size 2 clusters in the $y$-direction. The projections for five different bias voltages, for a 200 µm thick Micron n-on-p sensor (S25) are shown in Figure 6.28. The area at which size 2 cluster occurs, increases with increasing bias until the depletion voltage is reached ($\sim$ 40 V). Above depletion the area at which two pixel clusters occurs begins to decrease. This means that at very low bias and at very high bias, for a size 2 cluster to occur, the charged particle has to hit very close to the edge between two pixels, as expected. The optimum charge sharing occurs when the sensor is operated at the depletion voltage, resulting in the largest fraction of two pixel clusters.

The width of the areas at which size 2 clusters occur in a pixel is related to the size of the charge cloud. The width of charge clouds was defined by Equation 2.12 and for the

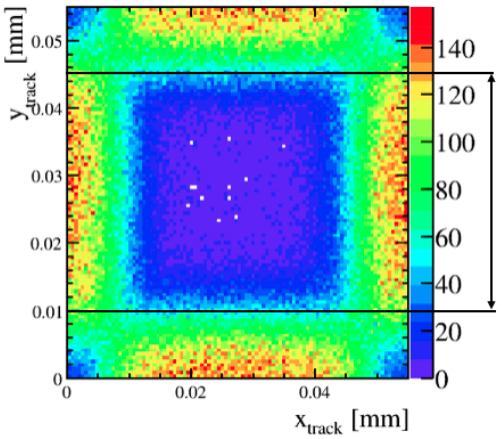


Figure 6.27: Intra-pixel track positions for size 2 clusters for sensor S25 operated at 40 V. To study contributions from size 2 clusters in the $x$-direction, data in the range 0.010 mm and 0.045 mm is considered only, as illustrated by the arrows in the figure.

prototype sensors is expected to be around $5-10$ µm. To extract the width of the size 2 regions, the projections shown in Figure 6.28 were replotted such that the right half of the plot was shifted by 0.055 mm to the left along the $x$-axis, shown in Figure 6.29 (a). The distribution is Gaussian like in shape and the peak is centred around zero, where zero is the very edge between two neighbouring pixels. The distribution for each voltage step was fitted with a Gaussian, where an example fit for the 160 V voltage step is shown in Figure 6.29 (b). The standard deviations $\sigma$ are plotted as a function of bias in Figure 6.30. The $\sigma$ measured at the depletion voltage (40 V) is ~7.4 µm, which is comparable in magnitude to the initial estimate of the charge cloud width for the prototypes.

### 6.3.1 Analogue Spatial Resolution

The spatial resolution is dependent on the charge sharing, charged shared over more than pixel improves the position reconstitution. Given the previous discussion on how the applied bias voltage changes how charge is shared and pixel clusters are formed, the resolution will vary. The best resolution is expected when the fraction of size 2 clusters is greatest and the magnitudes of charge measured on each of the pixels is largest, ensuring a good S/N. Note that the TimePix3 is operated with minimum thresholds of $\sim 1000e^-$ while its noise is $\sim 100e^-$, see Section 4.1.3. Therefore good S/N on the neighbouring

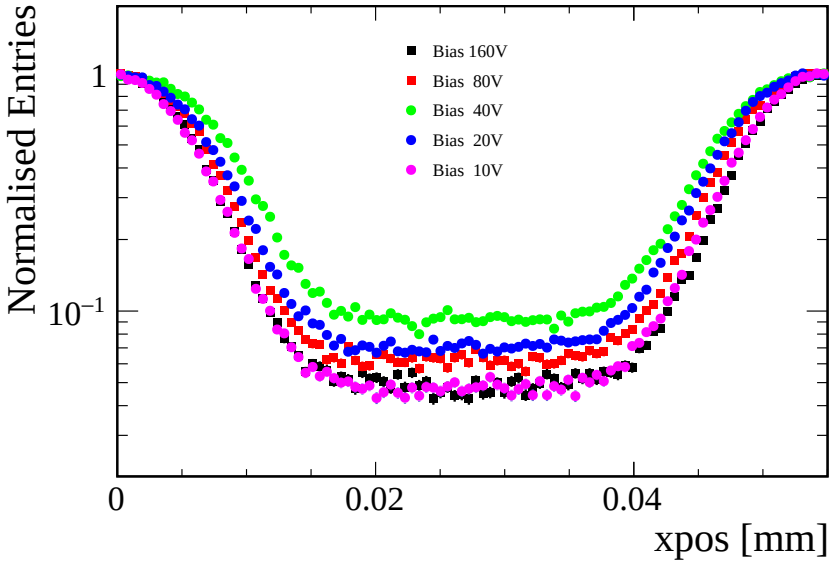


Figure 6.28: The size 2 projections in the $x$-direction for a range of voltages for sensor S25.

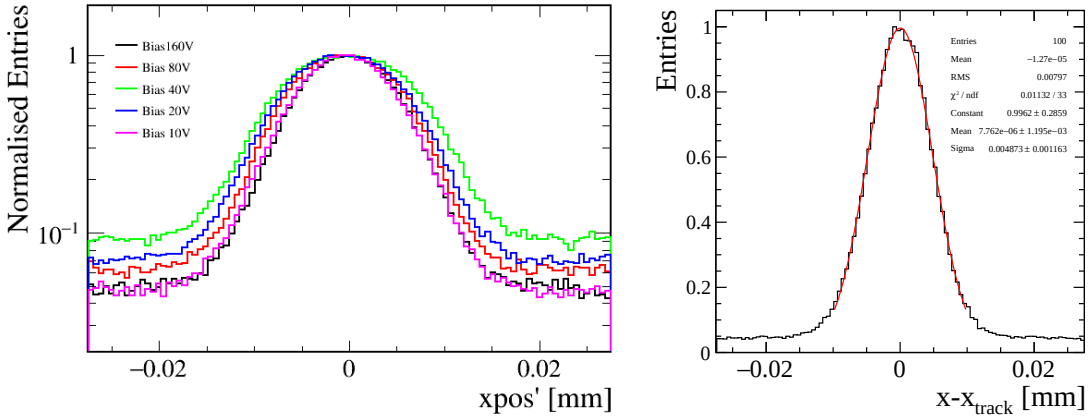


Figure 6.29: The replotted projections, such that the edge between two pixels is centred around zero (a) for sensor S25. An example Gaussian fit to extract the width of the area that size 2 pixels occur in $x$ (b).

pixel is guaranteed. Different spatial resolutions are expected for sensors of different thickness. For a thicker sensor, the generated charge is larger and there is more time for the charge to diffuse. This results in a higher signal on the neighbour and reduces the effects of non-linear charge sharing. Therefore the spatial resolution should be worse for the 150 µm thick sensors.

The spatial resolution was measured using the same method as described in Section 6.2.1. Figure 6.31 (a) shows the spatial resolution in $x$ ($\sigma_x$) as a function of bias for three different HPK sensors. The resolution improves as the bias voltage increases with the best

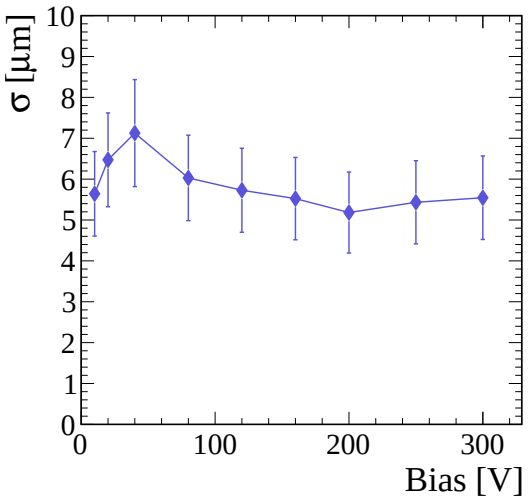


Figure 6.30: The size 2 widths ($\sigma$) in $x$ as a function of bias for sensor S25.

resolution occurring around depletion, as expected. Above depletion, the over biasing reduces the charge sharing between pixels resulting in degraded spatial resolution. The spatial resolution begins to plateau at bias voltages above depletion, as there is no difference in the generated signal nor in the charge sharing. In Figure 6.31 (b), the mean cluster size in column is plotted as a function of bias. The mean cluster size in column is measured instead of the overall cluster size, because the spatial resolution is studied in the $x$-direction only. The mean cluster size trend is the opposite of that seen in the resolution, the charge sharing and hence mean cluster size increases until the depletion is reached, at this point the spatial resolution is optimum. When the sensor is over biased, the mean cluster size begins to decrease, resulting in the degradation of the spatial resolution. The best spatial resolution achieved by each of the sensors and the bias voltage they were measured at are summarised in Table 6.1. All three HPK sensors are the same type and thickness, however there are variations in the measured spatial resolution. S6 and S11 are identical sensors, with the same implant size and follow the same trend but have different magnitudes of spatial resolution. S8 has very similar magnitudes of resolution to S11, but they differ in implant size: S8 has an implant size of 35 μm and S11 has 39 μm. A slightly better resolution is expected for a sensor with a smaller implant, increasing the probability that charge is shared between more than one pixel. This is seen in the data, with S11 having a marginally better resolution than S8. The differences between S6 and S11 are understood and are related to slight differences

| Sensor | Thickness [µm] | Implant [µm] | Best $\sigma_x$ [µm] | Bias [V] | Date |
|---|---|---|---|---|---|
| S6 | 200 | 39 | $12.07 \pm 0.04$ | 80 | May 2015 |
| S8 | 200 | 35 | $12.78 \pm 0.06$ | 100 | July 2015 |
| S11 | 200 | 39 | $12.96 \pm 0.06$ | 80 | July 2015 |
| S23 | 200 | 36 | $11.77 \pm 0.05$ | 80* | May 2015 |
| S25 | 200 | 36 | $11.96 \pm 0.06$ | 40 | July 2015 |
| S31 | 200 | 36 | $11.07 \pm 0.09$ | 30 | May 2015 |
| S30 | 150 | 36 | $12.43 \pm 0.06$ | 40* | July 2015 |
| S33 | 150 | 36 | $11.07 \pm 0.06$ | 20* | May 2015 |
| S34 | 150 | 36 | $10.38 \pm 0.04$ | 10* | July 2015 |

Table 6.1: Table summarising the different prototypes and the best analogue spatial resolution measured, The applied bias voltage at which the best resolution is achieved is also shown, where the * denote the resolutions measured for the lowest bias voltage measured and not necessarily the best achievable resolution of the sensor. The nomial depletion voltages are ~ 120 V for HPK sensors, ~ 40 V for Micron n-on-p and $\lesssim$ 40 V for Micron n-on-n. Variations in the experimental circumstances between different testbeam months resulted in different sptatial resolutions for idential sensors, therefore the date of measurement is also presented.

in the experimental circumstance, further discussed in the Appendix C.

The spatial resolution and mean cluster size in column as a function of bias are shown for Micron sensors: Figures 6.32 for 200 µm thick n-on-p sensors and Figures 6.33 for 150 µm thick n-on-n sensors. A similar trend is seen for the n-on-p sensors in comparison to the HPK sensors, where there is minimum in the spatial resolution around the depletion voltage (~ 40 V). For the n-on-n prototypes, the trends are similar, but no data was collected at bias voltages below depletion, so the best achievable spatial resolution cannot be extracted. The best spatial resolutions measured for each sensor are presented in Table 6.1. All sensors gave similar resolutions between 10 and 13 µm. This is much better than the theoretical perditions of $pitch/\sqrt{12}$, showing that charge sharing significantly improves the position resolution. There is no significant dependence on the implant size. However, this could have been expected as the implant size only varies from 35 to 39 µm inside a 55 µm pitch pixel. It is difficult to compare the performance between the different thicknesses because all data collected for the n-on-n sensors was above the depletion voltage, therefore the optimum spatial resolution could not be extracted.

As mentioned before, the spatial resolution $\sigma_x$ correlates strongly to the mean cluster size in columns. This is shown for prototype sensor S8, in Figure 6.34 where the spatial resolution is plotted as a function of the mean cluster size in column. It can be seen

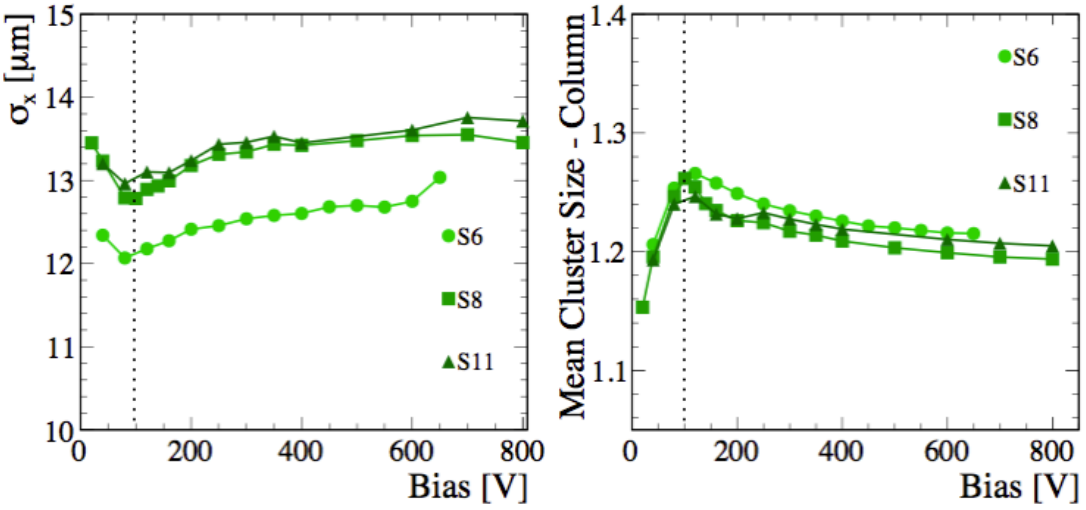


Figure 6.31: The analogue resolution in $x$ as a function of bias for HPK sensors (a) and the mean cluster size in column as a function of bias (b).

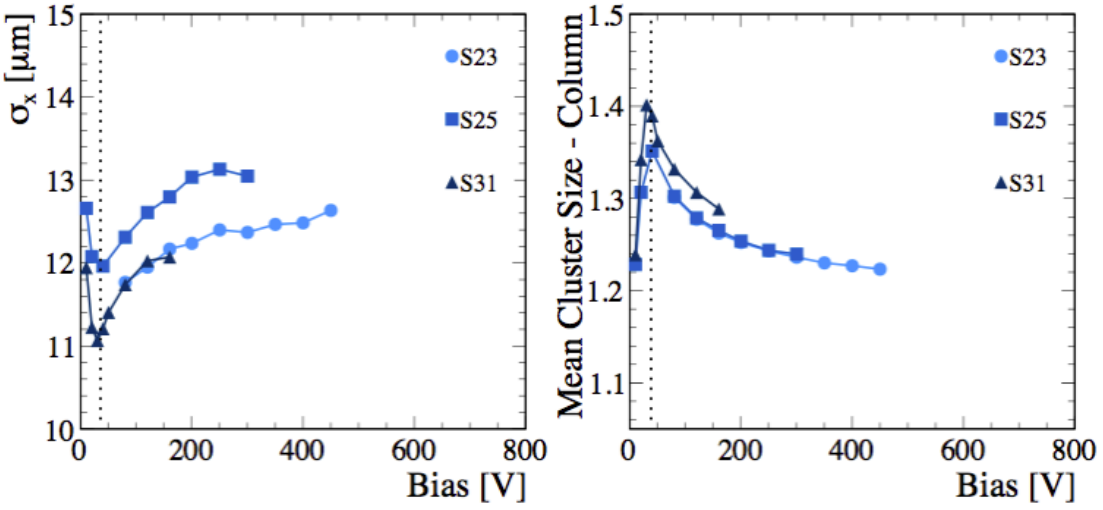


Figure 6.32: The analogue resolution in $x$ as a function of bias for Micron n-on-p sensors (a) and the mean cluster size in column as a function of bias (b)

that for similar cluster sizes, two different $\sigma_x$'s are measured. This is because the charge division before and after the depletion voltage of the sensor is different, as shown in Figure 6.25. Below depletion more charge is measured in the neighbouring pixel compared to the seed than that measured when the sensor is over-biased. Due to non-linear effects being more dominant in asymmetric charge division, see Section 6.2.1, the spatial resolution is better below depletion.

To summarize, the best resolution is achieved when the sensor is operated at the depletion voltage. At depletion, charge is generated in the full thickness of the sensor and the

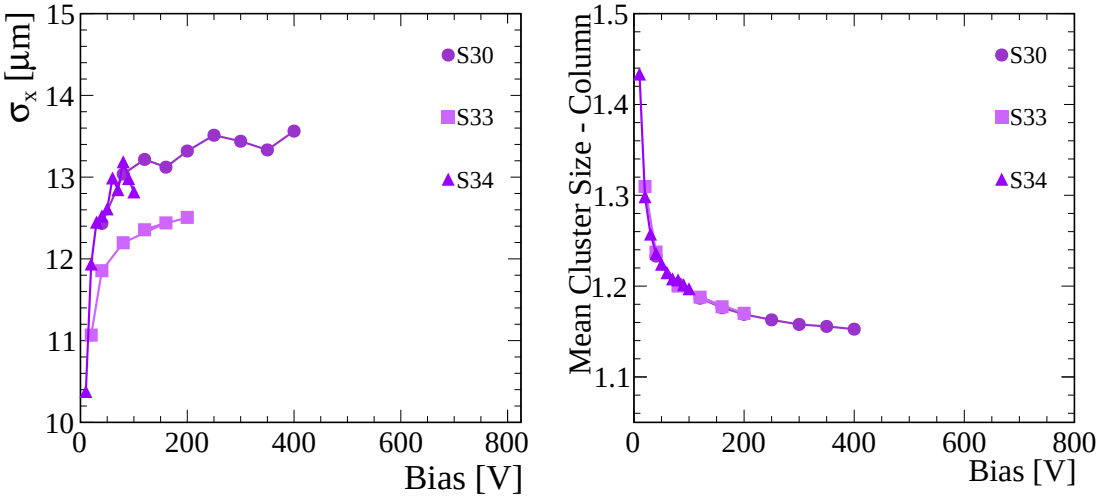


Figure 6.33: The analogue resolution in $x$ as a function of bias for Micron n-on-n sensors (a) and the mean cluster size in column as a function of bias (b)

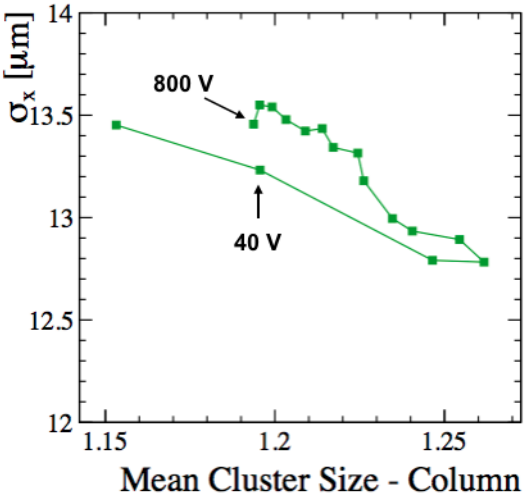


Figure 6.34: The spatial resolution $\sigma_x$ as a function of the mean cluster size in columns for prototype sensor S8. The 40 V and 800 V points are identified highlighting that two different voltages can result in similar cluster sizes but result in different spatial resolution measurements.

sensor is not over-biased, optimising the charge sharing between pixels. A thicker sensor is favourable because more charge is generated. A similar magnitude of resolution was measured for both the HPK and Micron n-on-p 200 µm thick sensors, however the best resolution is achieved at a lower bias voltage for the Micron n-on-p sensors. Minimal differences were measured in the spatial resolution depending on the implant size, this could be that the measurements were not sensitive to the small differences in implant sizes. Theoretically a smaller implant size allows more charge to be shared between pixels, therefore a better spatial resolution is expected in comparison to a larger implant.

This concludes, that the best sensor for the VELO upgrade when comparing analogue position reconstruction, is a 200 µm Micron n-on-p sensor with the smallest implant size available, which is 36 µm.

### 6.3.2 Binary Spatial Resolution

As previous discussed, the VeloPix ASIC will have a binary readout. At the time of testing the sensor prototypes, the VeloPix was not ready, therefore to study the expected performance, the TimePix3 data was converted into binary using the method described in Section 6.2.3. Generally the binary resolution is expected to be worse due to the lack of charge information. The differences stem from the fact that the binary reconstructed hit position is fixed depending on the cluster size, whereas analogue reconstructed hit positions vary depending on the charge division. However it was shown in Section 6.2.3, that for an example sensor, placed perpendicular to the beam and operated at the depletion voltage that the binary resolution was better than analogue. This was due to the non-linear charge sharing effects. It should be noted that when the signals are large enough that the neighbour is out of the non-linear regime, the analogue is expected to be better than binary. For different operational bias voltages, the binary resolution is expected to follow the same trends measured for the analogue resolution, but overall the magnitude of the resolution should remain better than analogue.

The binary spatial resolution was measured using the same method as described in Section 6.2.3. The binary spatial resolution (red) is compared with the analogue resolution (black) for the three example sensors in Figures 6.35: S8 HPK (a), S31 Micron n-on-p (b) and S33 Micron n-on-n (c). In all three examples, the binary resolution is better than the analogue resolution, as expected. Above the depletion voltage the trends are almost identical, where the average difference between the resolutions are 0.44 µm for (a), 0.82 µm for (b) and 0.42 µm for (c). However, for the HPK and Micron n-on-p examples there are slight difference between the trends for bias voltages below depletion. The analogue resolution is still worse than binary but the average difference is smaller. This is because at very low bias voltages, the majority of clusters are size 1. The binary and analogue residual differences are identical for size 1 clusters. However, since there is

still a small fraction of size 2 clusters at low voltages, the analogue resolution is largely influenced by the non-linear charge sharing. Therefore at low bias, the binary resolution is marginally better and improves at a quicker rate because it is not influenced by the non-linear charge sharing.

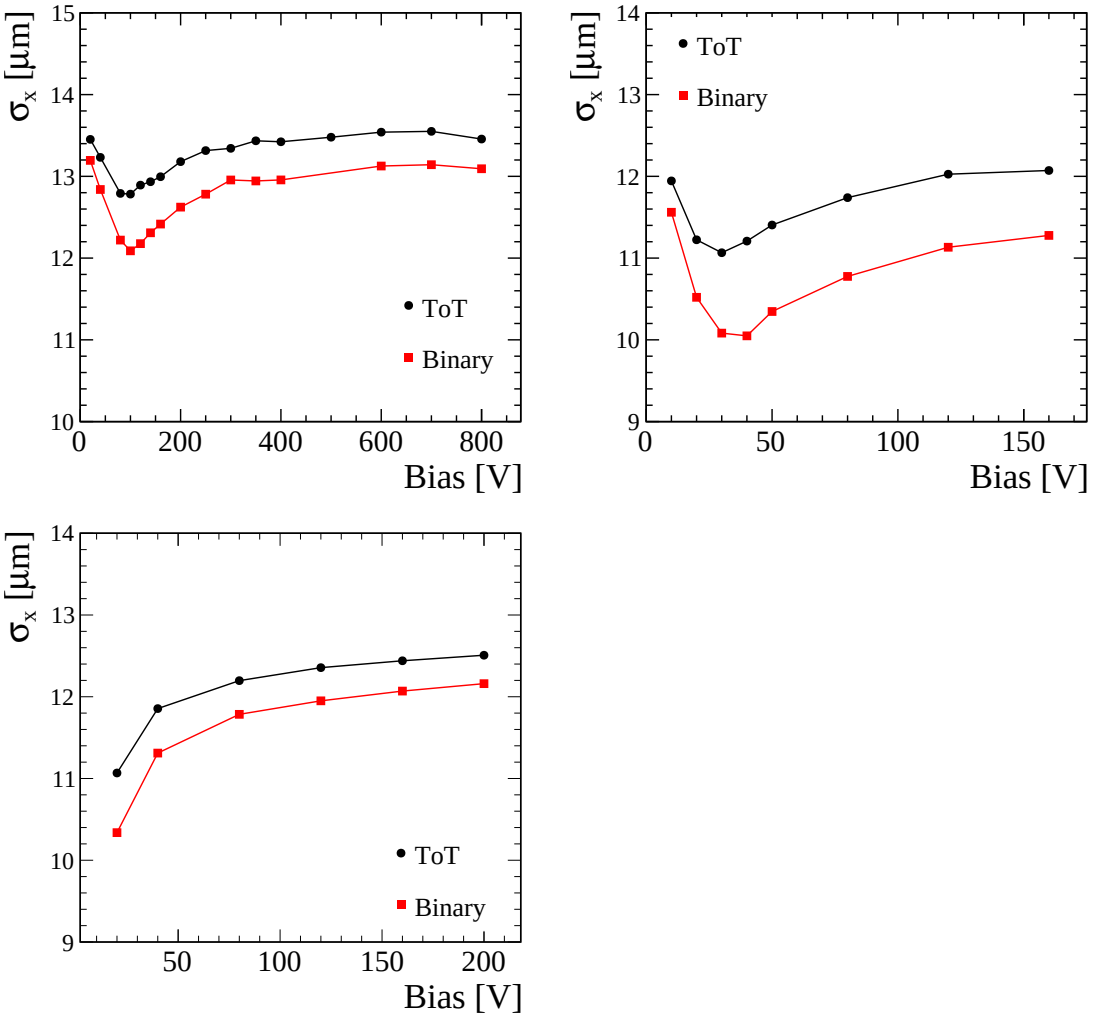


Figure 6.35: Comparison of the spatial resolution in $x$, using analogue reconstruction (black) and binary reconstruction (red). HPK sensor S8 (a), Micron n-on-p sensor S31 (b) and Micron n-on-n sensor S33 (c).

In comparison to the analogue resolutions studied for different bias voltages, the binary resolution is better. The same conclusions can be drawn. The 200 μm thick n-on-p sensor would be a good choice of sensor for the VELO upgrade with the binary results presented suggesting that a binary readout is better. However, it has only been shown that it is better for perpendicular tracks. Variations due to track angle will be discussed in the next section.

## 6.4 Track Angle

As discussed in Section 1.2, the LHCb experiment is optimised to study particles in the forward region and has an acceptance of 10 mrad to 300 mrad. Therefore, the VELO will reconstruct charged particle tracks that are at angles relatively close to the beam line. Figure 6.36 shows the distribution of the projected track angle along $x$ in the upgraded VELO. To study the spatial resolution performance for angled tracks, angle scans where performed focusing on the range between approximately 0° and 24°. The rotation is only in the $x$-direction and the $y$ position is fixed, as described in Section 4.2.

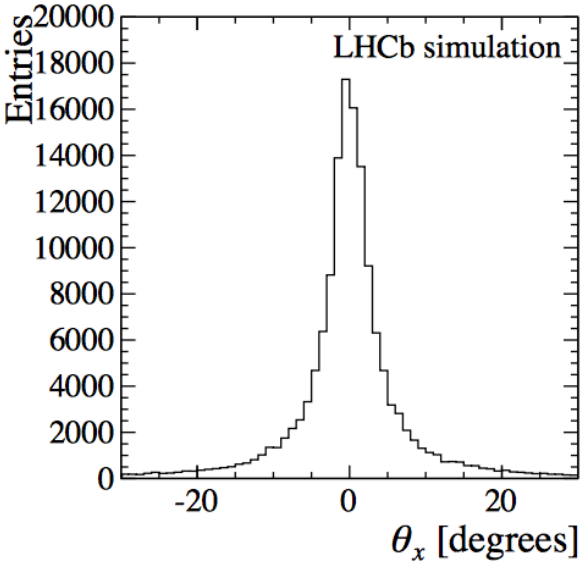


Figure 6.36: Distribution of the projected track angle along the $x$-direction.

For charged particles traversing at an angle, the path of the particle through the sensor bulk is greater than that of a perpendicular track. This results in an increase in the deposited charge. Figure 6.37 shows Landau distributions for three different track angles, 2°, 14° and 24°, for a 200 µm thick sensor (S23).

An increased track angle also increases the probability that charge will be collected by more than one pixel. Figure 6.38 shows an illustration of two tracks traversing a sensor. Both tracks have the same angle but hit the sensor at different locations on the sensor surface. One of the tracks first hits the sensor near the edge between two pixels and the particle traverses the width of two pixels. The deposited charge will be collected by two pixel implants resulting in a two pixel cluster. The other track, first hits the

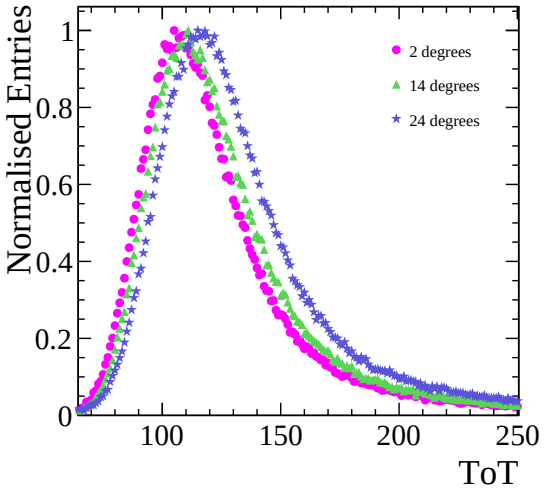


Figure 6.37: Three example Landau distributions for different track angles for sensor S23 operated at 200 V.

surface of the sensor within the area of an implant meaning that the particle traverses almost three pixels. Therefore, charge is collected by three implants. Depending on the magnitude of deposited charge on the third pixel, this track could result in a three pixel cluster. Therefore, the formation of different cluster sizes depends both on the angle of the track and the initial hit location of the particle.

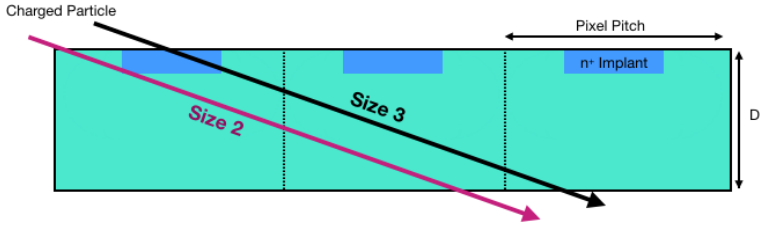


Figure 6.38: Illustration of two track scenarios with the same angle but different incident hit locations, leading two different cluster sizes.

The increase of charge collected by neighbouring pixels to a seed pixel is measured using the $ToT_{ratio}$. Figure 6.39 shows the $ToT_{ratio}$ distributions for size 2 pixel clusters in $x$ for different angles. The peak of the distributions increase with increasing angle, showing that the charge division becomes less asymmetric.

As a reminder, the cluster size distribution for perpendicular tracks is shown in Figure 6.40 (a), where the majority of clusters are size 1. To compare, the cluster size distribution for tracks at an angle of 10° is shown in Figure 6.40 (b). At this angle, the greatest proportion of clusters are size 2. To quantify the change in cluster size as

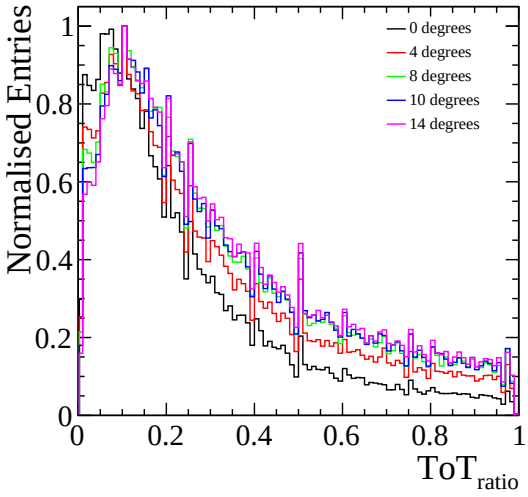


Figure 6.39: $ToT_{ratio}$ distributions as a function of angle for size 2 clusters in $x$ for sensor S25.

a function of angle, the fraction of cluster sizes is calculated for cluster sizes 1 through 4. Figures 6.41 (a) and (b) show the cluster size fractions as a function of angle, for a 200 µm thick n-on-p sensor (a) and a 150 µm thick n-on-n sensor (b). In both plots, as the angle increases the fraction of clusters that are size 2 increases and the fraction of size 1 decreases. In the 200 µm thick sensor (a), at an angle of 16°, the fraction of size 2 clusters is at a maximum, after which the fraction of size 2 cluster begins to decrease and the fraction of size 3 and size 4 clusters begins to increase. For the 150 µm thick sensor (b), the increase in size 2 clusters is more gradual due to the reduced thickness. For a track to traverse two or more pixels, the angle must be larger than that required in a 200 µm thick sensor.

The hit positions within a pixel that lead to the different cluster sizes were shown in Section 6.1.1 for perpendicular tracks. As previously discussed, tracks of the same angle can lead to different cluster sizes depending on the hit position within a pixel. Figure 6.42 shows the intra-pixel track positions depending on the cluster size for sensor S25, operated at 200 V, for three different track angles: 8°. 16° and 22°. The area at which size 1 clusters occur gets progressively narrower in $x$ with increasing angle. At 22° the fraction of clusters that are size 1 is very low, there is no clear trend and the hit positions that result in size 1 clusters is almost random. The widths of the areas in $x$ at which size 2 clusters occur increases with angle and at 16° a particle hit almost

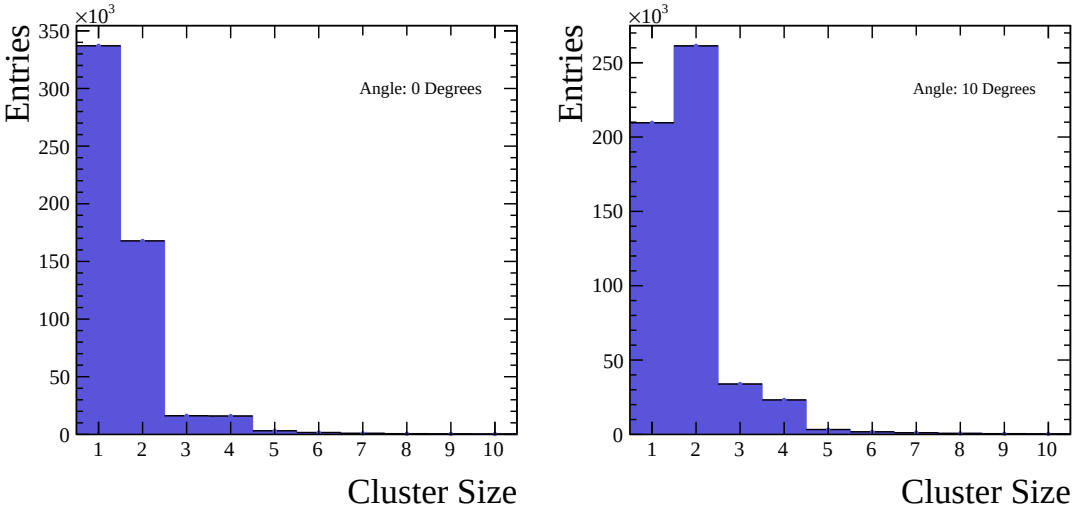


Figure 6.40: Cluster size distributions for sensor S25 placed perpendicular to the beam (a) and placed at 10° relative to the beam (b).

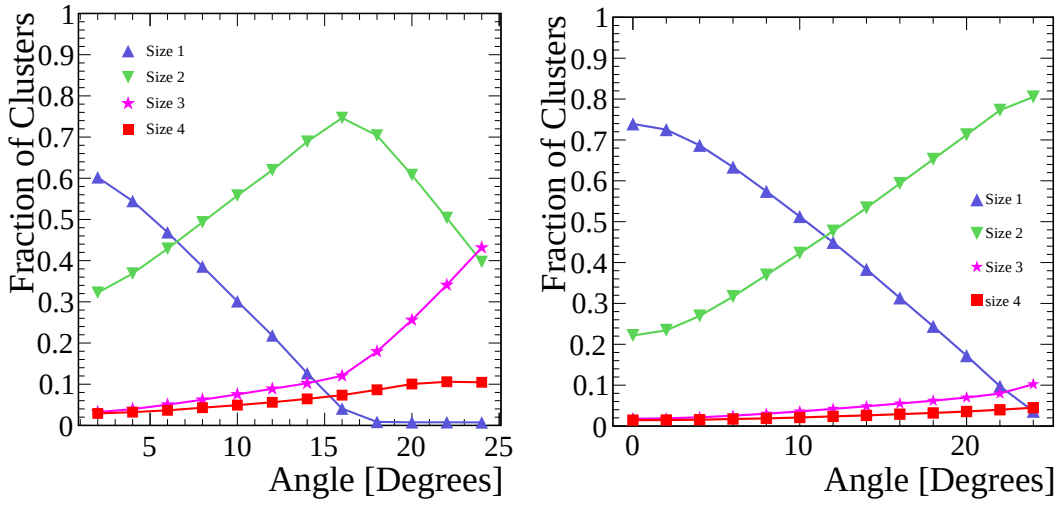


Figure 6.41: The fraction of clusters as a function of angle for a 200 µm thick sensor (S6) (a) and a 150 µm thick sensor (S30) (b).

anywhere in the pixel will result in a size 2 cluster. At 22°, the widths in $x$ begin to decrease again. This is because the fraction of size 3 clusters begins to increase and as illustrated in Figure 6.38, tracks that create size 3 clusters hit the sensor within the area of an implant. This evident when looking at the size 3 cluster distribution for tracks at 22°, where most of the tracks hit the centre of the pixel, though there is still some probability that tracks hitting close to the corner of a pixel will create a size 3 cluster. The hit locations leading to size 4 clusters remains roughly the same width in $y$, but is covers the full width of the pixel in $x$ for high angles. This suggests that particles hitting this area will create a "box" size 4 cluster, with a pixel width of 2 in each direction.

In all cases, the width of the distributions in $y$ remain mostly the same, because the rotation is only in the $x$-direction. One exception is for size 2 clusters created from tracks traversing at 22°, there appears to be minimal entries in the top and the bottom of the plot suggesting that at large angles, the probability of size 2 clusters occurring in the $y$ direction is very low.

To quantify the variations due to the track angle, the projection along the $x$-axis for the size 2 distribution was plotted, using the same method introduced for the bias scans in Section 6.3. Figures 6.43 shows the projections for a range of angles, split between low (a) and high (b). In Figure 6.43 (a), the area at which two pixel clusters occur in the pixel, increases with increasing angle. This trend continues Figure 6.43 (b), for tracks at an angle of 14° (black circles) and 16° (red squares), where the distribution almost flattens at the peak angle of 16°. However, for angles greater than 16°, the region in which size 2 clusters occur begins to decrease. This is due to the increase in the number of size 3 clusters.

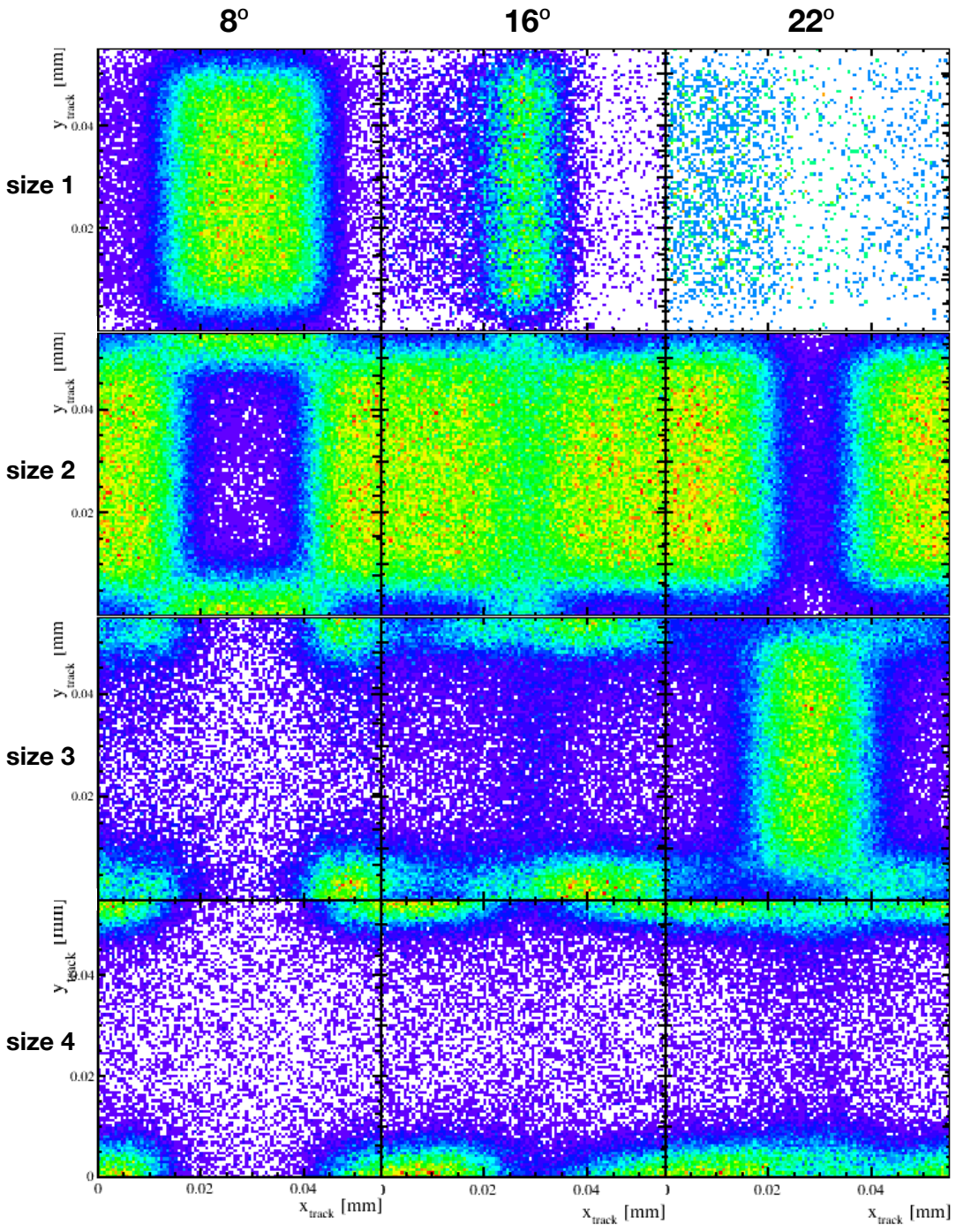


Figure 6.42: Intra-pixel track positions depending on cluster size for sensor S25 operated at 200 V placed 8°, 16° and 22° relative to the beam.

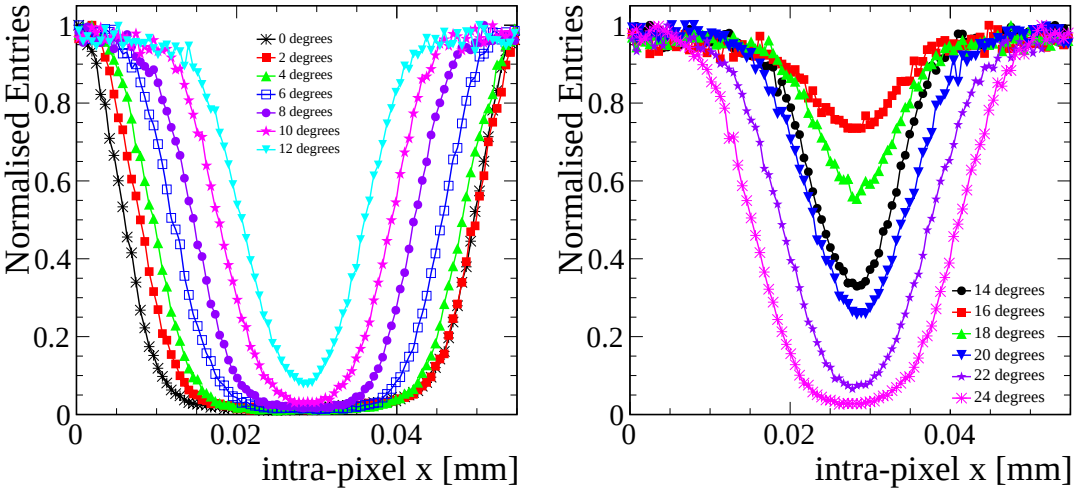


Figure 6.43: Size 2 projections along $x$ for a range of low angles (a) and high angles (b) for sensor S25.

### 6.4.1 Analogue Spatial Resolution

It was previously shown that for perpendicular tracks the Centre of Gravity (CoG) position reconstruction is influenced by non-linear charge sharing, which mostly affects clusters that have very asymmetric charge division (Section 6.2.1). For particle tracks traversing at angles, more charge will be generated in neighbouring pixels to the seed, making the charge division more symmetric. This means that the non-linear effects will be less dominant and the reconstructed hit positions become more accurate, reducing the residual differences between the hit position and the track position. Examples of three residual distributions in $x$ are shown in Figures 6.44 for angles 4° (a), 10° (b) and 16° (c). Visibly, the widths of the distributions decrease with increasing angle and the distinctive "double peak" is no longer a feature of the residual distribution. These distributions were then fit with a Gaussian to extract the spatial resolution.

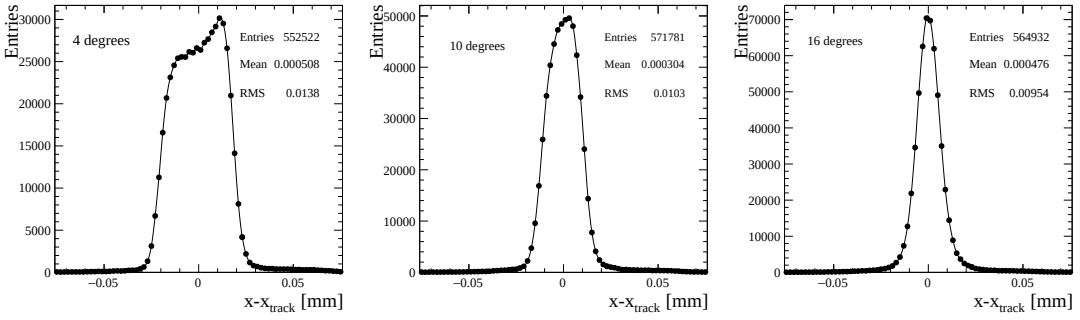


Figure 6.44: Example analogue residual distributions for track angles: 4° (a), 10° (b) and 16° (c) for sensor S25 operated at 200 V.

The spatial resolution in $x$ as a function of angle for HPK sensors S6, operated at 200 V is shown in Figure 6.45. The resolution improves as the angle increases and the optimum resolution is 4.7 μm, which is achieved at angle of ~6° where the fraction of size 2 clusters is highest, as shown in Figure 6.41 (a). Above 16° the fraction of size 2 clusters decreases and the fraction of size 3 increases, consequently this causes the resolution to degrade. This is because of fluctuations along the path length of the charged particle. Hence, the measured signals in the individual pixels are no longer dominated by the path length through those pixels, which deteriorates the position reconstruction.

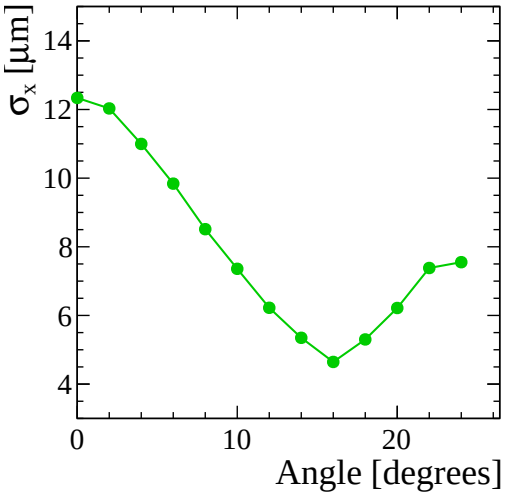


Figure 6.45: The spatial resolution in $x$ as a function of angle for HPK sensor S6.

| Sensor | Thickness [μm] | Implant [μm] | Best $\sigma_x$ [μm] | Angle [°] | Date |
|---|---|---|---|---|---|
| S6 | 200 | 39 | 4.65 ± 0.18 | 16 | May 2015 |
| S8 | 200 | 35 | 5.58 ± 0.05 | 16 | July 2015 |
| S11 | 200 | 39 | 5.70 ± 0.07 | 16 | July 2015 |
| S23 | 200 | 36 | 5.25 ± 0.08 | 14 | May 2015 |
| S25 | 200 | 36 | 6.14 ± 0.07 | 14 | July 2015 |
| S30 | 150 | 36 | 5.19 ± 0.05 | 22 | July 2015 |
| S31 | 150 | 36 | 5.77 ± 0.04 | 22 | May 2015 |

Table 6.2: Table summarising the different prototypes and the best spatial resolution measured and the angle it was measured at. All sensors were operated at a bias voltage of 200 V.

To compare the different prototypes the spatial resolution in $x$ as a function of angle for all prototypes tested are shown in Figure 6.46. All sensors were operated at 200 V. The HPK (green) and Micron n-on-p (blue) sensors have similar resolutions and the optimum angle is also roughly the same because they have identical sensor thickness. For the Micron 200 μm thick n-on-n (purple) sensors, the resolution is generally worse for the majority of the angle scan in comparison to the thicker 200 μm n-on-p sensors. This is because the path length of the charged particle through the n-on-n sensor is shorter than that of a charged particle traversing a 200 μm sensor at the same angle. This means that less charge is generated in neighbouring pixels. At an angle ~22° there is slight a minimum in the resolution trend, where the best resolution is similar to that measured by the n-on-p sensors. The best resolution measured and the angle they were achieved at are summarised in Table 6.2.

To summarize, a 150 µm thick n-on-n sensor is able to achieve the same magnitude of optimal spatial resolution in comparison to the 200 µm n-on-p sensors, but at a much higher angle. This is because all sensors have the same pixel pitch. Due to the acceptance of the LHCb experiment, the VELO is designed to study tracks at small angles close to the the beamline (Figure 6.36). Therefore, a 200 µm thick sensor is a better choice for the VELO upgrade because it achieves better resolution at a smaller angle.

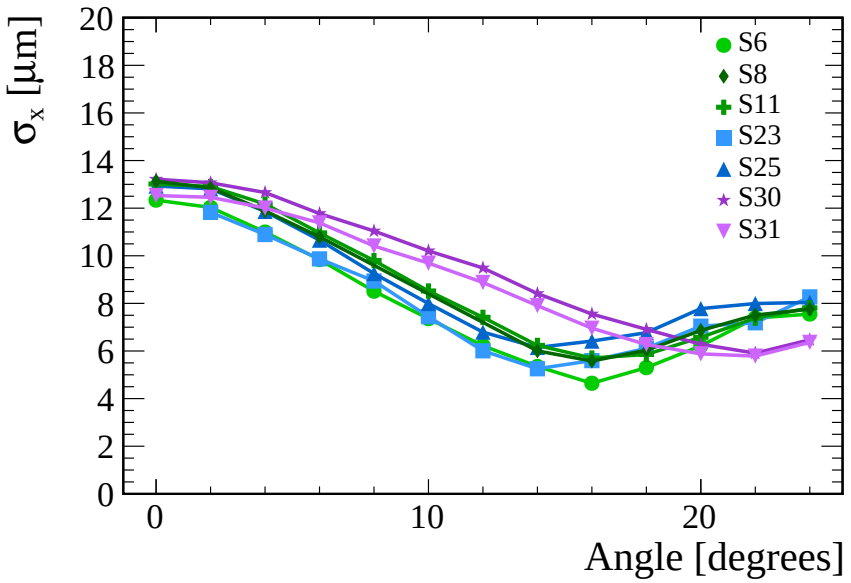


Figure 6.46: The spatial resolution in $x$ as a function of angle for all prototypes tested: 200 µm thick HPK (green), 200 µm thick Micron n-on-p (blue) and 150 µm thick Micron n-on-n (purple). All sensors were operated at a bias voltage of 200 V

### 6.4.2 Binary Spatial Resolution

The binary spatial resolution is also expected to improve with angle. For analogue reconstruction, charge sharing between pixels is important to improve the performance of the position reconstruction. This is also true for binary, but the reconstructed position is fixed depending on the cluster size. For example, the reconstructed position for size 1 clusters is the centre of the pixel and for size 2 it is the very edge between pixels. Therefore, the optimum binary resolution and the angle at which it is measured, may differ from the analogue resolution.

Figures 6.47 shows three example binary residual distributions in $x$ measured at: 4° (a), 10° (b) and 16°. The residual distributions were fitted with a Gaussian and the spatial resolution for a subset of prototypes are shown in Figure 6.48. The best resolution for the 200 µm thick prototypes is ~ 9 µm, which is ~ 4 µm worse than the best spatial resolution measured using analogue reconstruction. Also, the angle at which the best resolution is measured at ~ 8° which is much lower than that measured for analogue (~16°). This is understood when looking at the cluster sizes. At 8° the fraction of clusters that are size 1 is ~ 50% and the fraction that are size 2 is ~ 40% (Figure 6.41 (a)). The intra-pixel track position depending on cluster size for a sensor placed at 8° to the beam was previously presented in Figures 6.42. The projections of the size 1 and size 2 distributions are shown in Figures 6.49 (a) and (b). It is shown that the width of the area of which size 1 clusters occurs in $x$ is roughly the same as the widths of which size 2 clusters occur in (either side of the pixel). In binary reconstruction, the reconstructed hit position $x$ is the centre of the pixel for size 1 clusters and the very edge between two pixels for size 2, illustrated in Figures 6.49 by vertical red lines. Therefore at this angle, the maximum residual differences between the hit position and track positions are roughly the same for both clusters sizes, and the fraction of their occurrences are very similar. Above 8° the resolution degrades because the fraction of size 2 clusters increases and the area at which the occur in the pixel also increases. Due to the reconstructed hit position of size 2 clusters being fixed at the edge between two pixels the residual differences increase i.e. the resolution degrades. At ~ 18° the resolution begins to improve again. The angle scan stops at 24° and the resolution appears to be reaching a minimum similar

in magnitude to that observed at 8°. The minimum is not quite reached suggesting that it will occur at an angle a couple of degrees higher. This argument is supported by the fraction of cluster plot shown in Figure 6.41 (a). At ~ 24° the fraction at size 2 and size 3 clusters are roughly equal, this is a similar behaviour to that seen at 7° where size 1 and size 2 are roughly equal. The intra-pixel track positions for size 3 clusters at high angles was shown in Figure 6.42, where the majority of the hits occur in the centre of the pixel and the area at which size 2 clusters begins to decrease. For size 3 clusters the reconstructed binary hit position is the centre of the middle pixel in the cluster, therefore this behaviour is beginning to mirror that of the size 1 and size 2 at an angle of 8°. The maximum residual differences between the hit position and track positions is roughly the same for both cluster sizes, and the fraction of their occurrences are very similar. A similar trend is seen for the micron n-on-n sensor, but the best resolution of ~ 9 µmoccurs at 14° due to the different thickness.

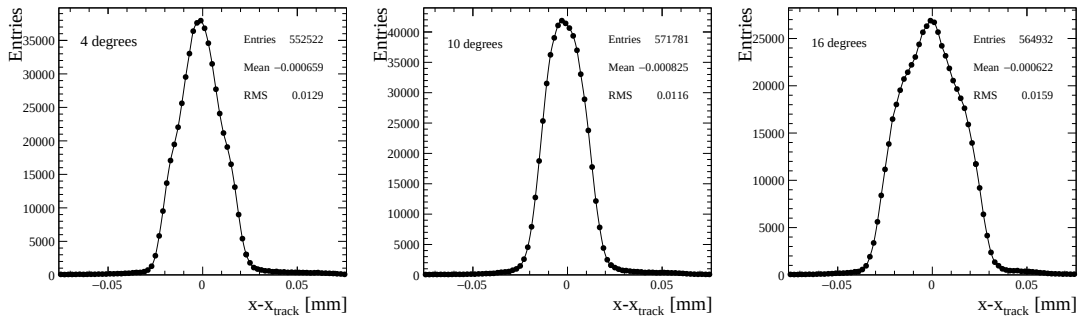


Figure 6.47: Example binary residual distributions in $x$ for angles: 4° (a), 10° (b) and 16° (c) for sensor S25 operated at 200 V. All sensors were operated at a bias voltage of 200 V

During the development of the VELO Upgrade TDR, LHCb simulation studies were performed to estimate the expected spatial resolution performance for a 200 µm sensor. Both analogue and binary resolutions were simulated and are shown in Figure 6.50 (a). To compare, the analogue and binary resolutions measured with real data for sensor S6 is shown in Figure 6.50 (b). Both have similar trends and magnitudes of spatial resolutions. It is seen that the binary resolution is slightly better at smaller angles. This is due to non-linear charge sharing degrading the analogue resolution. However, for angles greater than ~ 8° the binary resolution begins to degrade and the analogue resolution continues to improve.

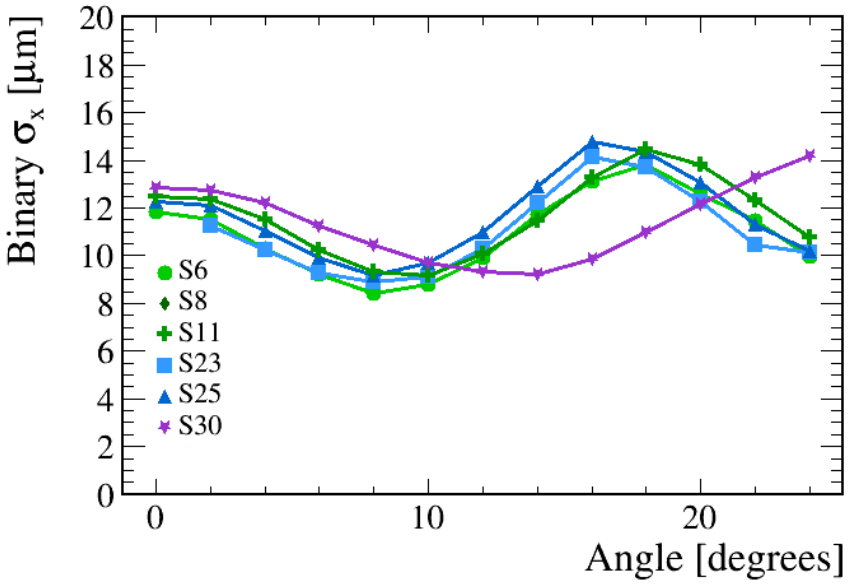


Figure 6.48: The binary spatial resolution in $x$ as a function of angle for all prototypes tested: 200 µm thick HPK (green), 200 µm thick Micron n-on-p (blue) and 150 µm thick Micron n-on-n (purple).

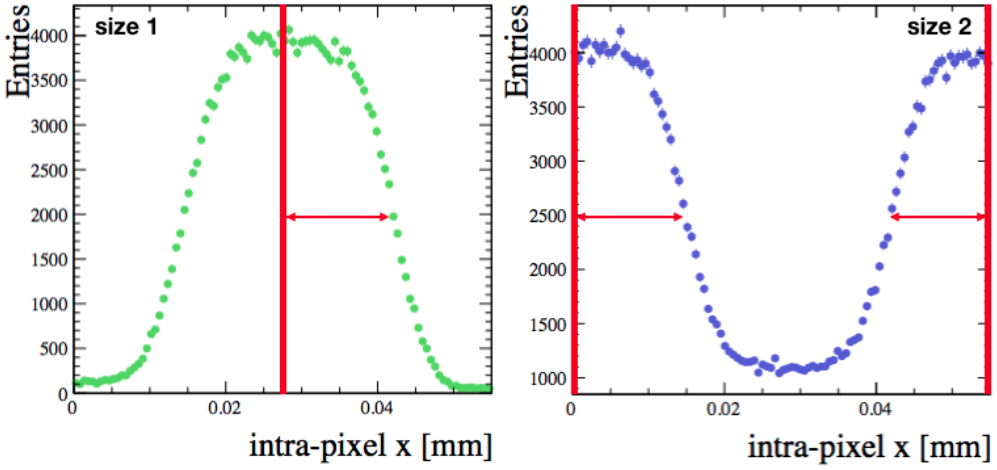


Figure 6.49: Projection of the intra-pixel track positions in $x$ for size 1 clusters (a) and size 2 clusters (b). Vertical lines represent the binary reconstructed hit positions.

## 6.5 Track Angle and Bias Voltage Comparisons

Previously the angles scans presented were for sensors operated at 200 V which is above the depletion voltage for all of the prototypes. Additional measurements were taken at testbeam to compare the analogue spatial resolution performance of the sensors when both the angle and bias voltage were varied. Figure 6.51 (a) shows the spatial resolution in $x$ as a function of angle measured when the sensor was operated at different bias voltages for HPK sensor S6. The corresponding mean cluster sizes in column are shown

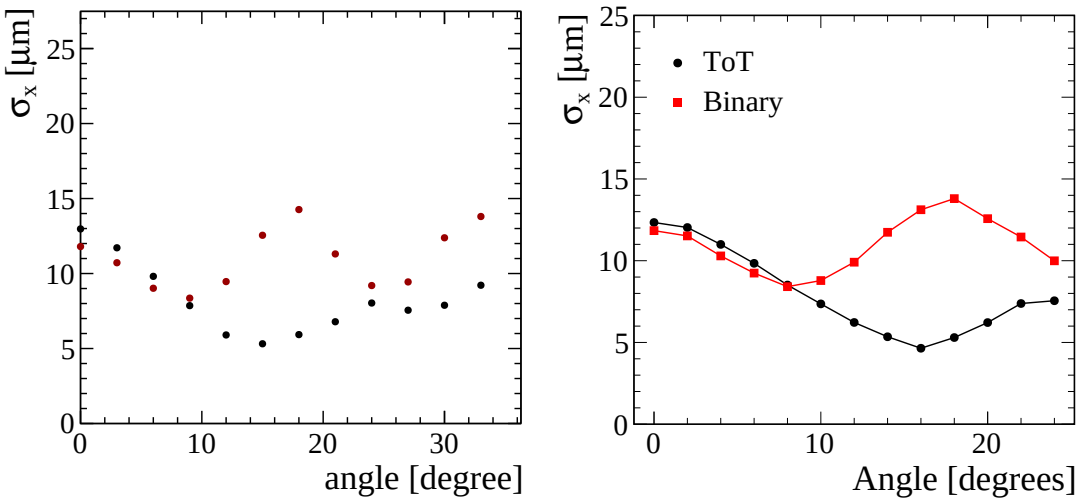


Figure 6.50: Binary and analogue resolutions measured using LHCb simulation (a) and the equivalent measured using data (b).

in Figure 6.51 (b). At the depletion voltage of 120 V the resolution trend is identical to the one shown in Figure 6.46. However, for the angle scans take at lower voltages (40 V & 80 V) the resolution is worse. This is because, for bias voltages below depletion the sensor bulk is not fully depleted and the effective thickness of the sensor is less. Therefore, these resolution trends are roughly comparable with the 150 µm n-on-n sensors resolution trends shown in Figure 6.46. The mean cluster sizes are smaller at lower lower bias, because the sensor bulk is not depleted.

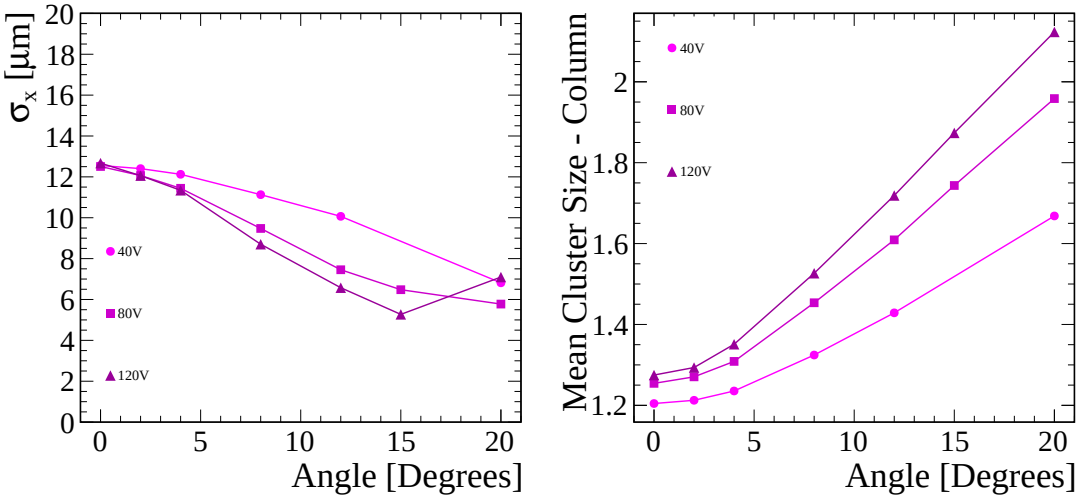


Figure 6.51: The spatial resolution in $x$ as a function of angle for different bias voltages for HPK sensor S8 (a) and the mean cluster size in column as a function of angle for different bias voltages (b).

## 6.6 Intra-Pixel Studies

Previously it was shown in Section 6.2.2 that the correlation of the intra-pixel track positions and the intra-pixel hit positions was not linear across the pixel area, see Figure 6.14. This was demonstrated for clusters sizes 2, 3 and 4, when the sensor was placed perpendicular to the beam and operated around the depletion voltage. The variations across the pixel were because of the non-linear charge sharing. It was also mentioned that these correlations are expected to change with angle and bias, making the correction outlined in Section 6.2.2 impracticable because new calibration curves would be needed for tracks at different angles and sensors operated at different bias voltages.

The variations in the correlations due to angle and bias are because of the difference in charge sharing properties. As previously discussed in Section 6.4, tracks traversing at angles generate more charge which is shared over more pixels in comparison to perpendicular tracks. The higher charge collection on neighbouring pixels means that non-linear charge sharing is no longer a dominant feature and the precision with which the hit position can be reconstructed improves. This suggests that for increasing angles, the position reconstructed by the track and the reconstructed hit position reconstruction converge towards the same value, improving the spatial resolution. This was proven to be true in Figure 6.46. The correlations of the size 2 intra-pixel track position $x_{track}$ and the intra-pixel reconstructed hit position $x$ for tracks at different angles are shown in Figure 6.52, for sensor S25 operated at 200 V. The correlations are visibly linear at higher angles.

The best spatial resolution was observed at the depletion voltage, see Section 6.3. Below the depletion voltage, the drift velocities are slower allowing charge carriers to diffuse to neighbouring pixels, but because of the lower charge collection they often do not reach threshold resulting in a large fraction of size 1 clusters, degrading the resolution. Above the depletion, the charge collection is greatest, but over biasing of the sensor reduces the charge sharing, again degrading the resolution. The correlations of the size 2 intra-pixel track position $x_{track}$ and the intra-pixel reconstructed hit position $x$ for a sensor

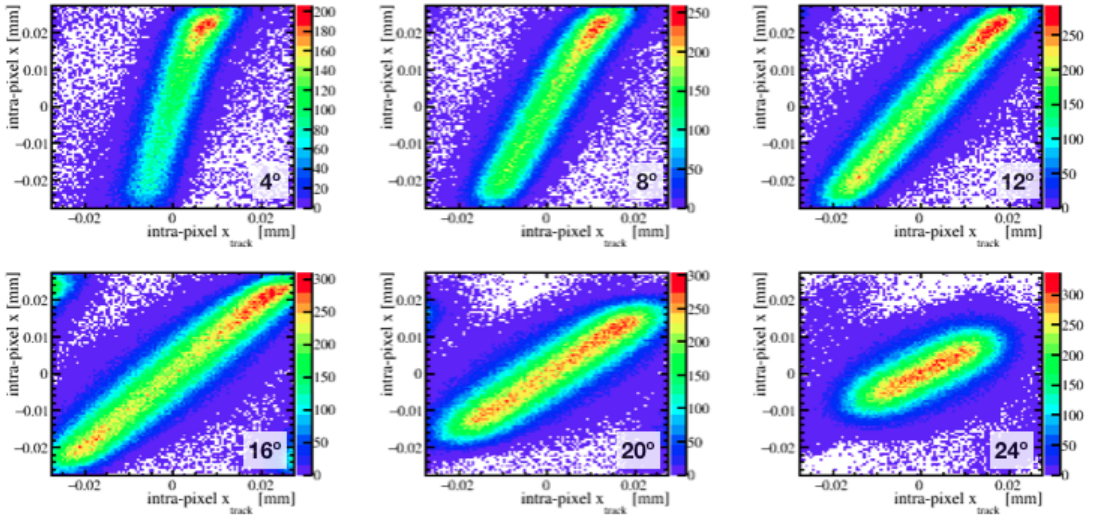


Figure 6.52: The correlations of the size 2 intra-pixel track position $x_{track}$ and the intra-pixel reconstructed hit position $x$ for tracks at different angles, for sensor S25 operated at 200 V.

placed perpendicular to the beam and operated at different bias voltages are shown in Figure 6.53, for sensor S8.

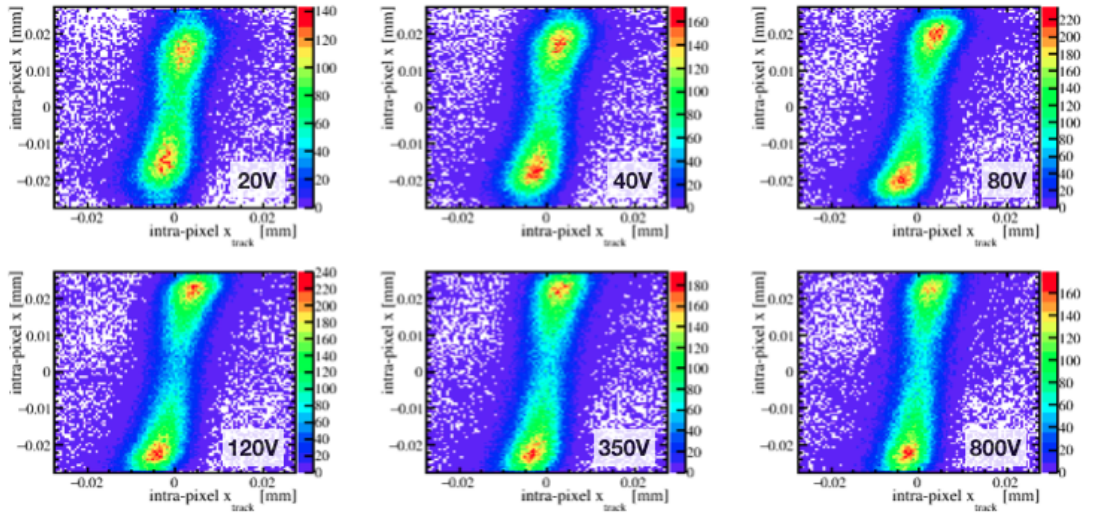


Figure 6.53: The correlation of the size 2 intra-pixel track position $x_{track}$ and the intra-pixel reconstructed hit position $x$ for perpendicular tracks for a range of different bias voltages, for sensor S8.

To quantify the changes in the correlations, calibration curves were produced using the same method described in Section 6.2.2. An example calibration curve is shown in Figure 6.54 (a), for sensor S25, placed perpendicular to the beam and operated at 40 V. A good variable to measure and compare for different angles and bias voltages is the gradient of the "linear" part of the distribution. To determine a range at which to fit a

straight line, each point on the $x$-axis was subtracted from the central point ($x_{centre} - x_i$). The differences are shown in Figure 6.54 (b). The fitting range was defined as 0.8 of the histogram. The resulting fit to the calibration curve is shown in Figure 6.54 (c).

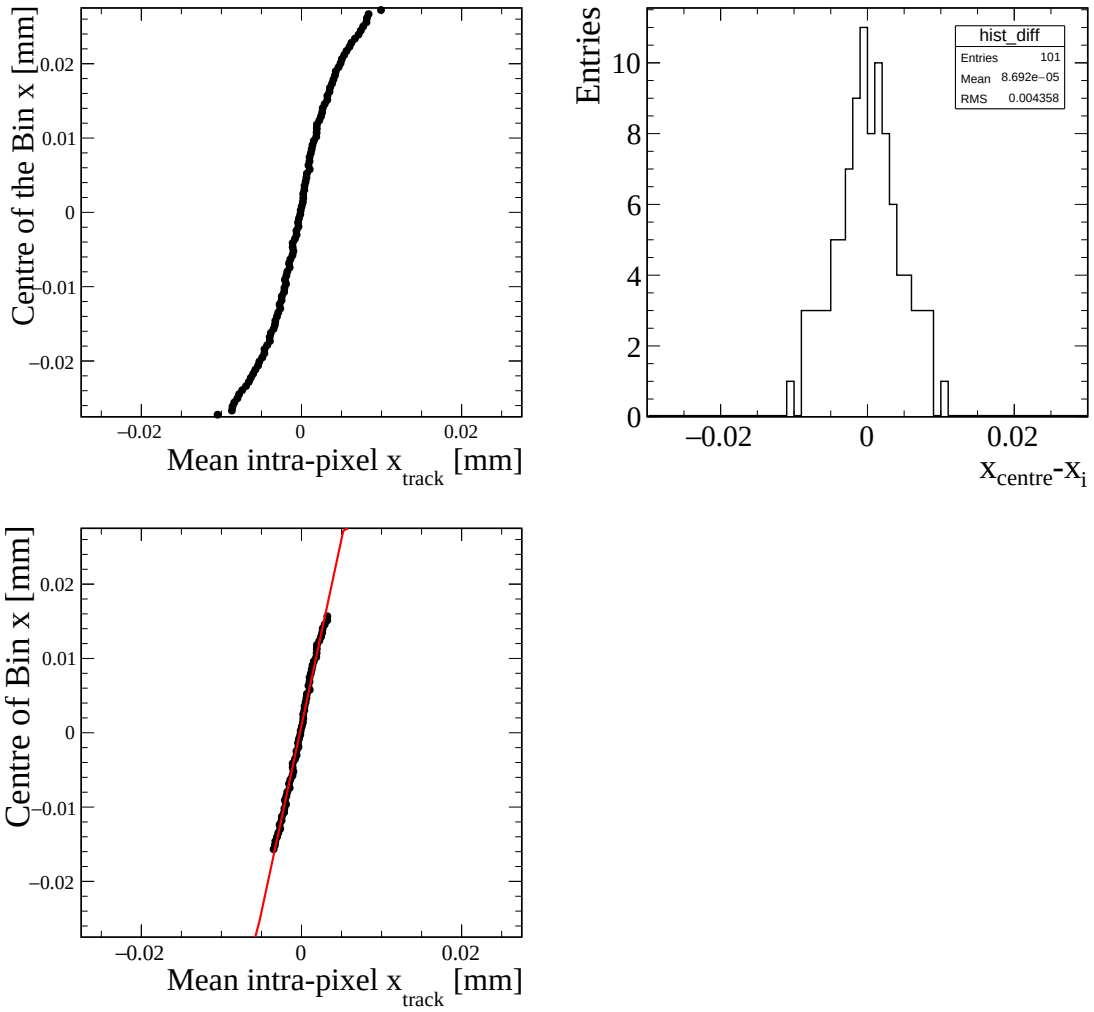


Figure 6.54: An example calibration curve for sensor S25, placed perpendicular to the beam and operated at 40 V (a). The distributions of $x_{centre} - x_i$ (b) and the linear fit to the calibration curve (c).

This procedure was repeated for the calibration curves obtained at each of the voltage and angle steps to extract the gradients. A gradient tending towards 1 identifies when the position reconstructed by the track and the reconstructed hit position reconstruction converge towards the same value. Figure 6.55 (a) shows the variations in the gradient as a function of bias for sensor S25 (Micron n-on-p) and also sensors S8 (HPK n-on-p) and S33 (Micron n-on-n). The trends vary in a similar way to the spatial resolution as a function of bias as expected, see Section 6.3.1. The smallest gradient is measured at the

depletion voltages, when charge sharing is optimal hence the hit position reconstruction is most precise.

Figure 6.55 (b) shows the variations in the gradient as a function of the angle for sensor S8 (HPK n-on-p), S25 (Micron n-on-p) and S30 (Micron n-on-n). These sensors were all tested in July 2015, therefore the gradients can be directly compared. For all sensors the gradients tend towards 1 as the angle increases, as expected. This means for size 2 clusters at large angles, there the non-linear effects are greatly reduced, The gradients measured for S30 are slightly larger because the sensor is 150 µm thick and therefore generates and shares less charge in comparison to a 200 µm thick sensor, at the same angle.

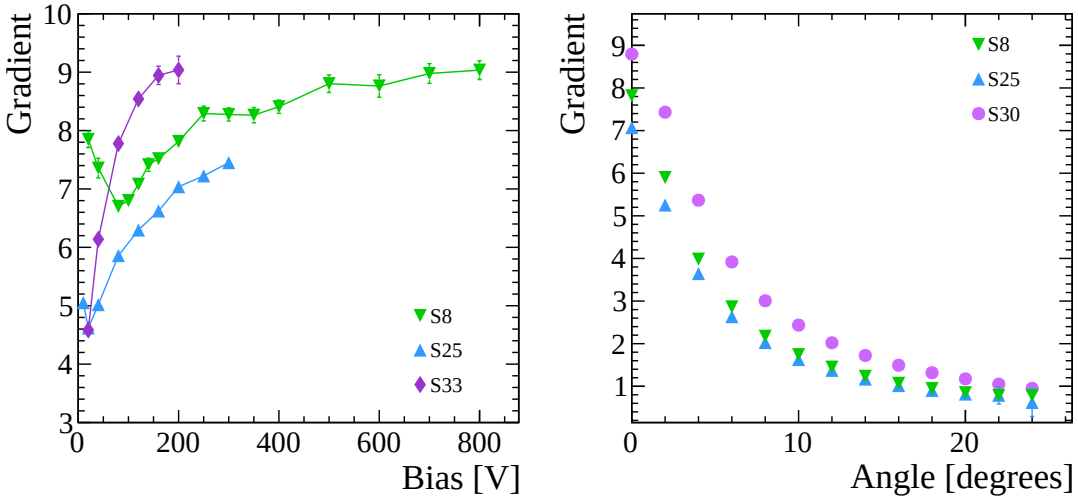


Figure 6.55: The gradient as a function of bias for sensor S25 (Micron n-on-p) and also sensors S8 (HPK n-on-p) and S33 (Micron n-on-n) (a) and the gradient as a function of the angle for sensor S8 (HPK n-on-p), S25 (Micron n-on-p) and S30(Micron n-on-n) (b)

# Chapter 7

# Spatial Resolution Performance of the Irradiated Prototypes

The radiation effects on silicon sensors were previously described in Section 2.3. It was shown that the effective doping concentration of the sensor bulk changes. As a result, a higher bias voltage is required to deplete the sensor. Additionally, the radiation induced trapping centres limit the charge collection, where the probability of trapping decreases with increasing bias. From testbeam analyses presented in Chapter 5, it was shown that the overall charge collection decreased for all irradiated prototypes. The charge collection requirement of a most probable collected charge exceeding $6000e^-$ (outlined in Section 3.3) was reached at $\sim$ 800 V for sensors exposed to the maximum dose of $8 \times 10^{15}$ $1MeVn_{eq}cm^{-2}$. The amount of collected charge did increase with increasing bias, however there was no plateau suggesting that none of the prototypes could reach full depletion before 1000 V. It was also shown that at very high bias, close to 1000 V, the efficiency matches that of non-irradiated sensors; reaching values $\sim$ 99%. However, for much lower voltages the efficiency is greatly reduced in the pixel corners. This is an effect that is greater for pixels with smaller implants. Given these radiation effects, the charge sharing properties of the sensors are expected to change. In this chapter, the spatial resolution for uniformly irradiated sensors is studied for bias and angle scans. Binary and analogue resolutions are compared.

## 7.1 Bias Voltage

The charge sharing behaviour at different bias voltages for a non-irradiated sensor placed perpendicular to the beam was previously discussed in Section 6.3. The bias voltage is directly related to the electric field strength and the drift velocity of the charge carriers. For sensors that are under depleted, the electric field strengths are weaker and the charge collection times are longer. This allows more charge to diffuse to neighbouring pixels. This is also true for irradiated sensors. However due to the reduced charge collection, and the increased probability of charge trapping due to the slow drift velocity, the likelihood of shared charge reaching threshold is greatly reduced. The cluster size distribution for sensor S9 placed perpendicular to the beam and operated at a bias voltage of 100 V is shown in Figure 7.1 (a). S9 was uniformly irradiated to the maximum fluence of $8 \times 10^{15}$ $1\text{MeVn}_{\text{eq}}\text{cm}^{-2}$. Almost all clusters are size 1 at this voltage. The fraction of the different cluster sizes as a function of bias is shown in Figure 7.1 (b). The fraction of size 1 clusters gradually decreases with increasing bias and the fraction of size 2 begins to increase. This behaviour is also seen in a non-irradiated sensor for bias voltages below depletion, shown in Figure 6.26 (a), however the rate of increase of size 2 clusters is much slower for irradiated sensors.

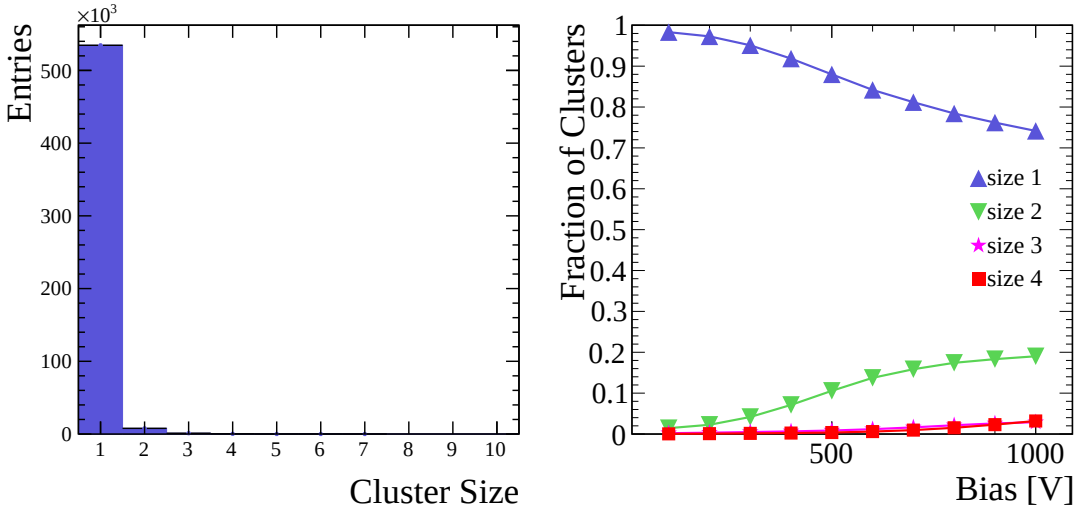


Figure 7.1: The cluster size distribution for a S9 placed perpendicular to the beam operated at 100 V (a). The fraction of clusters as a function of the bias voltage for S9 (b).

It was previously shown in Section 6.1.1 that the magnitude of charge sharing between

pixels is largely dependent on the hit position within a pixel. For charge to be shared between two pixels, the charged particle needs to traverse close to the edge of two pixels. This is still true for irradiated sensors. However, the total charge collected by a pixel needs to be large enough to reach threshold. Figure 7.3 shows the intra-pixel hit positions depending on the cluster size for three different bias voltages. At 100 V the majority of clusters are size 1 and the track hit positions mostly lie in the area within the implant. There are very few entries near the corners of the pixel. This is because of the reduced efficiency at the corner of the pixel for low bias voltages, previously shown in Figure 5.6. The fraction of size 2, 3 and 4 clusters is very small at 100 V and the hit positions are random across the pixel. At 500 V, the fraction of size 2 clusters begins to increase because the charge collection efficiency increases and the efficiency in the corners is recovered (Figure 5.5). The area over which size 1 clusters occur is almost the full pixel area. However, for tracks crossing very close to the edge of the pixel, size 2 clusters do occur. The formation of size 3 and size 4 clusters is evident at the very corners of the pixel, but the occurrence is very low. At 1000 V, the intra-pixel hit positions depending on the cluster size look very similar to those pre-irradiation.

To quantify how much the pixel area width that yields size 1 clusters varies with bias voltage, the projections along of $x_{track}$ along the $x$-axis were compared. Figure 7.3 shows the projections for low bias (a) and for high bias (b). In Figure 7.3 (a), at 100 V there is a steep decrease in the width of the area for which size 1 clusters occur because of the poor efficiency in the corners. As the voltage increases, the efficiency begins to recover and at 300 V, tracks crossing almost anywhere in the pixel result in a size 1 cluster. For voltages above 300 V the area within the pixel for which size 1 clusters occur begins to decrease because the charge collection is more efficient and the the probability of size 2 clusters occurring increases.

### 7.1.1 Analogue Spatial Resolution

Since the spatial resolution performance is highly correlated to the charge sharing properties of the sensor, the spatial resolution is expected to change for irradiated sensors. For non-irradiated sensors, both the analogue and binary spatial resolution followed

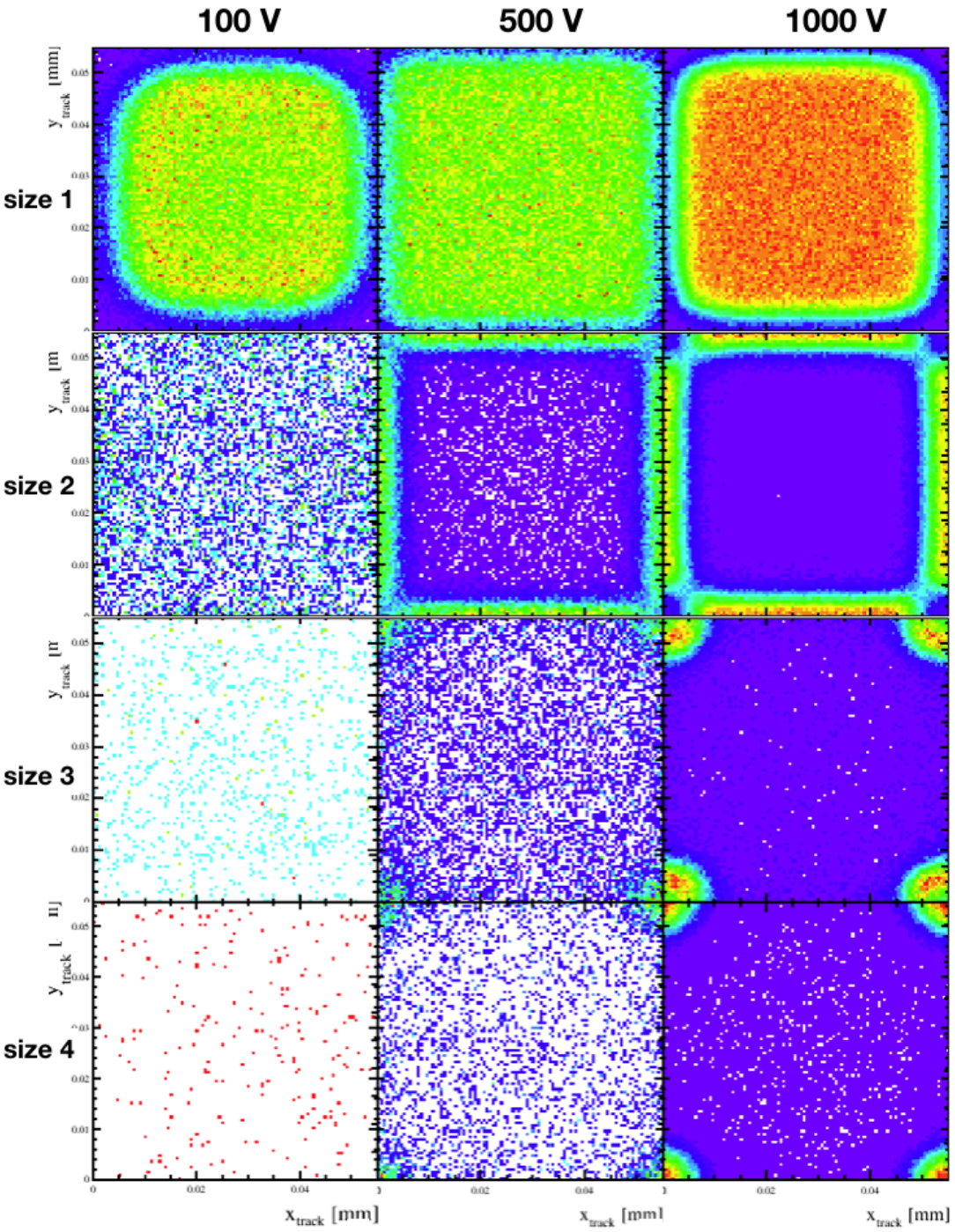


Figure 7.2: The intra-pixel track position depending on the cluster size for three different bias voltages for sensor S9 perpendicular to the beam.

similar trends with varying bias voltage, see Figures 6.35. The resolution gradually improved with increasing bias until the depletion voltage was reached after which the resolution degraded due to over biasing of the sensor. The irradiated sensors do not reach depletion before 1000 V, therefore the resolution is expected to be poor at very low bias and gradually improve with increasing bias. The residual distribution in $x$

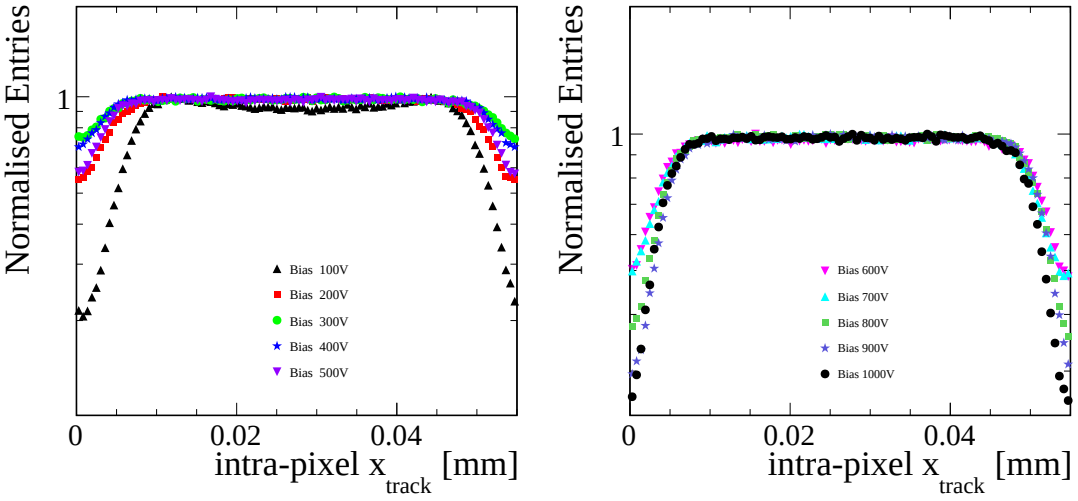


Figure 7.3: The projections of $x_{track}$ for tracks that create size 1 clusters for low bias voltages (a) and high bias voltages (b) for sensor (S9).

for S9 operated at 500 V is shown in Figure 7.4. Due to the large fraction of size 1 clusters the distribution closely resembles the binary "box" like distribution shown for size 1 clusters in Figure 6.10 (a). The residual distributions in $x$ for all voltage steps were fit with a Gaussian. The spatial resolution as a function of bias is shown in Figure 7.5 (a). At first glance, the spatial resolution does not follow the trend expected. The resolution degrades with increasing voltage until 300 V, after which the resolution begins to improve again. This is understood using the projections shown in Figure 7.3. The projections show how the area widths for which size 1 clusters occur. The greatest area at which size 1 clusters occur in a pixel is at 300 V. The position reconstruction of size 1 clusters is binary and is the difference between the centre of the pixel and track position, therefore the largest residual differences occur at 300 V giving the worst spatial resolution. Due to the inefficiencies in the corners at low voltages, the areas at which size 1 clusters occur covers a smaller area of the pixel resulting in a smaller the residual differences. This means that similar values of resolutions can be obtained in comparison to those measured at higher bias voltages. The improvement at bias voltages above 300 V is due to gradual increase in size 2 clusters because the charge collection efficiency increases, improving the probability that shared charge reaches threshold. Even though similar values of spatial resolution can be measured at very low bias, it is not advisable to operate the sensors at these voltages because the charge collection is very small reducing the S/N and the efficiency is poor.

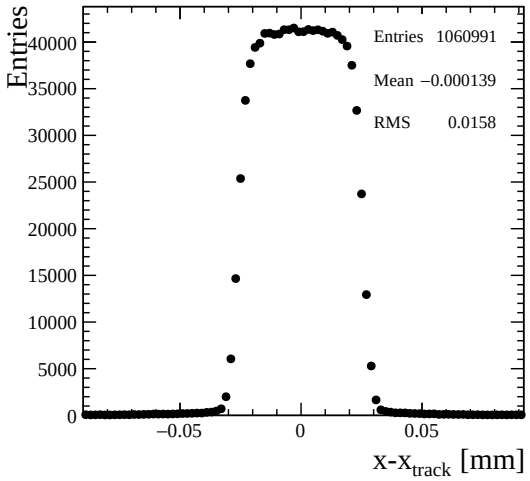


Figure 7.4: The analogue residual difference in $x$ for S9 placed perpendicular to the beam and operated at a bias voltage of 500 V.

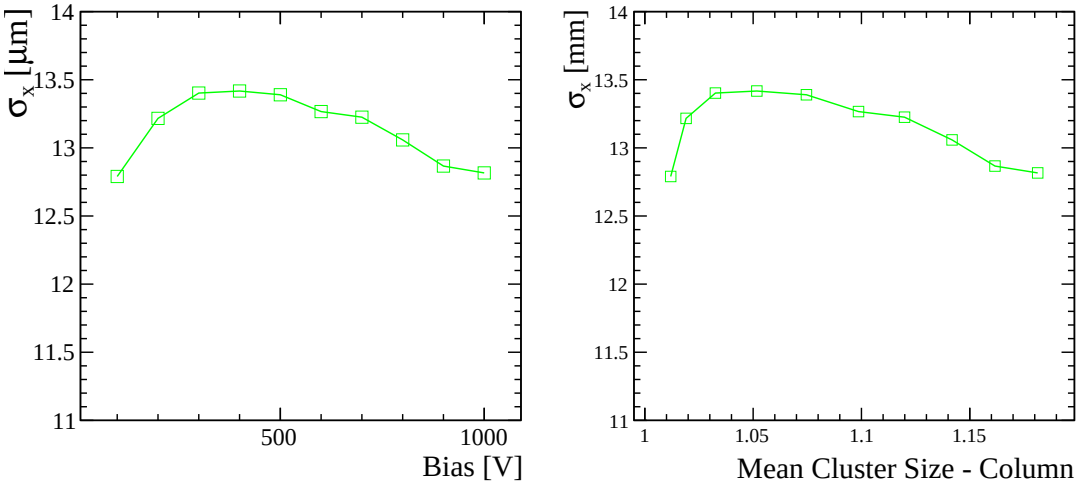


Figure 7.5: The analogue spatial resolution in $x$ as function bias for S9 (a) and the spatial resolution in $x$ depending on the mean cluster size in column (MCSC) (b).

Figure 7.5 (b) shows the spatial resolution as a function of the mean cluster size in column. The trend is distinctively different from the one presented for a non-irradiated sensor shown in Figure 6.34. The spatial resolution degrades with increasing bias between mean cluster sizes 1 to 1.05, after which the spatial resolution improves again. The resolution degrades for mean cluster sizes just slightly greater than one, because size 2 clusters begin to form and the charge on the neighbouring pixel will have charge signals just over threshold. These suffer from poor S/N and non-linear charge sharing. Therefore this effect is understood but the it is not clear the significance of the mean cluster size of 1.05. Therefore, to see if this is a significant mean cluster size, the same

analysis is performed on all of the prototypes tested.

The analogue spatial resolution in $x$ as a function of bias for all uniformly irradiated HPK sensors is shown in Figure 7.6 (a). The sensors were exposed to the maximum fluence of $8 \times 10^{15}$ $1\text{MeVn}_{\text{eq}}\text{cm}^{-2}$. The spatial resolutions for all sensors follows similar trends in comparison to S9. However the magnitudes of resolution vary. These variations are related to slight differences in the experimental circumstance, as previously discussed in Section 6.3.1. The mean cluster size in column as a function of bias voltage is shown in Figure 7.6 (b) for all HPK sensors. The cluster sizes increases with bias, as expected. The spatial resolution as a function of the mean cluster size in column is shown in Figure 7.6 (c). All of the sensors follow similar trends where there is a distinctive peak at mean cluster size $\sim 1.05$.

To compare, the analogue spatial resolution in $x$ as a function of bias for all Micron n-on-p sensors tested is shown in Figure 7.7 (a). The sensors were irradiated to the maximum fluence of $8 \times 10^{15}$ $1\text{MeVn}_{\text{eq}}\text{cm}^{-2}$. The mean cluster size in column as a function of bias is shown in Figure 7.7 (b) and the spatial resolution depending on the mean cluster size in column is shown in Figure 7.7 (c). Generally, the trends observed are similar to those seen in HPK sensors and there are distinctive peaks in Figure 7.7 (c), at a mean cluster size $\sim 1.05$.

### 7.1.2 Binary Spatial Resolution

For non-irradiated prototypes, the binary resolution as a function of bias was better than that of analogue. This was because of the non-linear charge sharing feature that influences the analogue position reconstruction. Non-linear charge sharing was found to mostly affect asymmetric charge sharing. For the irradiated sensors, the fraction of size 2 clusters is smaller and the magnitude of charge on each cluster is also small due to the reduced charge collection. Therefore the non-linear feature is still expected to degrade analogue spatial resolution, meaning that post irradiation the binary resolution is likely to be better. The analogue and binary resolution in $x$ as a function of bias are compared in Figure 7.8. At low bias, the binary (red) and the analogue (black) resolutions are similar because size 1 clusters dominate. After 300 V the difference between the

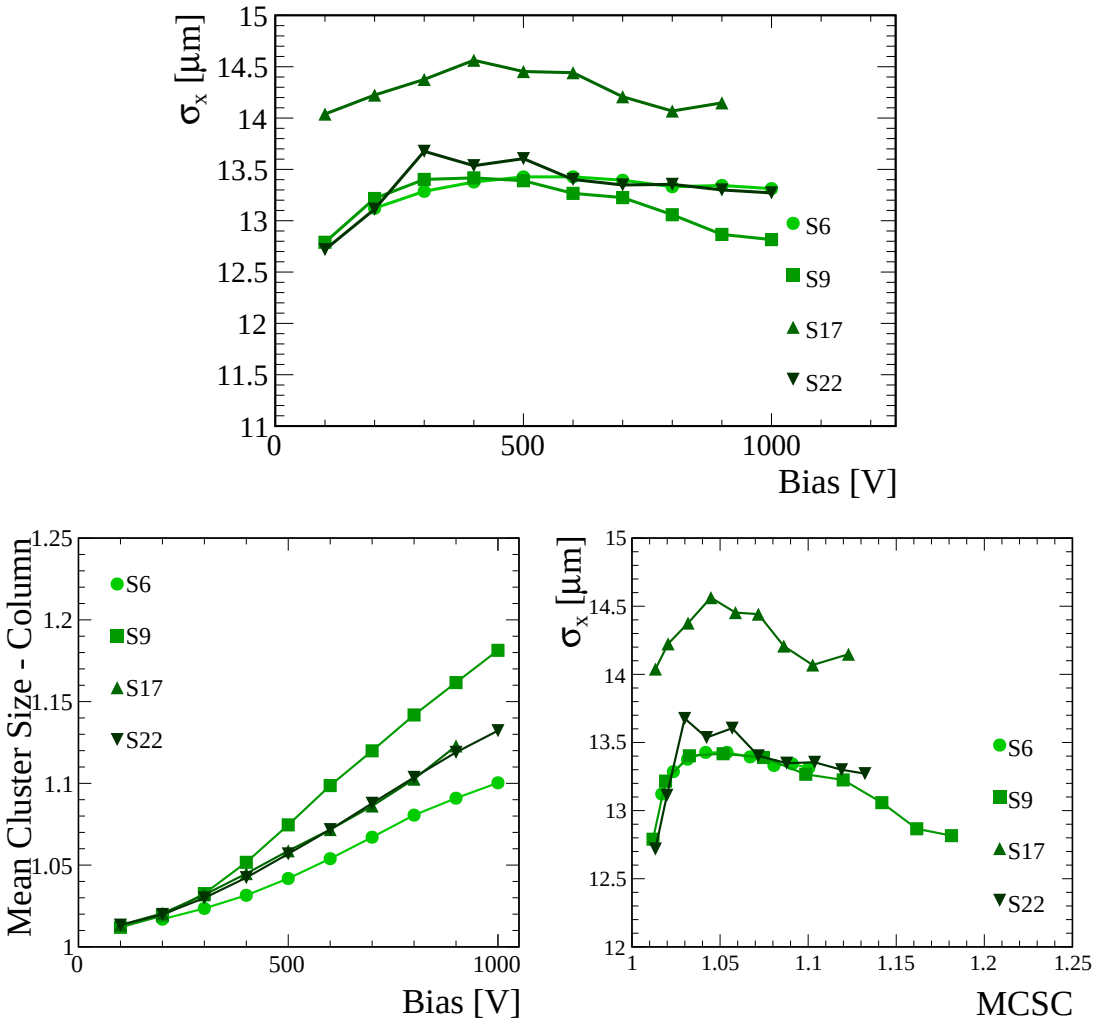


Figure 7.6: The analogue spatial resolution in $x$ as function bias for all HPK prototypes tested (a). The mean cluster size in column as a function of bias (b) and the analogue spatial resolution in $x$ depending on the mean cluster size in column (c) for all HPK prototypes tested.

binary and analogue resolution gradually increases due to the non-linear charge sharing experienced by the analogue position reconstruction. Figures 7.9 (a) and (b) are the residual distributions for size 2 clusters at 1000 V for analogue and binary, respectively. In the analogue distribution, the residual difference is noticeably wider and double peak feature previously discussed in Section 6.2.1 is a dominated feature of the residual. The binary residual is much narrower, and hence the overall resolution is better.

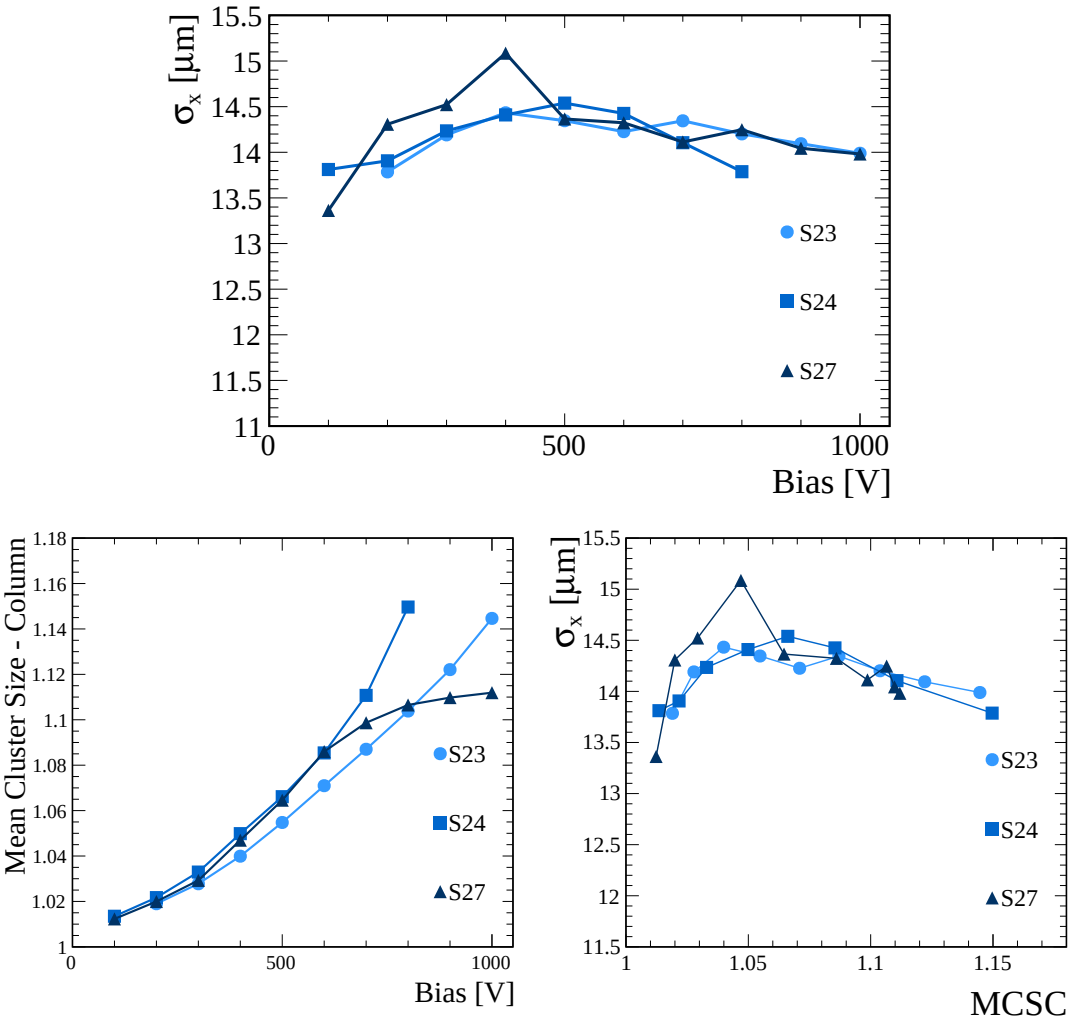


Figure 7.7: The analogue spatial resolution in $x$ as function bias for all Micron n-on-p prototypes tested (a). The mean cluster size in column as a function of bias (b) and the analogue spatial resolution in $x$ depending on the mean cluster size in column (c) for all Micron n-on-p prototypes tested.

## 7.2 Track Angle

It was shown in Section 6.4 that the path length of a particle though the sensor bulk is larger for tracks at an angle. Thus more charge is generated and more pixels are traversed. A more precise position is reconstructed for particles that share charge with more than one pixel, therefore the spatial resolution improves with angle. For pre-irradiated sensors the best analogue spatial resolution was at an angle where the fraction of size 2 clusters was greatest (Section 6.4.1). The best binary resolution occurred when the fraction of size 1 and size 2 clusters was roughly equal and the hit locations within a pixel at which size 1 and size 2 clusters occurred was divided equally (Section 6.4.2).

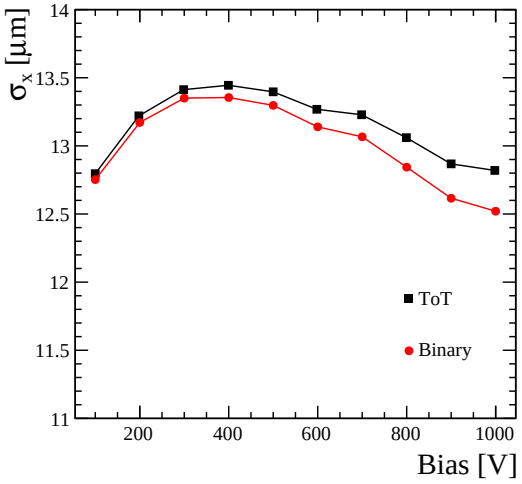


Figure 7.8: The comparison of binary and analogue spatial resolution in $x$ for uniformly irradiated S9.

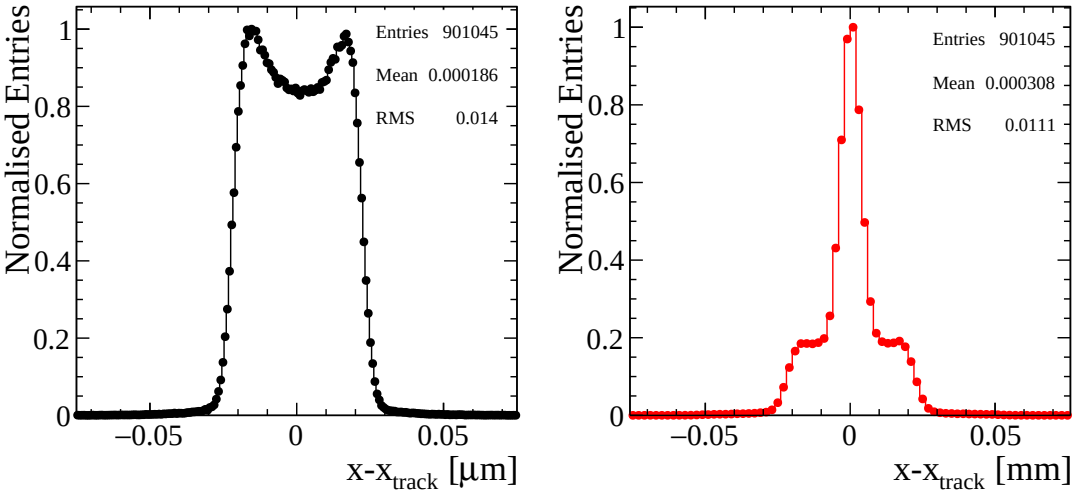


Figure 7.9: The analogue residual distribution (a) and the binary residual distribution (b) for size 2 clusters in $x$ for uniformly irradiated S9.

Similar scenarios are expected post irradiation, however the angles at which the best resolution occurs will change. This is because of the altered depletion voltages and reduced diffusion. When sensors are operated below depletion, the sensor is effectively thinner.

Figure 7.10 shows the fraction of the different cluster sizes as a function of angle. The fraction of size 2 clusters gradually increases with angle however it does not peak before 24°. This therefore suggests that there will be no minimum in the analogue resolution within the angle range measured. The fraction of size 1 and size 2 clusters is roughly

equal around ~ 18°. Given the analysis presented in Section 6.4.2, the optimum binary resolution is therefore expected at angles slightly larger than ~ 18°.

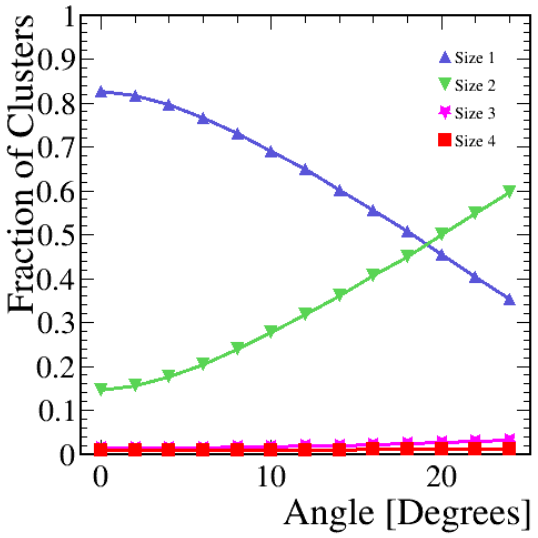


Figure 7.10: The fraction of the different cluster sizes depending on the track angle for sensor S23.

The analogue spatial resolution in $x$ as a function of angle is shown in Figure 7.11. The sensors were uniformly irradiated to the maximum dose of $8 \times 10^{15}$ $1\text{MeVn}_{\text{eq}}\text{cm}^{-2}$. For all sensors the resolution improves as a function of angle varying from ~ 13 µm at 0° to ~ 8 µm at 24°. The binary spatial resolution in $x$ as a function of angle is shown in Figure 7.12. The resolution improves as a function of angle until a minimum is reached and then the resolution degrades again. The angle at which this happens varies depending on the sensor and ranges between $15 - 20°$. The poorest resolution are ~ 13 µm measured at 0° and the best resolutions measured are ~ 10 µm, which is a couple of microns worse than best resolutions measured using analogue readout.

The analogue and binary spatial resolutions in $x$ as a function of angle are compared for sensor S23 shown in Figure 7.13. At smaller angles the binary resolution is better than the analogue resolution due to the non-linear effects degrading the analogue position reconstruction. However after 18° the binary resolution begins to degrade and the analogue resolution continues to improve. The reason for the decline in the binary resolution at high angles is because of the increase in the fraction of size 2 clusters, previously described in Section 6.4.2.

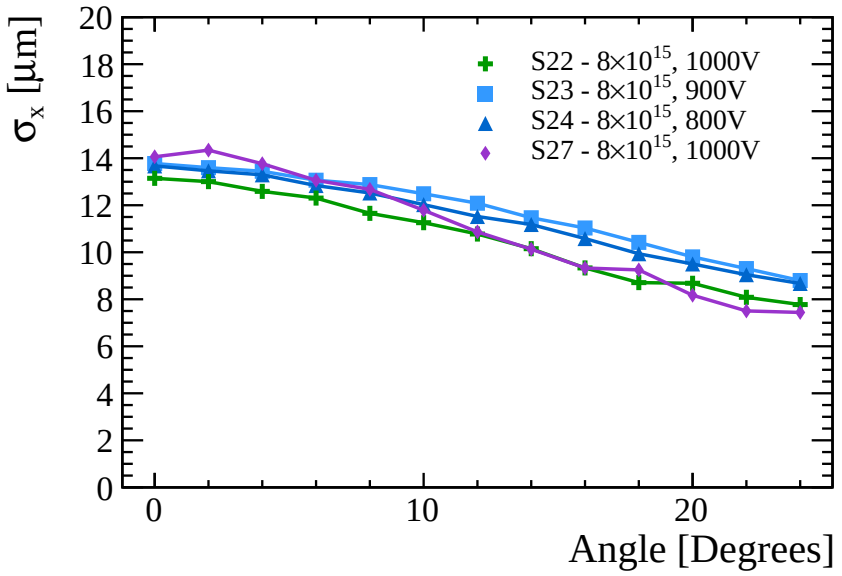


Figure 7.11: The analogue spatial resolution in $x$ as a function of angle for sensors uniformly irradiated to the maximum fluence.

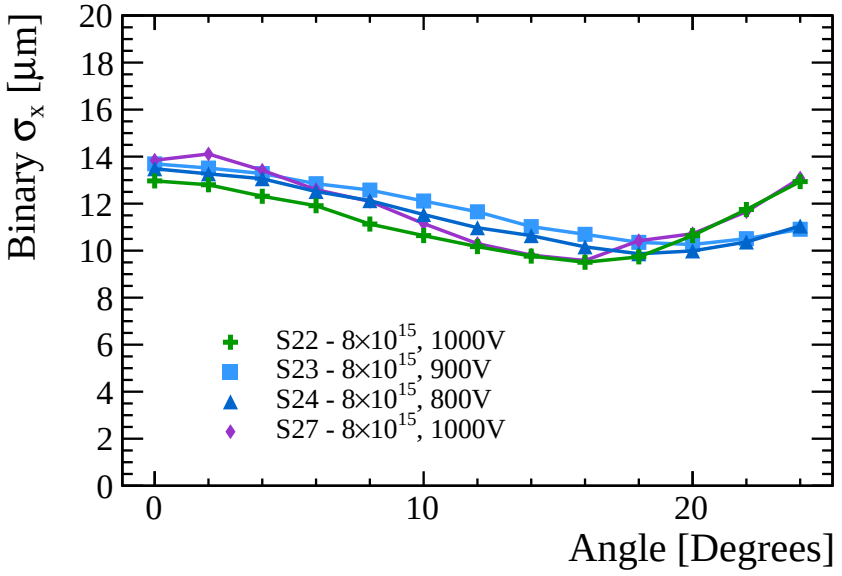


Figure 7.12: The binary spatial resolution in $x$ as a function of angle for sensors uniformly irradiated to the maximum fluence.

As previously mentioned, if a sensor is not fully depleted the effective thickness of the sensor is smaller. If only a very small fraction of the sensor is depleted, even if a track traverses at a large angle, all of the charge collected in the traversed pixels may not reach threshold. Figure 7.14 (a) shows the analogue spatial resolution in $x$ as a function of angle for 4 different bias voltages for irradiated sensor S23. The corresponding mean cluster sizes in column are shown in Figure 7.14 (b). At very low bias, the resolution is

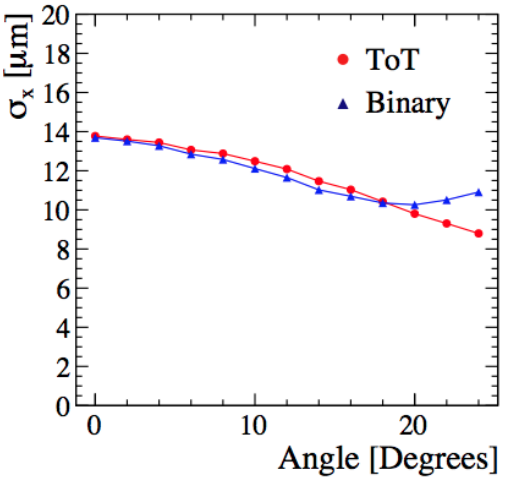


Figure 7.13: The comparison of the binary and analogue in $x$ as a function of angle for irradiated sensors S23.

mostly constant for all angles. This is because the mean cluster size does not vary with angle and is very close to 1. As the angle scans are performed using higher bias voltages, there are improvements in the spatial resolution at higher angles. The best resolutions overall are measured when the sensor is operated at the highest bias voltage (1000 V). At this voltage, the depletion width is largest and the charge collection is higher.

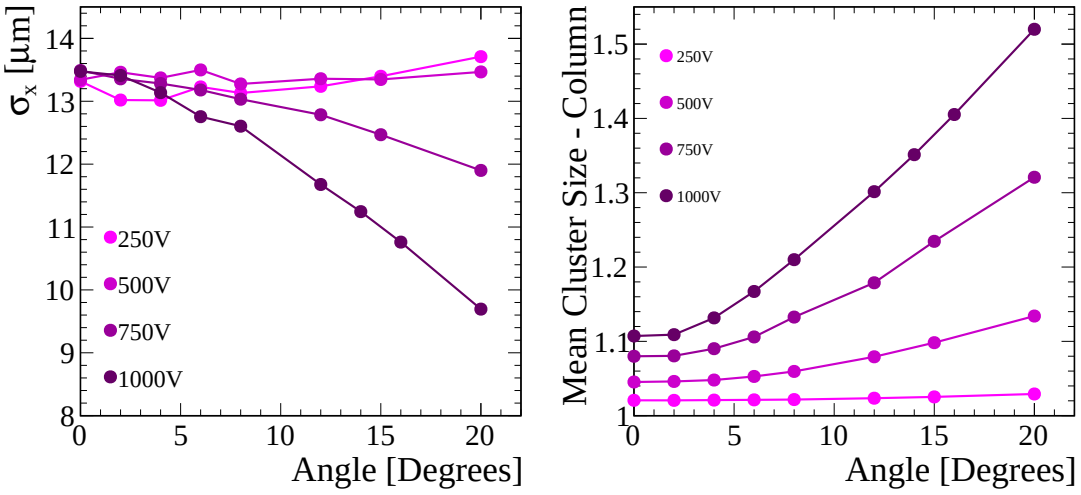


Figure 7.14: The analogue resolution in $x$ as a function of angle measured for four different bias voltages (a) and the corresponding mean cluster size in column (b). The sensor (S6) was uniformly irradiated to the full fluence.

## 7.3 Summary

Radiation damage leads to a reduced performance in the spatial resolution for all prototypes sensors. An increased bias voltage increases the charge collection efficiency, improving both the binary and analogue resolutions. For perpendicular tracks the binary resolution is generally better than the analogue resolution due to the non-linear charge sharing effects degrading the analogue resolution. The worst resolution was not necessarily measured at the lowest voltage. At very low voltage, the low efficiency in the corners of the pixels resulted in an improved the resolution. With increasing bias voltages, the resolution degraded before improving again. The worst resolution for all sensors occurs at a mean cluster size of $\sim 1.05$.

Both the analogue and binary resolutions improved as the track angle increased due to the larger charge collection for tracks traversing at angles. For low angles, the binary and analogue resolutions were roughly the same with the binary resolution being slightly better except at very large angles.

# Chapter 8

# Conclusions

The LHCb VELO detector will be upgraded during Long Shutdown 2 (LS2) of the LHC, beginning in 2019. The upgrade will allow for the detector to operate at higher luminosities. A key change to the VELO is the replacement of the silicon strip sensors with hybrid pixels sensors. The hybrid pixel sensors consist of two parts, a planar silicon sensor and a VeloPix readout ASIC. The VeloPix ASIC has a binary readout to cope with the increased data rates foreseen at higher luminosities. The silicon sensor design is the discussion of this thesis. The baseline design for the sensors was a 200 µm thick sensor with a p-bulk and n-type implants and guard rings size of 450 µm or less. Sensor prototypes were provided by two manufactures with different bulk types, thickness, implant sizes and guard ring designs. Over several years these prototypes were tested in a laboratory and at the SPS testbeam facility using the TimePix3 Telescope. The purpose of the tests was to determine which prototype design best fit the performance requirements outlined in the Technical Design Report (TDR) [5]. A fundamental requirement of the sensors is that they are radiation tolerant, thus the majority of the requirements given are for the performance post-irradiation. To summarize, the requirements are:

- The sensors must yield a most probable signal exceeding $6000e^{-}$, at a voltage less than 1000 V without breakdown, after exposure to a maximum fluence of $8 \times 10^{15}$ $1MeVn_{eq}cm^{-2}$
- A uniform charge collection efficiency >99% is required before and after irradiation

- A spatial resolution comparable to the current VELO

During the testing campaign, the VeloPix was still under design, therefore its predecessor the TimePix3 ASIC was used to test the prototypes. The TimePix3 ASIC has an analogue readout, making it an excellent ASIC for prototype testing because it provides charge information. This is crucial in determining whether the sensors are able to meet all of the requirements stated above.

In the laboratory, the IV tolerance of the prototypes was tested. It was found that all of the different prototypes exposed to the maximum radiation dose were able to reach 1000 V without breakdown. In addition, threshold equalisation of the TimePix3 ASIC was performed to correct for local offsets in the threshold and a charge calibration was also performed to convert the ToT counts measured by the ASIC to electrons.

The rest of the performance criteria were tested using the TimePix3 telescope. It was found that all of the prototypes yielded a most probable signal exceeding $6000e^-$ post irradiation at bias voltages $\sim$ 800 V. The required efficiency was achieved at very low voltages pre-irradiation, but required large bias voltages close to 1000 V to recover the efficiencies post-irradiation. For lower voltages, the efficiencies in the corners were found to degrade, an effect that was enhanced for pixels with smaller implants.

The spatial resolution is the measure of accuracy with which the hit position of a particle is reconstructed and is defined as the width of the distribution of the difference between the position predicted by a track and the hit position reconstructed using the sensor. The track positions were provided by the TimePix3 telscope, which was found to have a pointing resolution of $1.69 \pm 0.16$ µm in $x$ and $1.55 \pm 0.16$ µm in $y$ at the very centre between two telescope arms. The reconstructed position was reconstructed using both the Centre Of Gravity algorithm using the charge information to measure the analogue resolution and the binary reconstruction algorithm to measure the binary resolution. Both resolutions were measured as a comparison and to determine if the binary resolution matched the expectations from simulations presented in the TDR.

The expectation was that the analogue resolution would be better, however due to non-linear charge sharing influencing the analogue position reconstruction, the majority of

time the binary resolution was found to be better both before and after irradiation. The Centre of Gravity algorithm assumes linear charge sharing between pixels and therefore requires a non-linear correction to correct for the sensor effects. One method of correcting the non-linear feature was introduced but due to only small improvements it was deemed impractical (Section 6.2.2). Given more time, and if an alternative non-linear correction is realised, the analogue spatial resolution should always perform better than a binary resolution.

The precision at which the position of a particle can be reconstructed was found to be highly dependent on the magnitude of charge generation and sharing within a sensor. Pre-irradiation it was found that the 200 μm thick sensors had a better resolution in comparison to the 150 μm, due to the larger charge generation. Furthermore, theoretically a smaller implant size increases the probability that charge will be shared between pixels and therefore a better position resolution is expected. However, no significant difference in position resolution was observed between the smallest implant size, 35 μm, and the largest, 39 μm, in data. For irradiated sensors it was found that there was no dependence on the thickness and all prototypes showed the same response in terms of the charge collection. The smaller implant size reduced efficiency in the corners at lower bias, inadvertently this actually improved the spatial resolution. However, it is not advisable to operate the sensors at these voltages due to the smaller S/N and the poor efficiency.

All of the results discussed above, suggest that for a sensor optimised for spatial resolution, the best sensor design is a 200 μm thick, n-on-p sensor with the smallest implant available, 35 μm. However this only holds true for pre-irradiated sensors, therefore due to the reduced efficiency in the corners for irradiated sensors, a larger implant is best.

The performance of the different guard ring designs was studied and it was found that the Micron n-on-p and n-on-n guard ring designs did not perform as they should. Unfortunately, due to time constraints, Micron were not able to produce new prototypes with improved guard ring designs and thus the Micron sensors will no longer be considered for the final design choice of the VELO. Hence, the best design choice for a sensor optimised for spatial resolution is a HPK n-on-p 200 μm thick sensor with an implant

size of 39 μm. In the end, this was the final design choice for the VELO upgrade sensors, with the addition of the guard ring size of 450 μm.

If there were no issues with the guard ring designs, the micron n-on-p sensors would be the better choice because pre-irradiation they have a lower depletion voltage in comparison to the HPK. Or if the n-on-n sensors and their "edgeless" guard ring design could have been made with a thickness of 200 μm they could have been better choice for the VELO.

The best pre-irradiation binary resolution measured by a HPK sensors was $\sim 12$ μm for a sensor perpendicular to the beam operated at the depletion voltage. The same measurement post irradiation yielded a binary resolution of $\sim 10$ μm, though full depletion was never reached. For tracks at angles, the best binary resolution was $\sim 9$ μm measured at 10° pre irradiation and $\sim 10$ μm measured at ~18°.

The current VELO uses silicon strip sensors that have different strip pitches depending on the proximity to the beamline and the readout is analogue. The spatial resolution of the current VELO varies between $\sim 4.3 - 18$ μm depending on the strip pitch and track angle. Therefore, the VELO upgrade sensors and the move to binary readout will result in a poorer spatial resolution. However, the impact parameter resolution is still improved under upgrade conditions because of the reduced material budget and distance to the first measured point.

In theory, one other way to further improve the spatial resolution while still using the same thickness of detector is to tilt the VELO modules at an angle relative to the beamline. This would increase the charge generation and increase the cluster sizes, therefore improving the spatial resolution. The mechanical infrastructure of VELO currently does not allow this. The material budget that a track traverses would also increase, possibly degrading the impact parameter resolution.

The VELO module production is now under way, in preparation for the installation to of the new VELO to be installed starting from 2019.

# Appendix A

# Pointing Resolution

The pointing resolution defines the precision with which the hit position of a particle can be reconstructed. The pointing resolution is not constant along the track and is dependent on the intrinsic resolution of the telescope sensors, the number of sensors in the telescope, their thickness and their relative $z$ positions. The method of measuring the pointing resolution was previously described in Section 4.2.4.

Figure A.1 shows the pointing resolution for the $y$-coordinate as a function of the $z$-direction. The biased resolution from data is compared to simulation. The pointing resolution varies depending on the $z$ position where the best achievable pointing resolution is found at the centre of the telescope where $\sigma_y = 1.55 \pm 0.16$ µm. This is slightly better than the pointing resolution measured for the $x$-coordinate measured to be $\sigma_x = 1.69 \pm 0.16$ µm. This is likely due to variations in the mean cluster size in columns in comparison to the mean cluster size in rows, due to possible slight misalignments in the angular rotations.

The single hit resolution for each telescope plane can vary due to differences in ASIC thresholds and incident angle relative to the beam. For sensors that have a lower threshold relative to the rest, the charge collection can be larger and spread over more pixels increasing the cluster size. For sensors placed at a slightly larger angles than the rest, the charged particle generates more charge and traverse more pixels, again increasing the cluster size. The cluster size contributes to the precision at which the sensor hit position can be reconstructed, therefore leading to variations in the spatial resolution. Figure A.2 shows the biased resolutions from data, compared to the mean cluster size in column, for each of the telescope planes. Generally, a larger cluster size results in a better spatial resolution, which is the behaviour observed in Figure A.2.

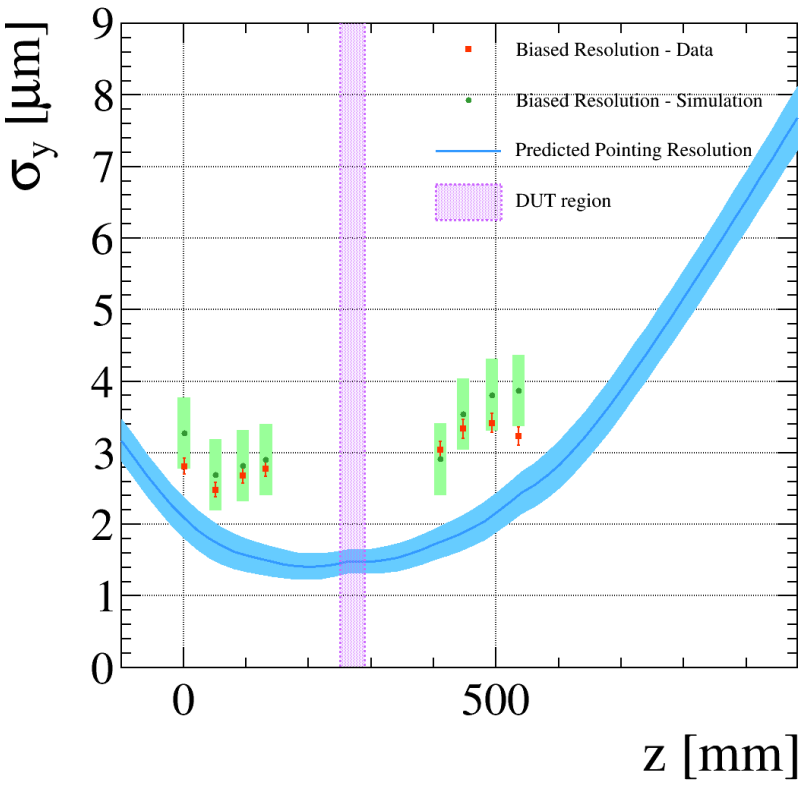


Figure A.1: The pointing resolution for the $x$-coordinate as a function of the $z$-position. The best achievable pointing resolution is found at the centre of the telescope and $\sigma_y = 1.55 \pm 0.16$ µm.

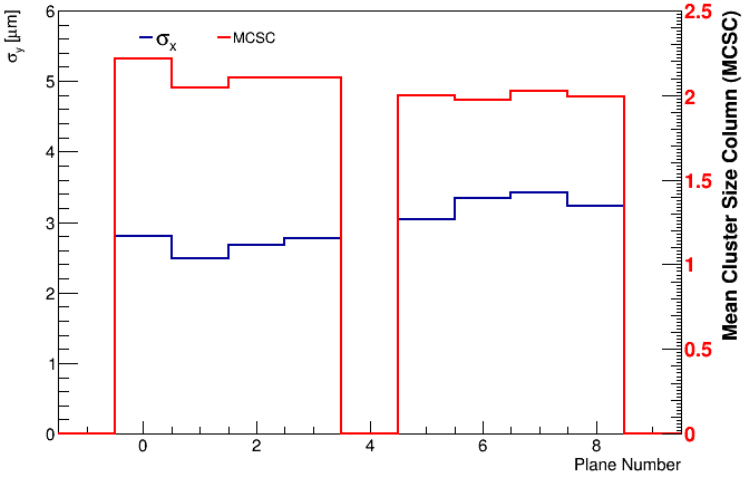


Figure A.2: The biased resolution in $y$ and the mean cluster size in rows (MCSR) for each of the telescope planes.

# Appendix B

# Intra-Pixel Residuals

In Section 6.2.1, the analogue spatial resolution was measured for a sensor perpendicular to the beam, operated at a bias voltage around depletion. The residual distribution in $x$ for all cluster sizes had a distinctive double peak feature, see Figure 6.8. The feature was found to be due to non-linear charge sharing between pixels. Since non-linear charge sharing does not effect size 1 clusters and the fraction of size 3 and size 4 clusters is small for perpendicular tracks, the non-linear feature was studied in detail in Section 6.2.1 for size 2 clusters only. One of the main methods of understanding non-linear feature was to plot the residual distributions depending on the intra-pixel hit positions within one pixel for the different cluster sizes. This was done by splitting the pixel into a $5 \times 5$ grid, as illustrated in Figure B.1. The sensor studied (S25) has an implant size 36 µm, meaning that the implant impinges a distance of 1.5 µm into the periphery bins. As a comparison, the residual differences in $x$ as a function of the intra-pixel track position depending on cluster size 1, 3 and 4 will be presented here.

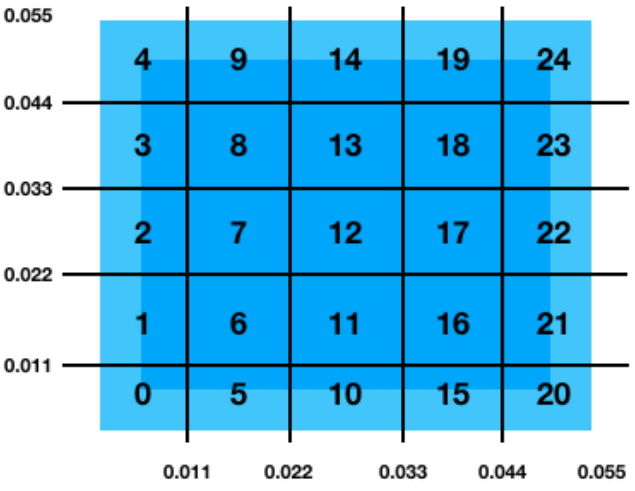


Figure B.1: Illustration of the division of a single pixel into a $5 \times 5$ grid.

For size 1, the analogue residual differences in $x$ depending on the intra-pixel track positions within the intra-pixel grid is shown in Figure B.2. The majority of tracks that result in a size 1 cluster travel through the centre of the pixel, around the area of the implant. This is reflected in the plot, where the majority of entries are in the central bins (6,7,8,11,12,13,16,17,18). Within these bins the residual distributions are box like, as expected for binary reconstruction. However, the very edges of the residuals in the periphery bins, show Gaussian like tails due the diffusion, as previously described for Figure 6.10 (a).

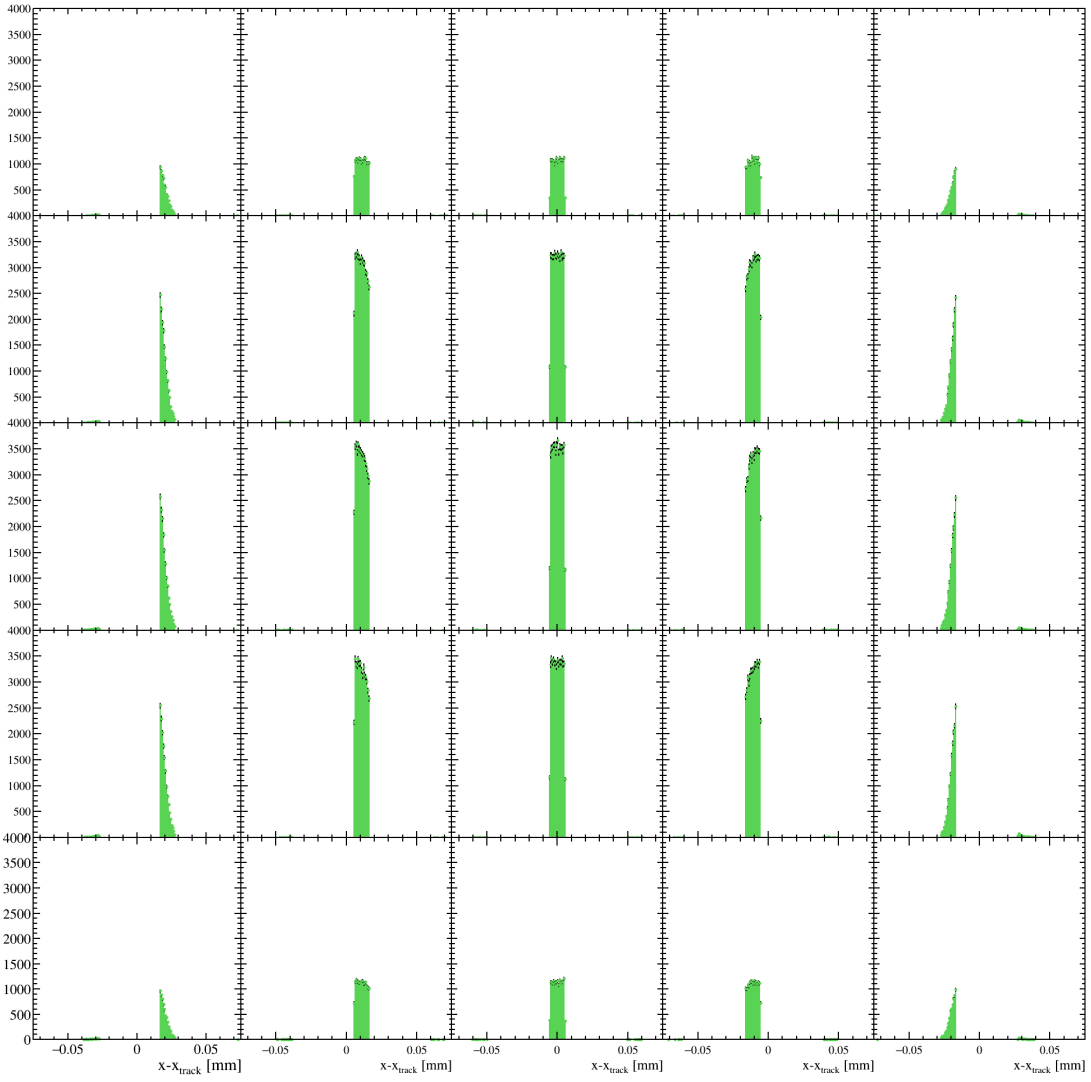


Figure B.2: The analogue resolution for size 1 clusters depending on the intra-pixel tracks positions within the grid illustrated in Figure B.1.

For size 3 and 4 clusters, the analogue residual differences in $x$ depending on the intra-pixel track positions within the intra-pixel grid are shown in Figures B.3 and B.4, respectively. The majority of tracks that result in a size 3 and 4 clusters traverse through the very corners of the pixels. Hence, the residual distributions are found within the very corner bins (0,4,20,24). The distributions are asymmetric in shape, with a peak

off centres, the same behaviour as seen for size 2 clusters. This suggests that analogue position reconstruction for size 3 and size 4 is also influenced by non-linear charge sharing. This is expected because the magnitude of charge measured in the neighbouring pixels is small. However, since the fraction of size 3 and size 4 clusters is small, there contributions and influences on the residual distribution for all cluster sizes is minimal.

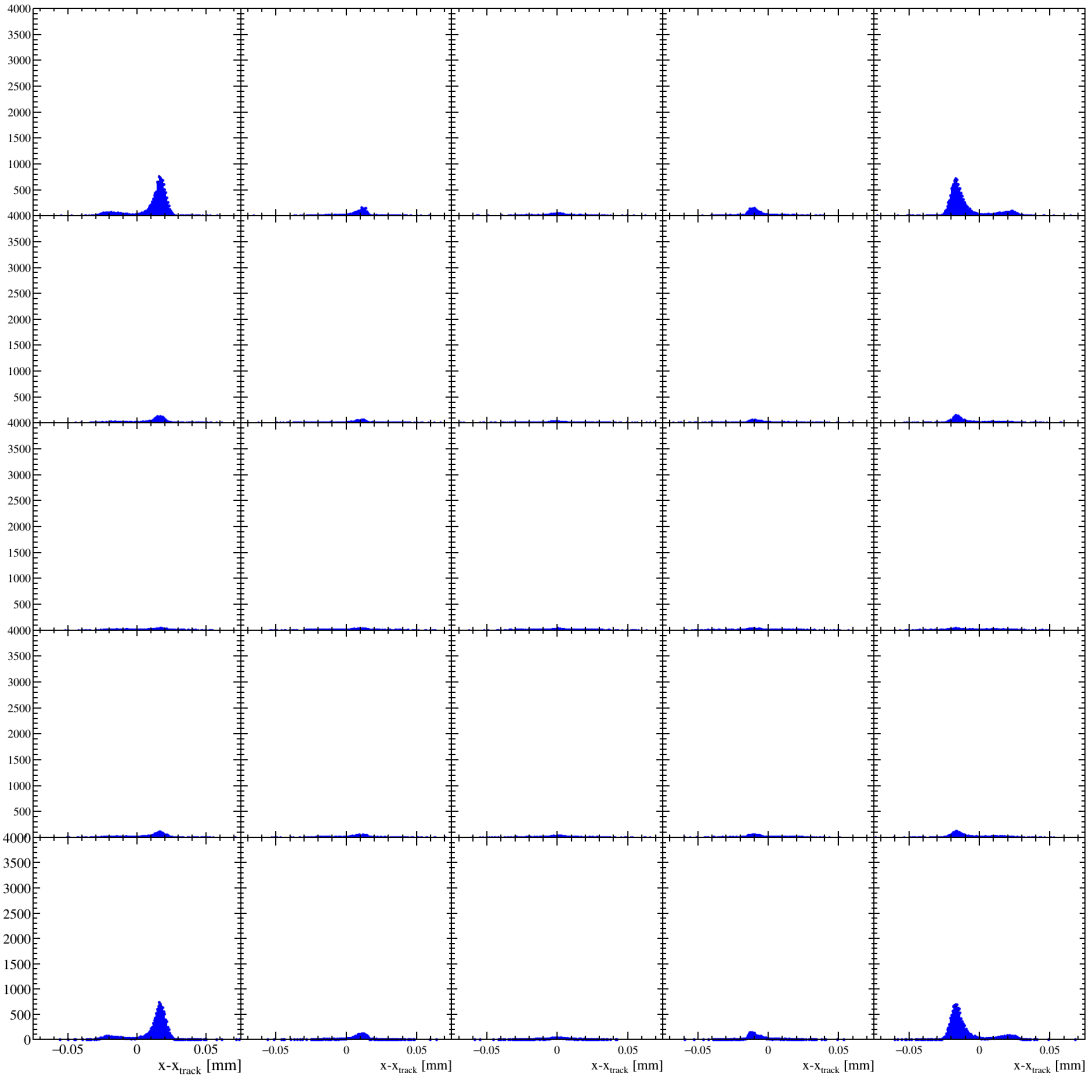


Figure B.3: The analogue resolution for size 3 clusters depending on the intra-pixel tracks positions within the grid illustrated in Figure B.1.

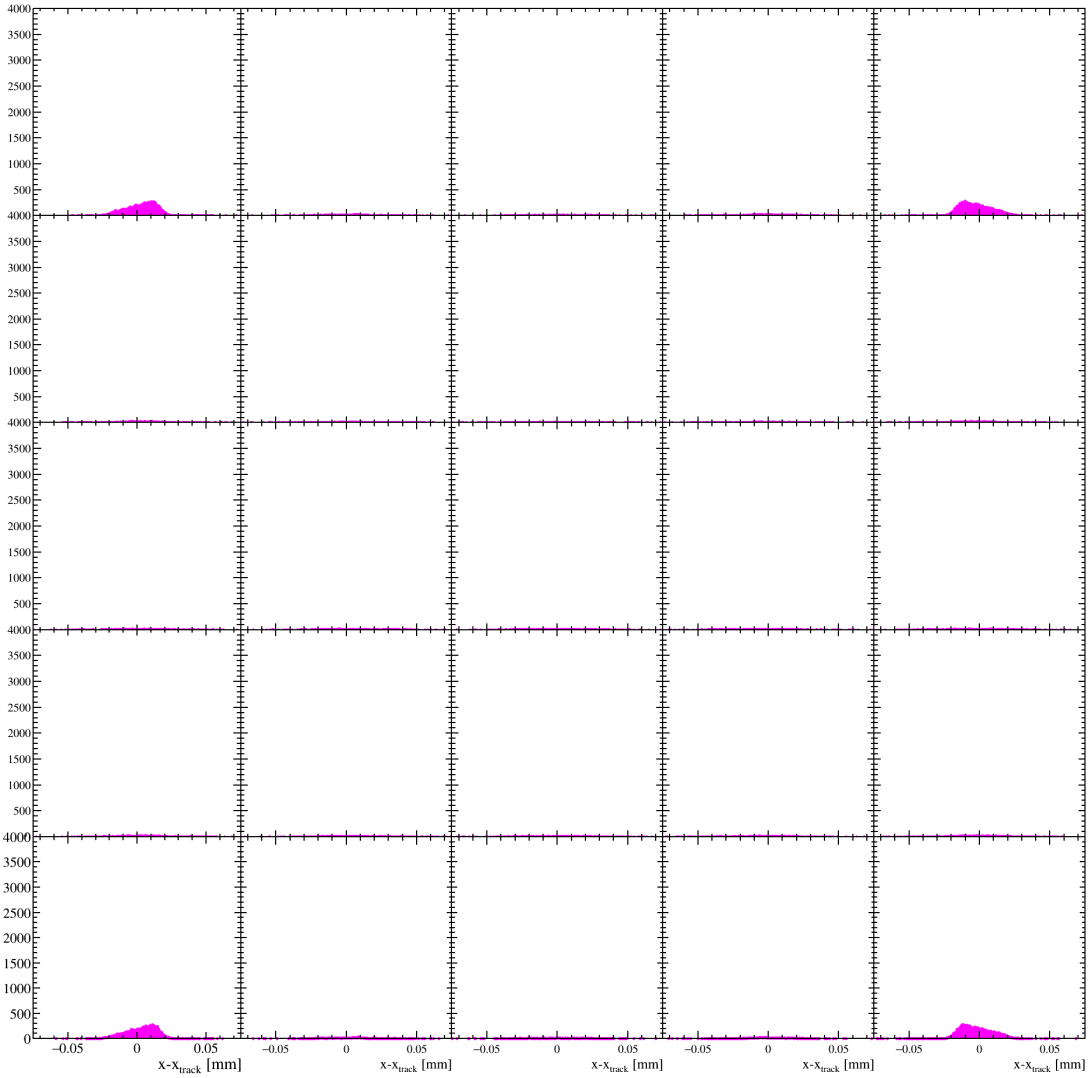


Figure B.4: The analogue resolution for size 4 clusters depending on the intra-pixel tracks positions within the grid illustrated in Figure B.1.

# Appendix C

# Telescope Residual Comparisons

It was previously shown in Section 6.3.1, that sensors of identical type (same manufacturer, type, thickness and implant size) showed variations in the order of ~ 1 μm in the measured spatial resolution. The mean cluster sizes were seen to be very similar, suggesting that the differences in spatial resolution stem from the reconstructed track positions. The tracking performance can vary between different testbeam months due to experimental circumstances: for example, variations in the $z$ positions or angular rotations of the planes, temperature variations, threshold settings and changes to the depletion voltage of the sensors. The TimePix3 telescope has been in operation at the SPS testbeams since 2014, and has been redeployed several times.

During a testbeam in August 2017, bias and threshold scans were performed on the telescope. Typically the telescope was operated at a bias voltage of 100 V or 150 V. Both voltages are above the depletion voltage of the telescope sensors. The unbiased spatial resolution ($\sigma_x$) in $x$ for each of the telescope planes is shown as a function of the bias voltage in Figure C.1 (a). The resolution improves with increasing bias for all telescope planes until ~ 70 V, after which the resolution begins to plateau. This behaviour is similar to that seen in Section 6.3.1, where the resolution is generally worse at bias voltages below full depletion[1]. To quantify the change in resolution as a function of the bias voltage, the ratio $\sigma_x[i]/\sigma_x[150\text{V}]$ where $i$ is each voltage step, was measure and is shown in Figure C.1 (b). Different bias voltages between 100 V and 150 V yield a difference in the resolution of up to ~0.2 μm.

During normal telescope operations, the threshold of each TimePix3 ASIC is set to 1000$e^-$ to ensure that the threshold is well above the noise, previously discussed in Section 4.1.3. Decreasing the threshold results in more charge signals reaching the threshold, meaning that the cluster sizes increase. This is shown in Figure C.2 (a), where the mean

[1]Note that the two analyses cannot be directly compared because the telescope planes are tiled at an angle of 9° with respect to the beam and the sensors tested in Section 6.3.1 were studied for sensors perpendicular to the beam.

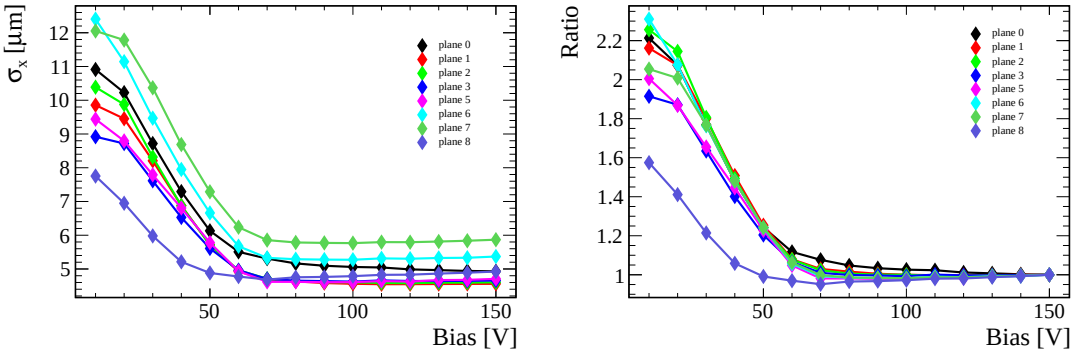


Figure C.1: The unbiased spatial resolution in $x$ for each of the telescope planes as a function of the bias voltage (a). The threshold of each of the telescope ASICs was set to 1000e$^-$. The ratio ($\sigma_x[i]/\sigma_x[150\text{V}]$) as a function of the bias voltage for all telescope planes (b).

cluster size in column is plotted as a function of the threshold. As the threshold is decreased the mean cluster size increases. Therefore, the spatial resolution also improves with decreasing thresholds, as shown in Figure C.2 (b). The reduced threshold may result in an improved resolution but the number of noisy pixels and hence data rate increases dramatically making operations of the telescope more challenging. To quantify the change in resolution as a function of the threshold, the ratio $\sigma_x[i]/\sigma_x[1000\text{e}^-]$ where $i$ is each threshold step, was measured and is shown in Figure C.2 (c). These results show that the difference in resolution over the threshold range is in the order of $\sim 0.5$ μm.

In addition to possible variations in bias voltage and threshold settings between different testbeam campaigns, it is not certain that all telescope planes are placed back exactly at the same locations. In principle, the $z$ positions of the detectors can be extracted from the alignment fit. However, as the tracks have a very small angle with respect to the beam axis, the uncertainties on the $z$ positions are large. Different $z$ values result in different reconstructed tracks and thus to a different pointing resolutions. Figures C.3 and Figures C.4 show the unbiased residuals for the telescope planes for three different testbeam periods. The distributions for each plane are slightly different for the three periods. At half maximum the differences in width are about 2 μm.

The studies above help explain why the position resolutions are not the same for the same type of sensor when measured in different testbeam periods. The measurement of spatial resolution depends on the telescope tracking performance which were shown to vary due to a number of effects. Over time, the depletion voltages of the telescope planes can change due radiation damage (Section 2.3) experienced by the telescope. The radiation damage and temperature variations can cause an increase in noise that may require the the equalisation procedure to be reapplied (Section 4.1.3). And the estimates on the pointing resolution of the telescope rely on accurate estimates of the $z$ positions of the planes, that may not have been recorded between different testbeam campaigns.

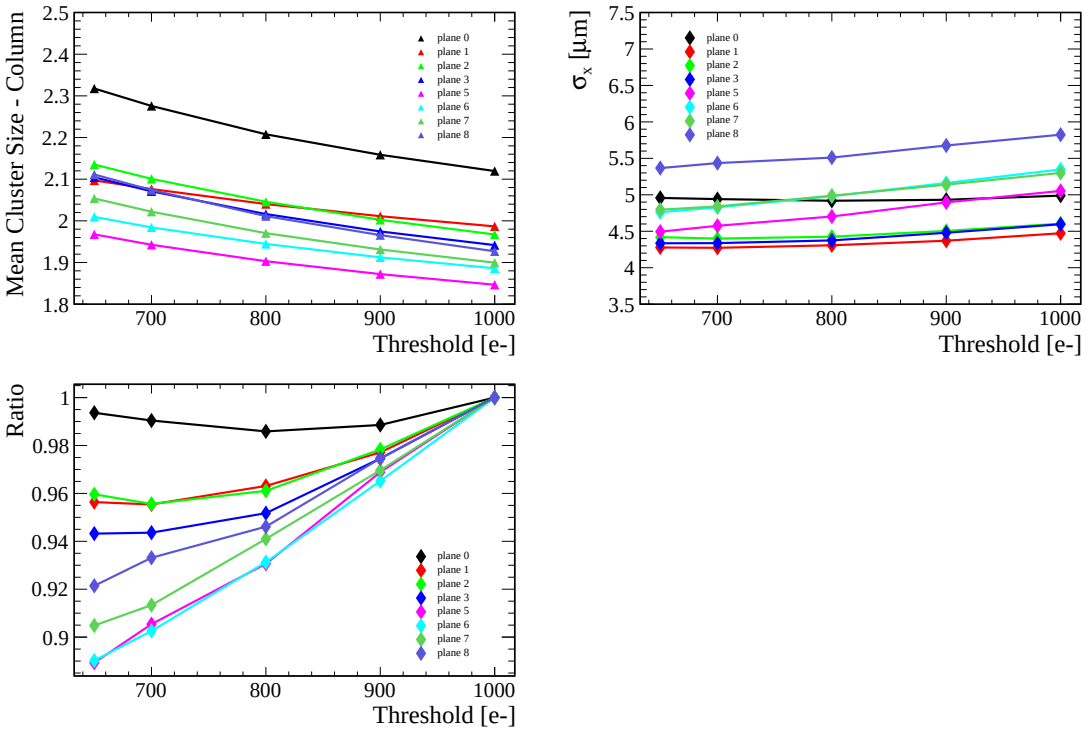


Figure C.2: The mean cluster size in columns as a function of the threshold for each of the telescope planes (a). The bias voltage of each of the telescope sensors was set to 150 V. The unbiased spatial resolution in $x$ for each of the telescope planes as a function of the threshold (b). The ratio ($\sigma_x[i]/\sigma_x[1000e^-]$) as a function of the threshold for all telescope planes (c).

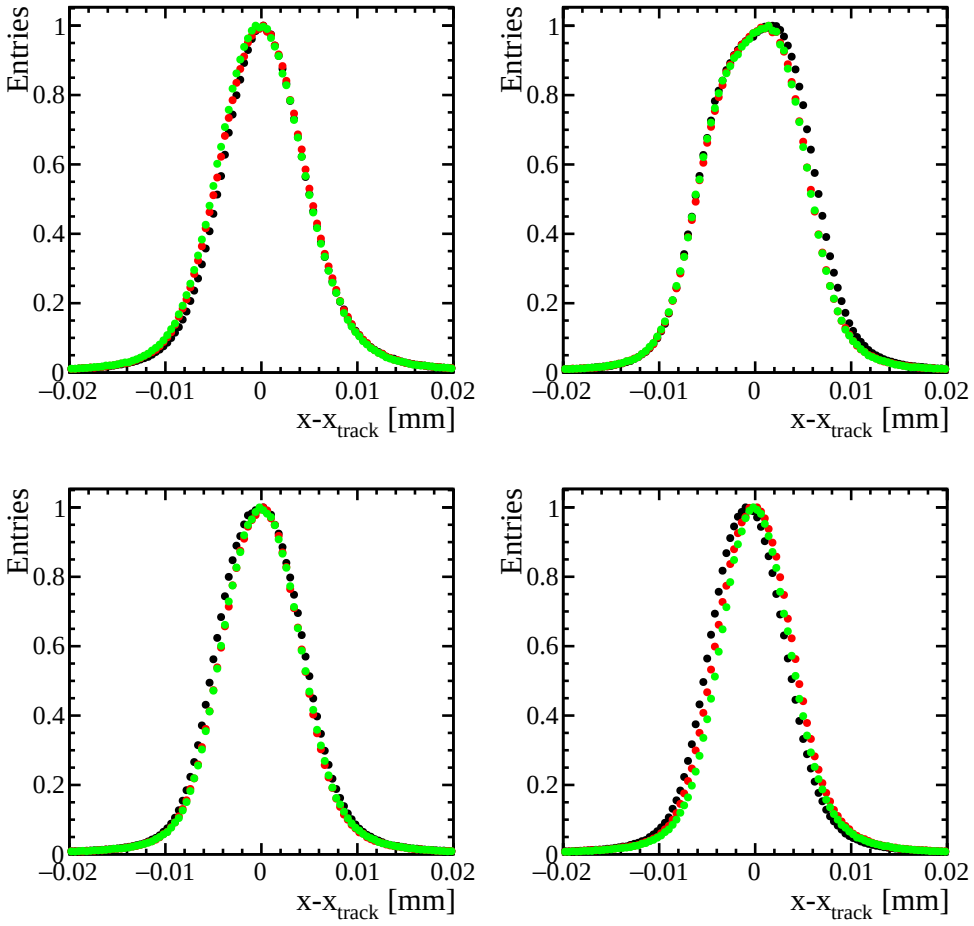


Figure C.3: Unbiased residuals for measured during two different testbeam months for the front arm of the telescope. (a) plane 0, (b) plane 1, (c) plane 2 and (d) plane 3. The coloured markers represented residuals measured during 3 different months of testbeam.

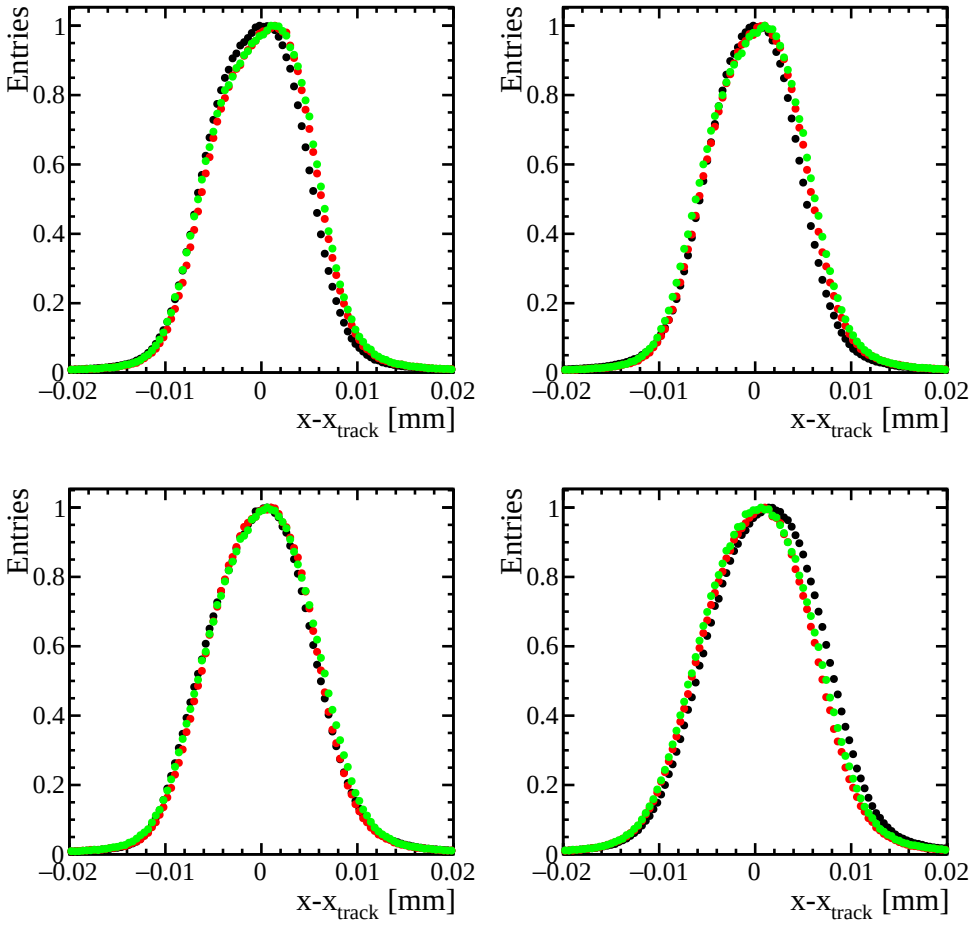


Figure C.4: Unbiased residuals for measured during two different testbeam months for the front arm of the telescope. (a) plane 5, (b) plane 6, (c) plane 7 and (d) plane 8. The coloured markers represented residuals measured during 3 different months of testbeam

# Bibliography


[1] **Particle Data Group** Collaboration, "Review of particle physics," *Phys. Rev. D* **98** (Aug, 2018) 030001. https://link.aps.org/doi/10.1103/PhysRevD.98.030001.

[2] **The LHCb** Collaboration, "The lhcb detector at the lhc," *Journal of Instrumentation* **3** (2008) no. 08, S08005. http://stacks.iop.org/1748-0221/3/i=08/a=S08005.

[3] **The LHCb** Collaboration, *LHCb VELO (VErtex LOcator): Technical Design Report*. CERN, Geneva, 2001.

[4] "Letter of Intent for the LHCb Upgrade," Tech. Rep. CERN-LHCC-2011-001. LHCC-I-018, CERN, Geneva, Mar, 2011. https://cds.cern.ch/record/1333091.

[5] **The LHCb** Collaboration, "LHCb VELO Upgrade Technical Design Report," Tech. Rep. CERN-LHCC-2013-021. LHCB-TDR-013, Nov, 2013. https://cds.cern.ch/record/1624070.

[6] E. Frojdh, M. Campbell, M. D. Gaspari, S. Kulis, X. Llopart, T. Poikela, and L. Tlustos, "Timepix3: first measurements and characterization of a hybrid-pixel detector working in event driven mode," *Journal of Instrumentation* **10** (2015) no. 01, C01039. http://stacks.iop.org/1748-0221/10/i=01/a=C01039.

[7] T. Poikela, M. D. Gaspari, J. Plosila, T. Westerlund, R. Ballabriga, J. Buytaert, M. Campbell, X. Llopart, K. Wyllie, V. Gromov, M. van Beuzekom, and V. Zivkovic, "Velopix: the pixel asic for the lhcb upgrade," *Journal of Instrumentation* **10** (2015) no. 01, C01057. http://stacks.iop.org/1748-0221/10/i=01/a=C01057.

[8] L. Evans and P. Bryant, "LHC machine," *JINST* **3** (2008) S08001.

[9] "The atlas experiment at the cern large hadron collider," *Journal of Instrumentation* **3** (2008) no. 08, S08003. http://stacks.iop.org/1748-0221/3/i=08/a=S08003.

[10] **CMS** Collaboration, S. Chatrchyan *et al.*, "The CMS experiment at the CERN LHC," *JINST* **3** (2008) S08004.

[11] "The alice experiment at the cern lhc," *Journal of Instrumentation* **3** (2008) no. 08, S08002. http://stacks.iop.org/1748-0221/3/i=08/a=S08002.

[12] M. Altarelli and F. Teubert, "B physics at LHCb," *Int. J. Mod. Phys.* **A23** (2008) 5117.

[13] T. L. Collaboration, "LHCb bb production angle plots,". lhcb.web.cern.ch/lhcb/speakersbureau/html/bb_ProductionAngles.htm.

[14] R. Aaij *et al.*, "Performance of the LHCb Vertex Locator," *JINST* **9** (2014) P09007, arXiv:1405.7808 [physics.ins-det].

[15] D. P. M. Hynds, L. Eklund, P. Soler, and C. Parkes, "Resolution studies and performance evaluation of the LHCb VELO upgrade," Mar, 2015. https://cds.cern.ch/record/2004399. Presented 27 Nov 2014.

[16] P. Bartalini, J. Buytaert, M. J. Charles, P. Collins, H. Dijkstra, O. Dormond, M. Elsing, M. Ferro-Luzzi, F. Fiedler, R. Frei, G. Gagliardi, P. Jalocha, T. Ketel, P. Koppenburg, J. Libby, C. Parkes, U. Parzefall, T. Ruf, D. Steele, M. Tareb, F. Teubert, M. Witek, and V. Wright, "VELO telescope resolution and efficiency measurements,". https://cds.cern.ch/record/691510. revised version number 1 submitted on 2000-10-27 16:06:45.

[17] **LHCb Collaboration** Collaboration, "Expression of Interest for a Phase-II LHCb Upgrade: Opportunities in flavour physics, and beyond, in the HL-LHC era," Tech. Rep. CERN-LHCC-2017-003, CERN, Geneva, Feb, 2017. https://cds.cern.ch/record/2244311.

[18] **LHCb Outer Tracker group** Collaboration, R. Arink *et al.*, "Performance of the LHCb Outer Tracker," *JINST* **9** (Nov, 2013) P01002. 30 p. https://cds.cern.ch/record/1629476.

[19] The LHCb RICH Collaboration, "Performance of the lhcb rich detector at the lhc," *The European Physical Journal C* **73** (May, 2013) 2431. https://doi.org/10.1140/epjc/s10052-013-2431-9.

[20] F. Machefert and A. Martens, "Overview of the lhcb calorimeters," *Nuclear Instruments and Methods in Physics Research Section A: Accelerators, Spectrometers, Detectors and Associated Equipment* **617** (2010) no. 1, 40 – 44. http://www.sciencedirect.com/science/article/pii/S016890020901907X. 11th Pisa Meeting on Advanced Detectors.

[21] B. Muratori and T. Pieloni, "Luminosity levelling techniques for the LHC,". https://cds.cern.ch/record/1957033. Comments: 5 pages, contribution to the

ICFA Mini-Workshop on Beam-Beam Effects in Hadron Colliders, CERN, Geneva, Switzerland, 18-22 Mar 2013.

[22] T. Head, "The lhcb trigger system," *Journal of Instrumentation* **9** (2014) no. 09, C09015. http://stacks.iop.org/1748-0221/9/i=09/a=C09015.

[23] N. Wermes, L. Rossi, P. Fischer, and T. Rohe, *Pixel Detectors, From Fundamentals to Applications*. Springer-Verlag, 2006.

[24] L. Eklund, "Physics benchmarks of the velo upgrade," *Journal of Instrumentation* **11** (2016) no. 12, C12066. http://stacks.iop.org/1748-0221/11/i=12/a=C12066.

[25] G. Lutz, *Semiconductor Radiation Detectors: Device Physics*. 01, 2007.

[26] W. R. Leo, *Techniques for Nuclear and Particle Physics Experiments: A How to Approach*. 1987.

[27] R. S. Gilmore, *Single particle detection and measurement*. 1992.

[28] S. E. Richards and J. Velthuis, "Characterisation of silicon detectors for the LHCb Vertex Locator Upgrade," Nov, 2017. https://cds.cern.ch/record/2626889. Presented 15 Dec 2017.

[29] F. Hartmann, "Evolution of Silicon Sensor Technology in Particle Physics," *Springer Tracts Mod. Phys.* **231** (2009) 1–204.

[30] H. Spieler., *Semiconductor Detector System*. 2005.

[31] M. Moll, *Radiation damage in silicon particle detectors: Microscopic defects and macroscopic properties*. PhD thesis, Hamburg U., 1999. http://www-library.desy.de/cgi-bin/showprep.pl?desy-thesis99-040.

[32] A. Affolder *et al.*, "Radiation damage in the LHCb Vertex Locator," *JINST* **8** (2013) P08002, arXiv:1302.5259 [physics.ins-det].

[33] C. Dean, "Time Dependent Studies of B→$h^+h'^-$ Decays and Research and Operation for the VELO Project at LHCb," *PhD Thesis, University of Glasgow* (2019) .

[34] T. Poikela, J. Plosila, T. Westerlund, M. Campbell, M. De Gaspari, X. Llopart, V. Gromov, R. Kluit, M. van Beuzekom, F. Zappon, V. Zivkovic, C. Brezina, K. Desch, Y. Fu, and A. Kruth, "Timepix3: a 65K channel hybrid pixel readout chip with simultaneous ToA/ToT and sparse readout," *Journal of Instrumentation* **9** (May, 2014) C05013.

[35] J. Visser, M. van Beuzekom, H. Boterenbrood, B. van der Heijden, J. Muoz, S. Kulis, B. Munneke, and F. Schreuder, "Spidr: a read-out system for medipix3

timepix3," *Journal of Instrumentation* **10** (2015) no. 12, C12028. http://stacks.iop.org/1748-0221/10/i=12/a=C12028.

[36] N. Alipour Tehrani, G. Dissertori, and D. Dannheim, "Test-beam measurements and simulation studies of thin pixel sensors for the CLIC vertex detector,". http://cds.cern.ch/record/2270788. Presented 13 Mar 2017.

[37] F. M. Pitters, N. Alipour Tehrani, D. Dannheim, A. Fiergolski, D. Hynds, W. Klempt, X. Llopart Cudie, M. Munker, A. M. Nurnberg, S. Spannagel, and M. J. Williams, "Time and Energy Calibration of Timepix3 Assemblies with Thin Silicon Sensors,". http://cds.cern.ch/record/2649493.

[38] M. Vicente Barreto Pinto, K. Carvalho Akiba, and E. Ribeiro Polycarpo Macedo, "Caracterizao do TimePix3 e de sensores resistentes  radiao para upgrade do VELO,". https://cds.cern.ch/record/2134709. Presented 04 Sep 2015.

[39] P. Tsopelas, "A silicon pixel detector for LHCb," 2016. https://cds.cern.ch/record/2238509. Presented 21 Nov 2016.

[40] J. Jakubek, "Precise energy calibration of pixel detector working in time-over-threshold mode," *Nucl. Instrum. Meth.* **A633** (2011) S262–S266.

[41] K. Akiba *et al.*, "The Timepix Telescope for High Performance Particle Tracking," *Nucl. Instrum. Meth.* **A723** (2013) 47, arXiv:1304.5175 [physics.ins-det].

[42] V. Blobel, "Software alignment for tracking detectors," *Nucl. Instrum. Meth.* **A566** (2006) 5–13.

[43] V. Franco, "Title to be determined," *PhD Thesis, University of Liverpool* (2019) .

[44] E. Dall'occo, "Title to be determined," *PhD Thesis, Nikhef* (2019) .

[45] J. A. Appel *et al.*, "Performance of prototype BTeV silicon pixel detectors in a high-energy pion beam," *Nucl. Instrum. Meth.* **A485** (2002) 411–425, arXiv:hep-ex/0108014 [hep-ex].